Presheath and Double Layer Structures in an Argon Helicon Plasma Source

by

M. Umair Siddiqui

A dissertation submitted in partial fulfillment of
the requirements for the degree of

Doctor of Philosophy
(Nuclear Engineering & Engineering Physics)

at the

UNIVERSITY OF WISCONSIN - MADISON
2014

Date of final oral examination: 8/8/2014

The dissertation is approved by the following members of the Final Oral Committee:

James Blanchard, Professor, Nuclear Engineering & Engineering Physics
Noah Hershkowitz, Professor, Nuclear Engineering & Engineering Physics
Carl Sovinec, Professor, Nuclear Engineering & Engineering Physics
Oliver Schmitz, Professor, Nuclear Engineering & Engineering Physics
Riccardo Bonazza, Professor, Nuclear Engineering & Engineering Physics
Benjamin Longmier, Professor, Aerospace Engineering, University of Michigan

Contents

List of Figures

0.1 Dedication

To my father:

"*A very few lonely pioneers make their way to high places never before visited ... they create the living conditions of mankind and the majority are living on their work*"

- Kristian Birkeland -

To my mother:

"*Hey mama,*

I wanna scream so loud for you,

Cause I'm so proud of you,

Let me tell you what I'm about to do,

I know I act a fool,

But I promise you I'm going back to school,

I appreciate what you allowed for me,

I just want you to be proud of me"

- Kanye West -

0.2 Acknowledgements

The experiments detailed here are the results of countless contributions from many people. I would like to thank my mentor and friend for the past four years, professor Noah Hershkowitz. Noah has provided an environment for me that I can only describe as a playground. After forty years doing experimental plasma physics, Noah has acquired a wealth of experimental apparatus and related equipment. Giving me independence and incredible resources has been a luxury a student experimentalist can only dream of. Furthermore, Noah strives to make himself personally available to his students despite whatever else he has going on. This level of access is crucial as Noah's many years in plasma physics has given him experiences in virtually every possible engineering and scientific situation one can find themselves in. Spending time with Noah has been just as important to the success of this project as his resources has been. For this Noah, and for your and Ros's friendship, I thank you.

I also thank the members of my thesis committee, professors Oliver Schmitz, Riccardo Bonazza, Carl Sovinec, and Ben Longmier. Each member provided essential advice, comments and questions that progressed this experimental endeavor. Without the help designing of the apparatus, information on engineering applications, or acute questions cutting to the basic physics of the problems, the project would not have been completed, or as fleshed out as the final product presented here.

In addition I would like to thank professors Earl Scime from West Virginia University and Greg Severn from the University of San Diego. Both Greg and Earl were indispensable resources throughout this project. Greg single handedly taught me all I know about the laser-induced fluorescence diagnostic that is vital to this experiment. Likewise, Earl taught me much of what I know about helicons, their experimental construction, and appropriate diagnosis. It was obvious very early on that without their help I would not be able to complete this project.

I have had the good fortune of having the ongoing mentorship of two more teachers, Kristina Lynch, my undergraduate advisor, and Greg Devine, my high school physics and math teacher. Both Kristina and Greg have the incredible skill of being able to identify the intellectual state of mind of a student, and the ability to guide the student to the next stage along their path of learning. Their lessons continue to resonate with me, and their simple explanations of complex topics continue to help me to break down complicated research problems. It is by example that they have shown me how to introduce others to the complexities of science and research for the first time. I hope that I can inspire my own share of people, just as they have inspired me.

My own students while at UW, Paul Crandall, Justin Kim and Cory Jackson, have been a joy to work with. You all have consistently exceeded my high expectations of you, and you have endured my continuous pushing. There is simply no way this project could have been completed on schedule without the assistance of my undergraduates in the design, construction, and use of the experimental apparatus. Furthermore, I have learned a great deal from you all, especially how to approach students and introduce them to basic design and experimental techniques.

My friends have been a resource I could not go on without. Derek and Marisa, Corey, Jaime and Niall, Matt, Adam, Dinh, Sirous and Urza in Madison, and June and Flor back home, you have been my family while in Madison, have supported me, put up with me, and introduced me to new things. Derek and Matt have also directly contributed to the design, and analysis of my experiment. One of my father's students once said "science is nothing without love and friendship", and my experiences with you all in graduate school exemplify this sentiment.

Finally my family has been the most incredible and supportive resource I could ask for. Whether it has been physically helping me get moved into Madison, calming me over the phone, or with specific advice on how to deal with adversities while in school, my

family's presence in my life is what made this project possible. In the dedication I have separate quotes for my father and mother. In reality what is expressed in those statements can be extended to either of them. Both my parents in my view have pushed their own comfort zones both to raise me by their own ideals, and to further pursue knowledge. As my friends know by the way I talk about them, I am very proud of the accomplishments of my mother and father. Without my pride in them and the confidence they have imbued in me I would not be able to continue my own pursuits of knowledge on my own. For this and many other reasons I could not possibly fit into this thesis, I thank you.

0.3 Abstract

Ion velocities and temperatures, plasma density, potential, and electron temperatures are measured in a 13.56 MHz helicon produced argon plasma upstream from a grounded plate inside a 10 cm ID cylindrical Pyrex vacuum chamber. The plate is held at $\psi = 0^o \rightarrow 60^o$ relative to the background axial magnetic field in the system. For the $\psi = 0^o$ experiment, two distinct helicon discharge equilibria are observed at 500 W rf power, 900 G magnetic field, and a neutral pressure of $3 \rightarrow 4$ mTorr. Both modes exhibit a localized region of hot electrons ($T_h \approx 10$ eV, $T_c \approx 3.5$ eV). For the first mode the hot electrons are confined by a localized potential structure and the density decreases monotonically towards the grounded plate. For the second mode the hot electrons cool off gradually in space due to heat conduction generating a downstream density peak and no major potential structures are observed. It is found that the type of discharge mode is determined by the location of the grounded plate, the length of the presheath, and the rf electron heating mechanism.

For the $\psi = 16^o \rightarrow 60^o$ plate positions, ion flow to the boundary where a 1 kG magnetic field is obliquely incident is measured at 1, 3, and 6.5 mTorr neutral pressure and $450 \rightarrow 750$ W rf power. The results are compared to the magnetic presheath models put forth by Chodura [Phys. Fluids **25**, 1628 (1982)], Riemann [Phys. Plasmas **1**, 552 (1994)], and Ahedo [Phys. Plasmas **4**, 4419 (1997)]. Ion flows in the $x - z$ plane follow the magnetic field lines within the limit $v_\perp / v_{||} \leq 25\%$. The 1 mTorr dataset is used to benchmark a one-dimensional fluid model for the ion flow in the presheath. Definitions of the "magnetic presheath" are discussed. The fluid model in conjuction with the data show that the ion velocities in the $\vec{E} \times \vec{B}$ direction can be $10\% \rightarrow 40\%$ of c_s for the angles investigated. Ion flow to fusion experiment boundaries and Hall thruster walls is discussed.

Chapter 1

Introduction

In most scientific and industrial applications plasmas come in contact with bounding surfaces such as the wall of a fusion experiment or an electric propulsion device. In many cases potential structures form to balance the net fluxes of charges leaving the plasma to the boundary. These regions are called sheaths and presheaths [1]. While sheaths and presheaths around surfaces in relatively cold plasmas have been studied for some time [2, 3, 4, 5, 6, 7, 8, 9], the role of the presheath and its interactions with hotter, magnetized and collisional plasmas is not well understood. Understanding these boundaries is critical to solving major problems such as erosion of divertor surfaces [10] and Hall thruster channel walls [11], which limit the lifetimes of the respective apparatus. To a lesser extent this boundary is important for understanding probe characteristics in magnetized plasmas [12]. In fusion experiments, regions near the walls contain strong, obliquely incident magnetic fields, and significant ion-neutral collisions and ionization. In these regions measured heat loads to the walls from plasma flows disagree with computer models and emission spectroscopy diagnostics [13, 14]. Understanding these regions is also critical for setting the proper boundary conditions for fusion turbulence [15] and MHD [16] codes. For Hall thrusters magnetic fields are obliquely incident on the thruster wall. Modern simulations do not accurately predict the level of the experimentally observed channel erosion

[17, 18, 19]. For probe measurements in space [20] and strongly magnetized fusion plasmas [21], the particle fluxes to the probes depend on the details of the potential structures at the probe's magnetized plasma boundary.

In order to investigate presheaths in collisional, magnetized plasmas with electron temperatures (T_e) hot enough for significant ionization ($\nu_{iz} \sim \nu_c$, where $\nu_{iz,c}$ is the ionization/ion-neutral collision frequency respectively), ion velocity distribution functions (IVDFs), plasma densities and potentials, and electron temperatures are measured in a helicon plasma upstream from a grounded plate. Helicons are radio frequency (rf) plasma sources generated by resonant interaction of an electromagnetic wave with a preexisting plasma [22]. They often produce plasmas with similar parameters to those at the edges of fusion experiments ($n_{e,n} \approx 10^{12} \rightarrow 10^{13} cm^{-3}$, $T_e \approx 5 \rightarrow 10$ eV, where $n_{e,n}$ is the electron/neutral density) and require a background magnetic field to operate [23]. The angle of the plate normal relative to this field (ψ) is varied from $0^o \rightarrow 60^o$.

For the $\psi = 0^o$ experiment the presheath structure is found to play a critical role in determining the overall helicon discharge equilibria, and in certain situations the location of a localized double layer structure in the plasma. Both discharge modes exhibit localized hot electrons ($T_e \approx 10$ eV). The discharge equilibria is determined by the location of the hot electrons, driven by the electron heating mechanism, the location of the downstream grounded boundary, and the length of the presheath of the boundary, which is determined by the ion-neutral collision length (λ) and the ionization frequency. For the discharge mode that exhibits the double layer, the double layer exists to confine the hot electrons. In the mode with no double layer the electrons cool via heat conduction in space.

The $\psi = 16^o \rightarrow 60^o$ experiments show that presheath structures in the presence of obliquely incident magnetic fields are highly sensitive to experimental and plasma parameters such as collision and ionization frequencies, magnetic field strength and angle of incidence. Simple theories in these cases are not good predictors for the length and struc-

ture of the presheath [24]. Finally the ion velocity in the $\vec{E} \times \vec{B}$ direction is found to be significant even when the magnetic field angle of incidence is close to normal, which must be properly accounted for when assessing ion induced erosion and sputtering, flow driven instabilities, and boundary conditions for computer models.

In the next chapter all relevant background information will be presented. Chapter 3 describes the experimental setups and information on the diagnostics. Chapter 4 shows and discusses the results of the $\psi = 0^o$ experiment, and chapter 5 gives the results of the $\psi = 16^o \rightarrow 60^o$ experiments. Conclusions are presented in chapter 6.

Chapter 2

Background information

2.1 Sheaths

To understand the plasma boundary it is instructive to look at the electric field due to an infinite charged planar surface in vacuum and plasma. The electric field and electric potential in all space due to such an object is given by Poisson's equation (displayed in one dimension for planar geometry and SI units)

$$\frac{d^2\phi}{dx^2} = -\frac{en(x)}{\epsilon_o} \tag{2.1}$$

where ϕ is the electric potential, e is the fundamental charge in Coulombs, $n(x)$ is the density of charges, and ϵ_o is the permittivity of free space. In vacuum $n(x) = 0$ and thus the electric field $E = -d\phi/dx$ is constant everywhere, and ϕ changes linearly away from the surface.

In a plasma the right hand side of equation 2.1 is no longer zero because the plasma by definition contains charged particles. These particles will move to shield the electric field from the charged plane. These particles will have a distribution of energies, often described by the Maxwell-Boltzmann relation given in equation 2.2

$$f_{e,i} = \sqrt{\frac{m_{e,i}}{2\pi T_{e,i}}} exp\left(-\frac{m_{e,i}v_{e,i}^2}{2T_{e,i}}\right) \tag{2.2}$$

where $f_{e,i}$ is the electron/ion distribution function, $m_{e,i}$ is the electron/ion mass, $T_{e,i}$ is the electron/ion temperature in units of energy, and $v_{e,i}$ is the electron/ion velocity in a single dimension. Because of the their distribution of energies, some particles will escape the electric potential well generated by the charged wall. The plasma will not completely shield out the wall's electric field, which will still be non-zero close to the wall. This region is non-neutral, contrary to a typical undisturbed plasma. This non-neutral region is called the plasma sheath, a term first coined by Irving Langmuir [25].

The potential and density structure in the sheath can take different analytical forms for different plasma parameters (the matrix sheath, the collisional sheath etc). One common formulation, the Child-Langmuir sheath, is derived here. The entrance to the sheath in this example is defined to be at $x = 0$ and the plasma potential at this point is defined to be $\phi(x = 0) = 0$. In this situation, the sheath thickness is much less than the ion mean free path such that the sheath is considered to be collisionless. The difference between the wall potential and the plasma potential is much greater than the electron temperature in units of energy ($e\phi/T_e \gg 1$). As a result the potential in the sheath is negative enough that the electron density in the sheath is considered to be negligible $(n_e(x) \approx 0)$ compared to the ion density $(n_i(x))$. The ions are considered to be perfectly cold ($T_i = 0$). Furthermore the electric field at 0 is also considered to be small $(E(x = 0) \approx 0)$.

Because the ions do not suffer any collisions in the sheath, the ion flux is conserved throughout. Thus the ion current density throughout the sheath is constant $(J(x) = J(x = 0) = J_0)$ and the ion density in the sheath is given by

$$n_i(x) = \frac{J_o}{ev_i(x)} = \frac{J_0}{e\left(\frac{-2e\phi(x)}{M_i}\right)^{1/2}} \tag{2.3}$$

Inserting this into Poisson's equation (equation 2.1), integrating twice and solving for the plasma potential one obtains

$$\phi(x) = \left(\frac{9J_0x^2}{4\epsilon_0}\sqrt{M_i/2e}\right)^{2/3} \tag{2.4}$$

which is the well known form of space-charge-limited current collection [26]. The sheath region is often scaled to the Debye length $\lambda_D = \sqrt{\epsilon_0 T_e / n_0 e^2}$. This model fits experimental data well for many low temperature, collisionless, single ion species plasma sheaths with perfectly absorbing walls [5].

2.2 Presheaths

2.2.1 The necessity of the presheath

In order to solve for the potential structure outside of the electron-free sheath, the electron density must be taken into account. The full classical equilibrium electron energy distribution function yields the Boltzmann relation for the electron density

$$n_e(x) = n_0 exp[e\phi(x)/T_e] \tag{2.5}$$

where n_0 is the bulk plasma density. Inserting this and 2.3 into Poisson's equation one obtains

$$\frac{d^2\phi}{dx^2} = -\frac{1}{\epsilon_0}\left(\frac{J_0}{e\left(\frac{-2e\phi(x)}{M_i}\right)^{1/2}} - n_0 exp\left(\frac{e\phi(x)}{T_e}\right)\right) \tag{2.6}$$

which is not solvable analytically. However, after multiplying by $d\phi/dx$, integrating once, and looking near the limits $d\phi/dx \approx 0$ and $\phi \ll 1$ one obtains the condition

$$v_i(x=0) > \sqrt{T_e/M_i} \equiv u_B \tag{2.7}$$

which is called the Bohm sheath criterion (positive velocity is towards the boundary). This was first recognized by Langmuir [27] and calculated by Bohm [28]. Explicitly, the condition maintains that the ions must enter the non-neutral sheath region with a speed directed towards the wall that is greater than or equal to the ion sound speed (c_s) when the ion temperature is negligible with respect to the electron temperature.

This result implies that there must be some electric field outside of the electron-free sheath that accelerates ions to this speed. This electric field must be relatively small (compared to the other terms in equation 2.6 after it is integrated once) in order to satisfy the assumptions from the previous derivation. Furthermore this electric field must exist in a region where the electron density is non-negligible and is given by equation 5.3. This region of accelerating electric field and significant electron density is called the presheath.

The necessity of the presheath can be understood if one looks at how the electron and ion densities change in the sheath. Electron density will follow the Boltzmann relation (equation 5.3), whereas the ion density is given by flux conservation (equation 2.3). If ions start off at a speed directed towards the wall less than the sound speed, then at some point in the sheath the electron density will be greater than the ion density. This effect is shown in figure 2.1 where $y_0 = M_i v_i^2 / 2T_e$. Thus the sheath potential profile will not

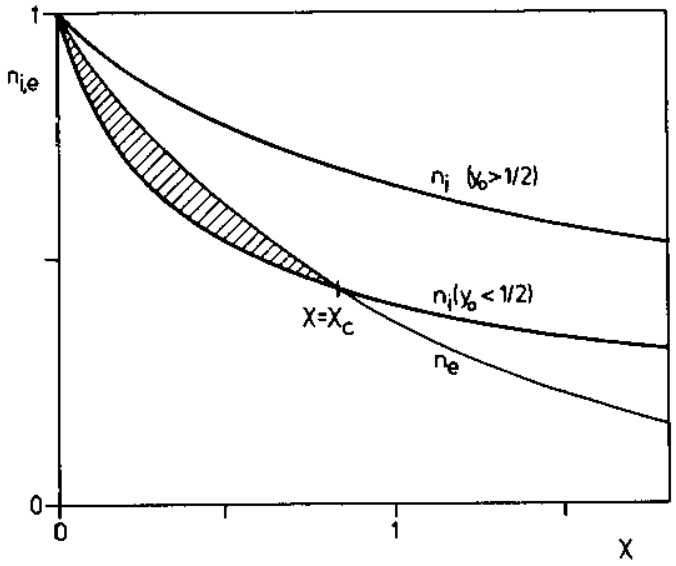

Figure 2.1: Electron and ion densities in the sheath with different starting ion velocities [29].

decrease monotonically (as can be seen from equation 2.1). This contradicts the condition that electron density is much less than the ion density in the sheath. For a physical and

mathematically sound solution the ions must enter the electron-free region with a velocity of at least the sound speed [1].

2.2.2 Presheaths in weakly collisional plasmas

The presheath has been extensively reviewed by Riemann [3, 29] for the cases where $\lambda/\lambda_D \gg 1$ in the absence of a magnetic field. Riemann solves Poisson's equation numerically for both the sheath and presheath regions. When solving for the sheath region Riemann derives and numerically solves equation 2.4. Solving for the presheath region, Riemann solves Poisson's equation, using the Boltzmann relation for the electron density. For the ion density Riemann uses

$$n_i(x) = \frac{J_0}{e v_i(x)} \tag{2.8}$$

In the presheath solution Riemann requires that the ion mean free path be less than or on the order of the length of the presheath. Thus $v_i(x)$ is not solved for by energy conservation as the ions undergo collisions in the presheath and do not conserve energy. Instead he solves for the ion velocity by solving the ion momentum equation

$$M_i v_i(x) \frac{dv_i}{dx} = -e\frac{d\phi}{dx} - \nu_c M_i v_i(x) \tag{2.9}$$

where ν_c is a frictional collision frequency that does not include ionizing collisions [3]. Riemann shows that the resulting numerical solution for the presheath approaches a singularity as the ion velocity approaches $\sqrt{T_e/M_i}$, or the ion sound speed for $T_i \ll T_e$. Close to this singularity he shows that in this region the plasma potential changes as

$$\phi(x) = -\frac{T_e}{e}\sqrt{\frac{x_0 - x}{\lambda}} \tag{2.10}$$

where x_0 is the location of the sheath-presheath transition. Riemann defines the "inside edge" of the presheath to be where his solution reaches this singularity.

Physically the plasma potential does not reach a singularity in any plasma experiment. Riemann resolves this by deriving a "matching" solution between his presheath and sheath solutions. To accomplish this he normalizes his governing equations (equations 2.1 and 2.9) to an arbitrary scaling factor and looked near the limit where $\lambda_D/\lambda \rightarrow 0$, where λ is the ion collision length. He shows that this "intermediate" solution matches his solutions to the presheath and the sheath to continuously solve for the plasma potential and density in space around a boundary in a weakly collisional plasma [3]. Riemann also claims that the length of this transition region scales as $\lambda^{1/5}\lambda_D^{4/5}$.

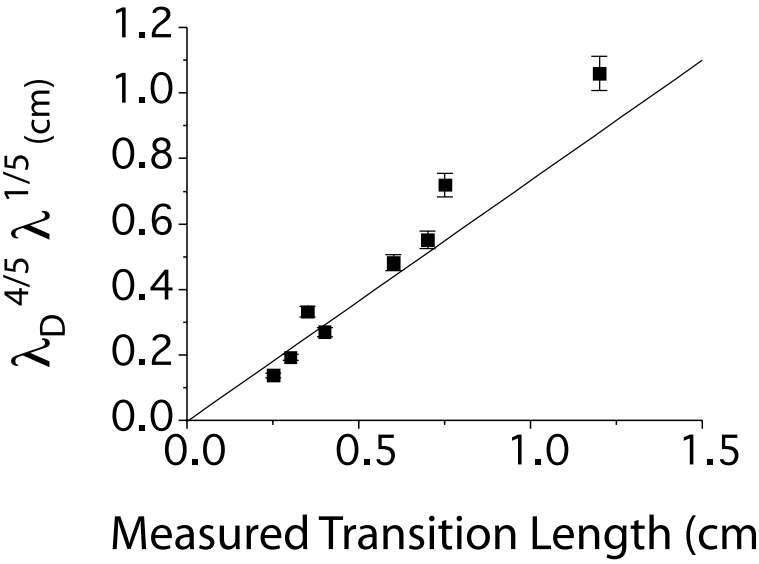

Figure 2.2: Presheath transition region length versus $\lambda^{1/5}\lambda_D^{4/5}$ [4].

These numerical results were confirmed experimentally by Oksuz and Hershkowitz [4] and are shown in figure 2.2. In this work, an emissive probe was used to measure plasma potential normal to a biased plate in a quiet, low temperature plasma generated in a multidipole chamber. Neutral pressure and primary electron energy were varied to change λ and λ_D. The presheath region was fitted to the numerical solution given by equation 2.10 and the sheath region was fitted to the solution given by equation 2.4. The

region between the inner and outer boundaries of the the aforementioned solutions was defined to be the intermediate regime, and the length of this region was shown to scale with $\lambda^{1/5}\lambda_D^{4/5}$ [3, 4].

In a collisionless presheath (λ is greater than the size of the system) to be accelerated to the sound speed, the potential drop across the presheath must be at least $T_e/2e$, from conservation of energy and from the requirement that the ions enter the sheath at the Bohm speed. In a system where λ is less than the experimental size scale, the ions will undergo several collisions in the presheath. Riemann [29, 30] claims that in this "collisional" regime the plasma potential drop can be determined transcendentally from

$$\frac{1}{2} - \frac{1}{2}exp\left(\frac{2e\phi(x)}{T_e}\right) - \frac{e\phi(x)}{T_e} = \frac{x}{\lambda} \tag{2.11}$$

Koch and Hitchon [31] observe this effect numerically. They show that as λ becomes shorter than half the size of the experimental apparatus that the potential drop needed to accelerate ions to the sound speed increases by at least a factor of 2.

Hershkowitz et al. [33] show mathematically that in weakly collisional presheaths ion flow velocity can be described by a "mobility-limited" model. This model assumes that in the presheath ions are described by the continuity equation 2.3 and the fluid equation 2.9. The authors assume that in the presheath $n_e \approx n_i$ and thus the ion density is also given by the Boltzmann relation (equation 5.3). Using these equations Hershkowitz et al. [33] show that the ion velocity can be given by the quadratic equation 2.12

$$v_i = \frac{eE}{M_i\nu}\left(1 - \frac{v_i^2}{c_s^2}\right) \tag{2.12}$$

where E is the electric field in the presheath and $c_s = \sqrt{(T_e + T_i)/M_i}$ is the ion sound speed.

Oksuz et al. [32] demonstrate experimentally using laser-induced fluorescence (LIF) and emissive probes in the presheath of a biased electrode in a quiet Argon plasma, that when λ is small compared to the size of the apparatus and when the plasma potential drop

across the presheath is $T_e/2e$ or more, the ions still are not accelerated to the sound speed due to collisional friction with neutrals. These data are shown in figures 2.3 and 2.4, where v_d is the ion drift velocity and c_s is the ion sound speed.

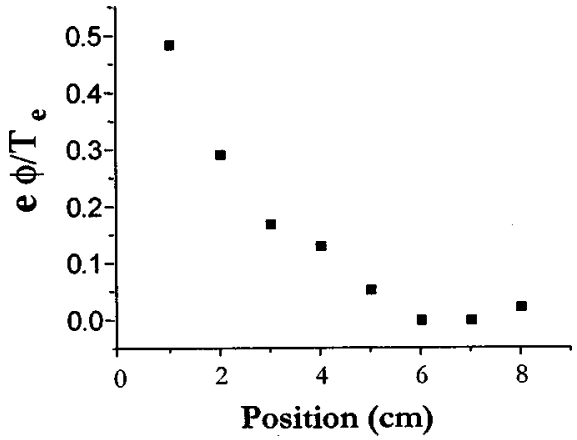

Figure 2.3: Plasma potential in the presheath versus distance from Oksuz et al. [32].

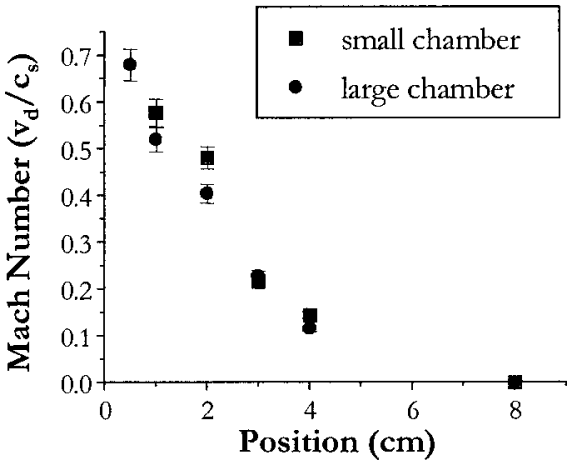

Figure 2.4: Ion drift velocity in the presheath versus distance in two different vacuum chambers from Oksuz et al. [32].

2.2.3 Presheaths in magnetized plasmas

The presheaths discussed until now have had scale lengths determined by experimental dimensions and ion collision lengths. In magnetized systems, the ion gyro radius (ρ_i) adds another scale length that can determine the presheath length. "Magnetized" plasmas refer to those where ρ_i and ρ_e (the electron gyro radius) are less than the relevant scale sizes of the system, such as the radius of the experimental vacuum chamber. The reigning paradigm for understanding the magnetized plasma boundary was proposed by Chodura [24] in 1982. Chodura modeled the plasma boundary using a particle-in-cell (PIC) method where a magnetic field was obliquely incident to an absorbing surface. He modeled an unmagnetized sheath boundary and criterion and thus set the ion velocity normal to the wall to equal the sound speed at the sheath-presheath interface. Chodura found that neglecting collisions and ionization, the ions had to enter the simulation space with a velocity equal to the sound speed along the magnetic field lines. Thus he postulated that the presheath consists of two structures, both quasineutral: one to accelerate the ions to the sound speed along the magnetic field, the collisional presheath, and one to accelerate them to the sound speed normal to the wall. He deemed this latter structure the "magnetic presheath" [24]. He also showed that the extent of the magnetic presheath in his simulations was equal to $\sqrt{6}(c_s/\omega_{ci})sin\psi$, where ω_{ci} is the ion cyclotron frequency and ψ is the angle between the magnetic field and the normal to the boundary.

Riemann [34] extended this work to include the effects of ion-neutral charge exchange collisions using a fluid model. From the numerical integration of his fluid equations he found that in the presence of collisions, the ion sonic point along the magnetic field approached the sheath edge - that is the magnetic presheath, as defined by Chodura [24] became shorter. Figure 2.5 shows Riemann's calculated ion drift velocity along the magnetic field (the 'x' direction is very nearly the direction of the magnetic field in this model). For $\nu \rightarrow 0$ the point where $v_x = c_s$ goes to $-\infty$; that is the parallel velocity must equal

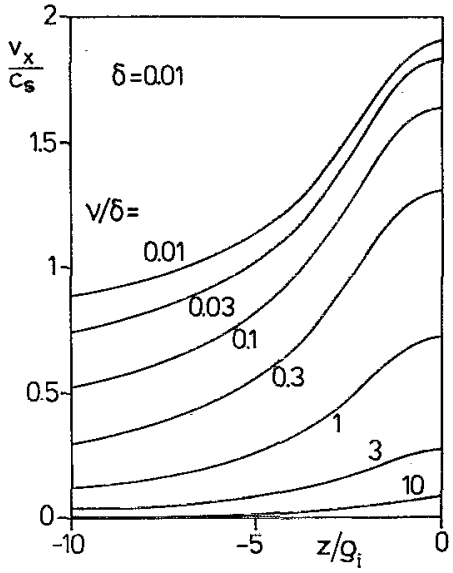

Figure 2.5: Calculated ion drift velocity along the magnetic field line versus distance from the boundary (normalized to ρ_i) [34]. $\delta = \tan(90^o - \psi)$.

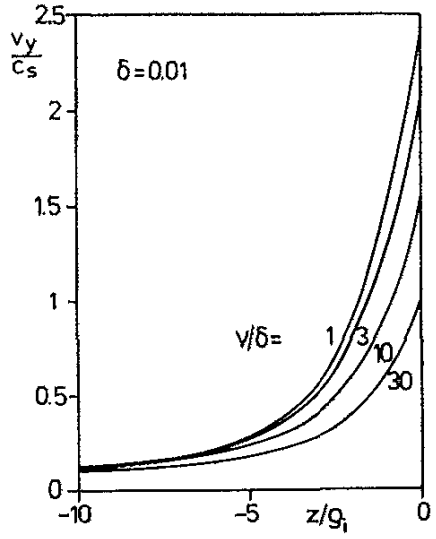

Figure 2.6: Calculated ion drift velocity in the $\vec{E} \times \vec{B}$ direction versus distance from the boundary (normalized to ρ_i) [34]. $\delta = \tan(90^o - \psi)$.

the sound speed at the entrance of his model - Chodura's result. As the collision frequency becomes comparable to the ion cyclotron frequency (ω_{ci}), this point comes closer to the point $z = 0$, the location of the sheath edge in his model.

Riemann also showed that the ion drift velocity in the $\vec{E} \times \vec{B}$ direction can become comparable to the sound speed near the sheath edge. Figure 2.6 shows v_y profiles from his calculation for different collision frequencies (the 'y' direction is the $\vec{E} \times \vec{B}$ direction in his model). For increasing collisionality the $\vec{E} \times \vec{B}$ directed ion flow slows.

This model was further extended by Ahedo [35] to arbitrary magnetic field angle of incidence and strength. His model showed that the presheath double structure (collisional and magnetic structures) only exists in the limit that $\lambda/\rho_i \rightarrow \infty$, where ρ_i is the ion cyclotron radius. Ahedo found that when $\lambda/\rho_i \rightarrow \mathcal{O}(1)$ the collisional presheath and the magnetic presheath become a solitary structure (with $\rho_i \gg \lambda_D$ in both cases). Specifically he showed that ion velocities perpendicular to the magnetic field lines could occur earlier in space than the location where the ions achieved the sound speed parallel to the magnetic field lines. Finally Stangeby [36] emphasized that including the plasma flow parallel to the boundary (the $\vec{E} \times \vec{B}$ direction) is important for being able to properly model the magnetic presheath using the fluid equations.

Other authors [39, 41] investigate magnetic presheaths in the limit where the magnetic field is parallel to the boundary. Schmitz et al. [39] solved for the plasma potential and density normal to a biased plate with parallel magnetic fields numerically using the same equations as Riemann [34]. They found, similarly to Riemann, that collisions play an integral role in transporting ions across the magnetic field lines to the boundary.

Despite their importance, there have been few experimental investigations of magnetic presheaths. Kim et al. [37] performed emissive probe measurements normal to a biased conducting plate in the presence of a plasma, where a magnetic field was obliquely incident. The experiments were performed in the parameter range of $\lambda/\rho_i = 10 \rightarrow 100$, with

$\rho_i \gg \lambda_D$. The log of the plasma potential profile in space exhibited regions of distinctly different slopes, the boundaries of which were taken to be the boundaries of different presheath regimes. In both the collisional and collisionless cases, the region that was assumed to be the magnetic presheath was found to scale as $(c_s/\omega_{ci})sin(\psi)$. These data are presented in figure 2.7.

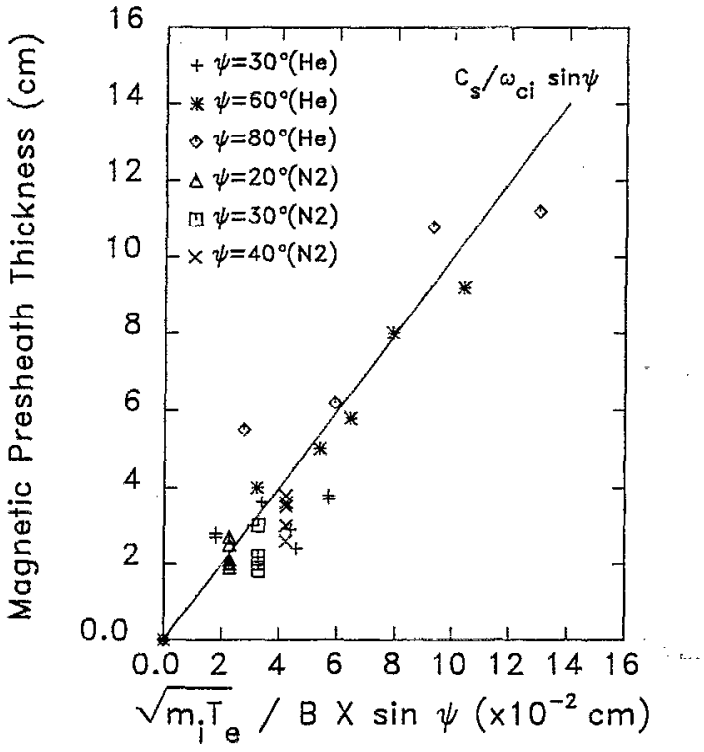

Figure 2.7: Scaling of the magnetic presheath from Kim et al. [37].

Measurements of magnetic presheaths have also been taken by Singha et al. [38]. In their work the authors performed measurements in a device similar to Kim et al. using the same diagnostics (Langmuir and emissive probes). They found that Chodura's form of the magnetic presheath length matched their data for angles of incidence between 30 and 90 degrees. In addition to measuring magnetic presheath lengths versus angle of incidence of the magnetic field, they were able to measure sheath thicknesses as well. They found

that as the magnetic presheath length increases, the sheath thickness decreases. They claim that this is because a longer magnetic presheath implies smaller presheath electric fields. In order to achieve space charge-limited current to the plate in the sheath, the sheath electric field must increase. To increase the electric field at fixed plate bias voltages, the extent of the sheath decreases [38]. Their data are presented in figure 2.8. In this figure

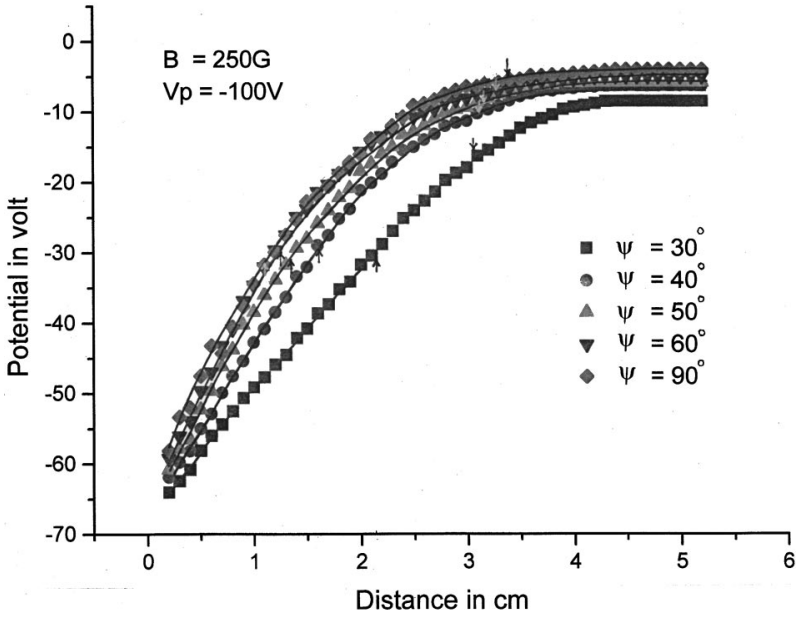

Figure 2.8: Plasma potential measurements in front of a biased plate in a plasma with obliquely incident magnetic fields [38].

the upward arrows indicate the sheath-presheath edge, and the downward arrows indicate the magnetic presheath edge.

A significant shortcoming of these experimental works was the inability to measure the ion drift velocities. Presheath lengths were estimated by looking at changes in the shape of the potential structures in space, while the magnetic presheath length is defined by Chodura [24] by the ion velocity boundary conditions. As such it is not clear whether the potential structures observed by Kim et al. [37] and Singha et al. [38] actually corresponded to the magnetic presheath, as defined by Chodura.

2.3 Double layers

Double layers are sheath-like structures, regions where the electric potential changes by amounts usually greater than $T_e[eV]/e$ over the scale of 1 - 100 Debye lengths (λ_D), away from any boundaries [5, 42, 43, 44]. Double layer phenomena occur in many plasma en-

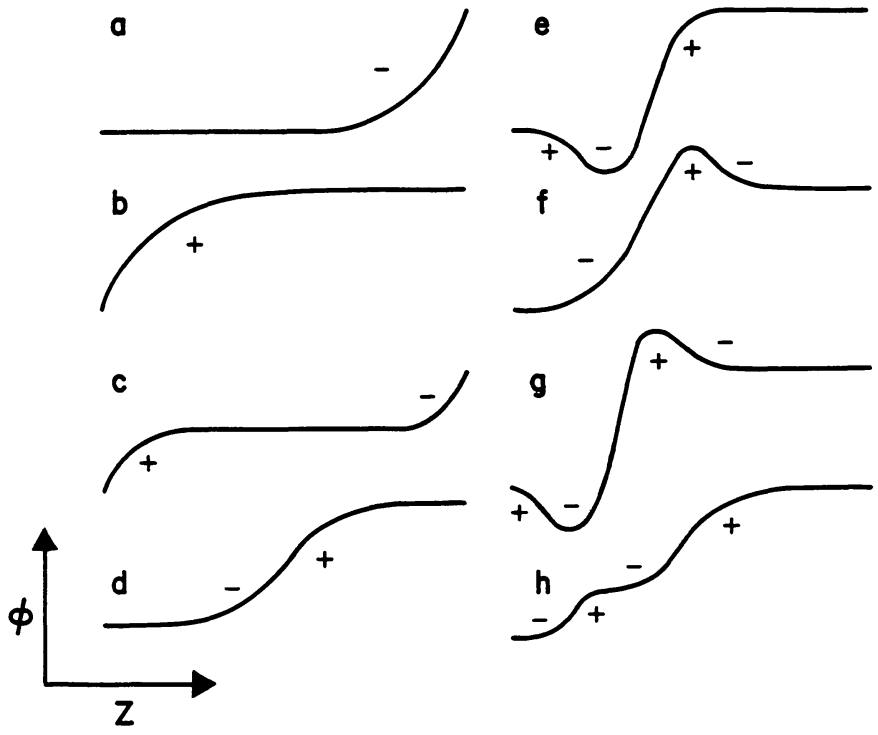

Figure 2.9: Schematics of many different manifestations of double layer structures [42]. ϕ is the plasma potential and z is the spatial coordinate. + and - represent areas of non-neutrality and the dominant charge in that region.

vironments including ionospheric plasmas and electric propulsion devices. Double layers manifest themselves through many different driving mechanisms. One recent structure of interest has been "current free" double layers in regions of expanding magnetic fields. The curvature of he field lines in the expansion region is small compared to the electron gyro radius and large compared to the ion gyro radius. As such the electrons remain stuck to

the expanding magnetic field lines and as such the electron density drops. From the Boltzmann relation (equation 5.3) the potential decreases in step. If the fields expand rapidly a potential jump can exist in a short space, generating a double layer [45]. These are under investigation for electric propulsion prototype devices [46, 47].

Double layers can also exist in regions of strong gradients of plasma density and temperature [42]. Steady state double layers have been observed joining regions of two electron temperatures [48, 49]. In some cases the double layer exists in order to balance particle fluxes from regions of plasma with two different electron temperatures [43, 50, 51]. As one region of electrons has greater thermal velocities, hot electrons stream out of the hot region faster than cold electrons can replenish them. In this case a double layer can exist to retard some of the fluxes of hot electrons and equalize the fluxes of replenishing cold electrons, similar to the action of a sheath near a floating boundary.

2.4 Helicon discharges

The helicon discharge is a resonant wave plasma generated and maintained by efficient coupling of a "bounded" whistler wave to a preexisting plasma. In a typical helicon source a cylindrical chamber is used with a helicon antenna wrapped around the outside. There are several helicon antenna geometries that are commonly used and are shown in figure 2.10. In this figure, the top left panel shows a symmetric (m = 0) loop antenna, the upper right is called a Nagoya type III (m = 1) antenna, and the bottom row shows a twisted Nagoya configuration, each with opposite polarity (m = $\pm$ 1). These antennas launch electromagnetic waves into the plasma. The wave fields depend on the antenna configuration and were calculated by Chen [53] and are given in figures 2.11 and 2.12. Helicons were first observed by Boswell in 1984 [22] where he reported on very efficient coupling of a whistler wave to a plasma with close to 100% ionization. In this work Boswell measured the characteristic linear relationship between the plasma density and the axial magnetic

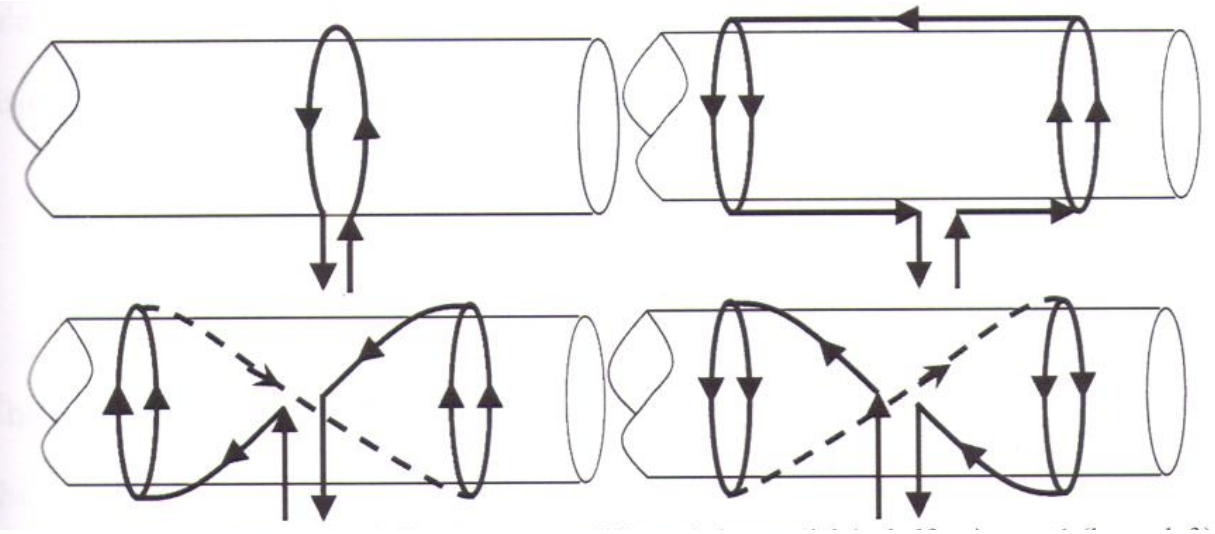

Figure 2.10: Common helicon antenna designs taken from Longmier [52].

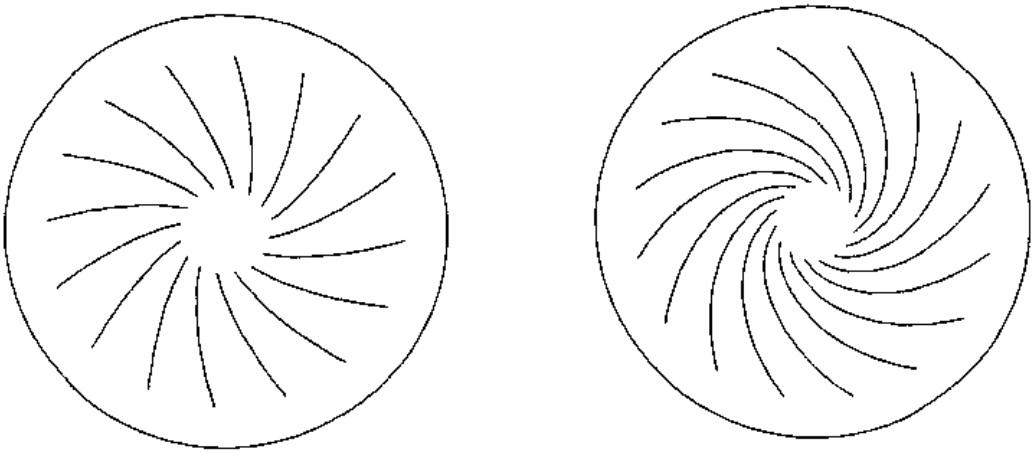

Figure 2.11: The m = 0 electric fields at different points downstream from the helicon antenna [53].

field strength. These data are shown in figure 2.13.

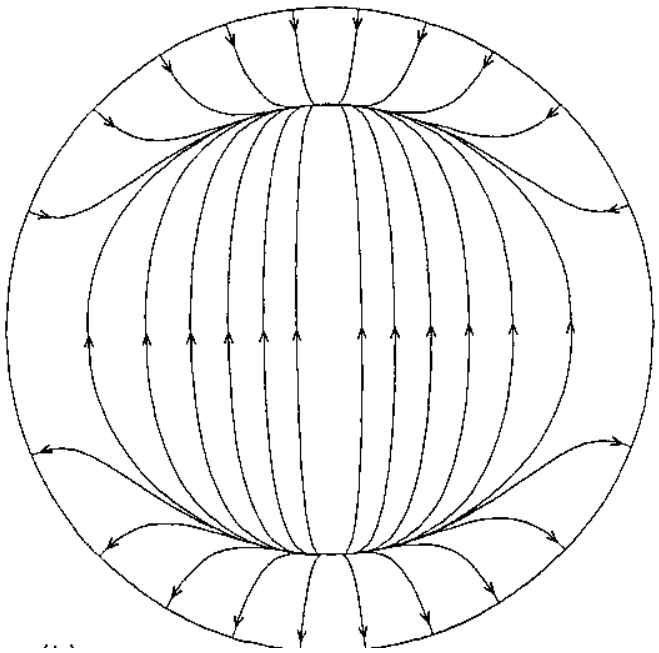

Figure 2.12: The m = 1 electric fields from Chen [53].

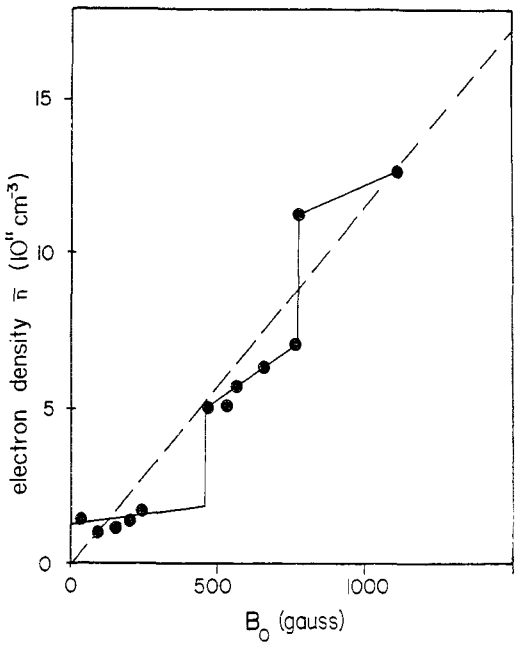

Figure 2.13: Electron density versus magnetic field strength from Boswell [22].

2.4.1 The helicon dispersion relation

The linear relationship between density and magnetic field strength is predicted by the typical helicon dispersion relation, which is derived here as per Chen [53]. The relevant equations are the electron equation of motion (equation 2.13)

$$m_e \frac{\partial \vec{v_e}}{\partial t} = -e(\vec{E} + \vec{v_e} \times \vec{B_0}) - m_e \nu \vec{v_e} \tag{2.13}$$

where B_0 is the background axial magnetic field and ν is the electron collision frequency, and Ampere's law and Faraday's law (equations 2.14 and 2.15).

$$\nabla \times \vec{E} = -\frac{\partial \vec{B}}{\partial t} \tag{2.14}$$

$$\nabla \times \vec{B} = \mu_0 \vec{J} \tag{2.15}$$

Assuming changes in the fields and velocities go as $exp(ikz - i\omega t)$ (where k is the wavenumber and ω is the wave angular frequency) then linearizing the equations and solving for a vector differential equation in $\vec{B}$ yields

$$(\beta_1 - \nabla\times)(\beta_2 - \nabla\times)\vec{B} = 0 \tag{2.16}$$

where β_1 and β_2 are given by the roots of

$$(\omega + i\nu)\beta^2 - k(eB_0/m_e)\beta + \omega\omega_{pe}^2/c^2 = 0 \tag{2.17}$$

where ω_{pe} is the electron plasma frequency ($n_0 e^2/\epsilon_0 m_e$). The helicon solution is given by β_1 which, when $\omega_{ce} \gg \omega$ ($\omega_{ce} = eB_0/m_e$) is given by

$$\beta_1 = e\mu_0 \frac{n_0}{B_0} \frac{\omega}{k}. \tag{2.18}$$

Since β_1 is a constant, a linear relationship between n_0 and B_0 is apparent. In typical experiments, ω is determined by the rf frequency applied to the antenna, and k is determined by the antenna size. The wave fields given in figures 2.11 and 2.12 are obtained by solving for $\vec{B}$ in equation 2.16 in cylindrical geometry.

2.4.2 Helicon discharge equilibria

In the 1990s Chen et al. [55, 56, 94] investigated overall helicon discharge equilibria as a function of magnetic field strength and orientation relative to the rf antenna. They measured plasma parameters using a Langmuir probe on the axis of a helicon discharge from the antenna to the downstream axial boundary. In all cases they observed a localized peak of hot electrons with $T_e \approx 4.5$ eV [94]. They subsequently observed a downstream peak in density. An example set of data is shown in figure 2.14. Estimating the plasma

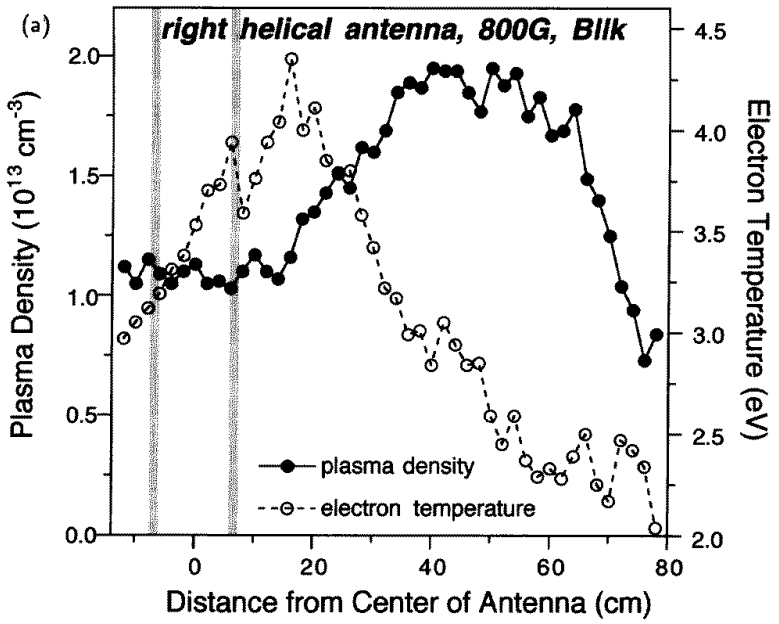

Figure 2.14: Plasma density and electron temperature versus distance from the center of the rf antenna [94].

potential with the Langmuir probe traces they determined that no major axial potential structures existed in the plasma. An example dataset is shown in figure 2.15.

Chen et al. argued that the electron temperature profile is due to a local electron heating mechanism, though the mechanism itself was not identified. The T_e decay profile was simply due to electron heat conduction and inelastic collisions with neutrals. As per Chen

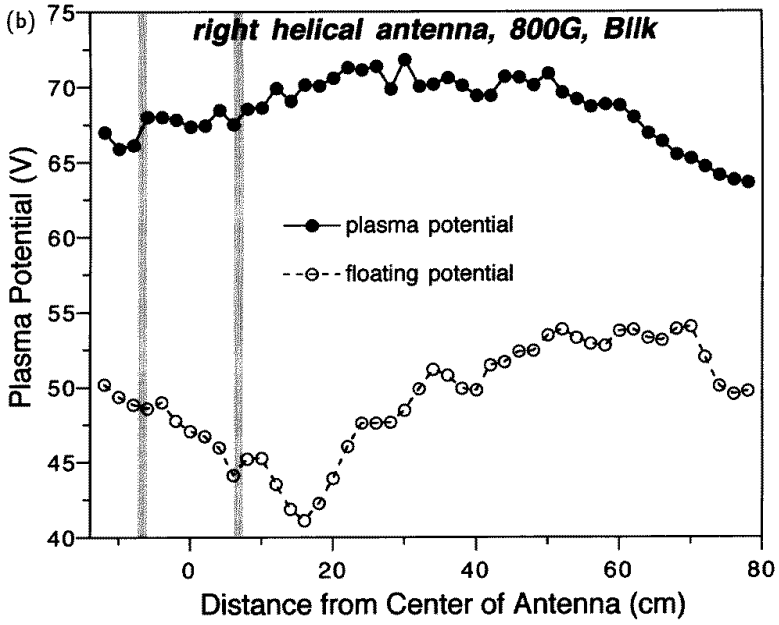

Figure 2.15: Plasma potential and floating potential versus distance from the center of the rf antenna measure by a Langmuir probe [94].

et al. [94] the electron heat flow is given by

$$\frac{\partial q}{\partial z} = Q(T_e(z)) \tag{2.19}$$

where q is the heat flux, z is the axial spatial coordinate, and Q is the heating rate due to rf heating and inelastic collisional cooling. q is given by

$$q = -2.4 \frac{1}{e^4 ln(\Lambda)} \frac{T_e^{5/2}}{\sqrt{2\pi m_e}} \frac{\partial T_e}{\partial z} \tag{2.20}$$

where $ln(\Lambda)$ is the Coulomb logarithm (~ 10 in typical low temperature plasmas). Using tabulated values for $Q(T_e)$ Chen et al. numerically integrated equation 2.19 using data for initial conditions and found a good fit. The results are shown in figure 2.16.

Given these results Chen et al. argued that the downstream density peak existed to maintain a pressure balance with the hot electrons and the electric fields such that

$$-en_e\vec{E} - \frac{\partial p_e}{\partial z} = 0 \tag{2.21}$$

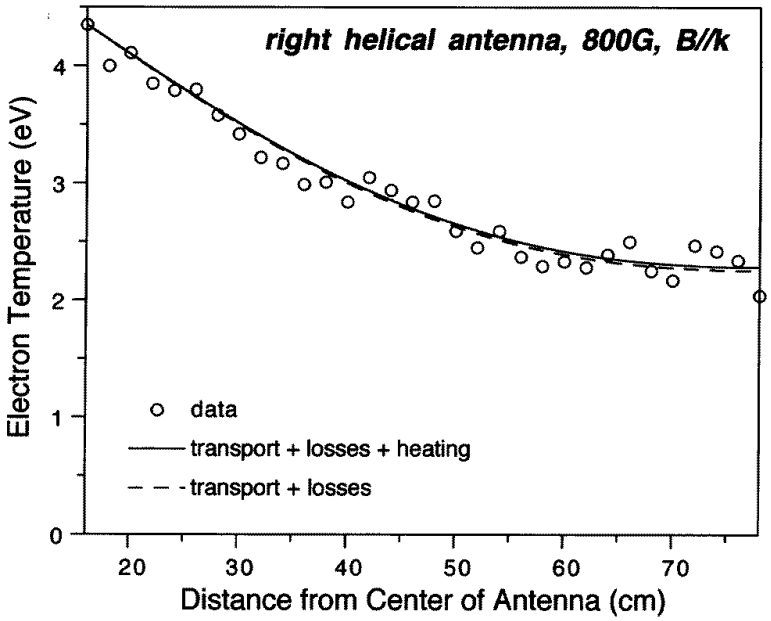

Figure 2.16: Electron temperature versus distance from the center of the antenna, data and numerical model taking into account different sources and sinks of heat [94].

where p_e is the thermal electron pressure. Checking this hypothesis against the data (presented here in figure 2.14) they found that equation 2.21 was approximately equal to zero over four antenna lengths, after which the data no longer agreed. This has since been the standard understanding of overall helicon discharge equilibria.

2.4.3 Ionization and heating in helicon discharges

The ionization mechanism of helicon waves in the plasma is a topic that has been debated since Boswell's seminal paper [22]. One of the first theories was Landau damping of the helicon wave on the electrons. It was noted by Chen [53] that the helicon wave's phase speed was slightly slower than the optimal electron speed for neutral impact ionization . Thus the wave could collisionlessly damp on the electrons, accelerating them to a speed where the ionization cross section is large, producing more plasma. Using

Langmuir probes, R. Chen and Hershkowitz [57] found evidence of electron beams in a multi-mode helicon discharge, where the beam energies agreed well with the waves' phase velocities. Chen and Blackwell [58] showed that the population of electrons accelerated by Landau damping is not sufficient to account for the ionization efficiencies commonly observed. Instead they proposed that the wave which satisfied the β_2 root in equation 2.16, the Trivelpiece-Gould wave, which can strongly damp on the electrons, could account for the helicon's ionization mechanism [59]. They argued that the helicon wave can mode-convert to the TG wave near the edge of the plasma downstream from the antenna. The TG wave is strongly damped and propagates inward, depositing energy efficiently throughout the discharge [58].

Despite the fact that Landau damping cannot account for the high ionization fractions observed in helicons, significant wave trapping can still occur in regions near the antenna where capacitively coupled electric fields can be significant. Wave trapping creates beams of electrons in phase with the applied rf frequency that can subsequently thermalize downstream due to collisions with neutrals, ions, and instabilities [58]. Hence Landau damped electrons can be a source of hot electrons in helicon sources, especially near the rf antennas.

Another theory for helicon ionization was proposed by Akhiezer et al., where the helicon wave acts as a pump wave for a parametric instability that produces ion sound waves [60]. These waves can have wavelengths of the order of the electron gyro radius (ρ_e) and can then scatter off of and deposit energy to the electrons creating hot populations, increasing ionization. The authors argue that this mechanism could account for much of the helicon wave's plasma production. Furthermore they showed that the electron temperature peak location observed by Chen et al. [55, 94] can potentially be explained by parametric instabilities generated by the helicon pump wave, given the experimental data provided. Kline et al. later measured the power spectrum of electrostatic fluctuations as a function

of rf pump frequency and position and found “sideband” modes that are characteristic of parametric instabilities [61]. These modes’ frequencies agreed with expected ion sound wave frequencies. Their data are presented in figure 2.17.

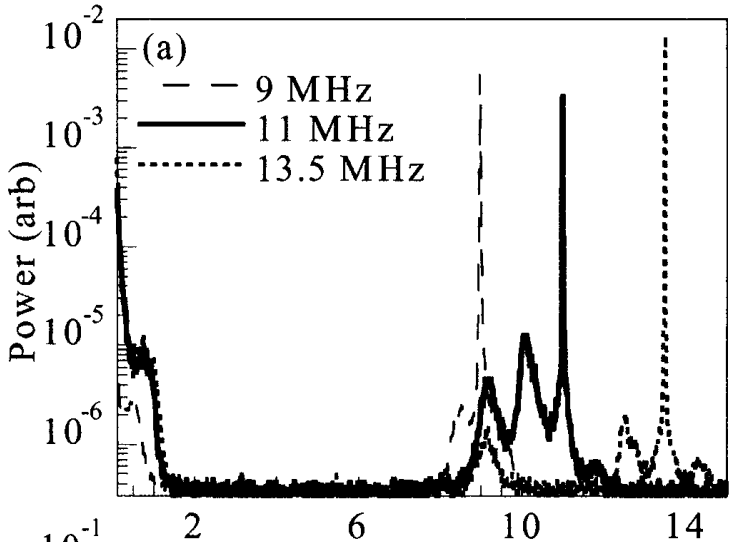

Figure 2.17: Electrostatic fluctuation power spectrum vs. frequency for different pump wave frequencies [61].

2.4.4 Turbulence & ion temperature anisotropy in helicon discharges

The turbulence in helicon discharges affects different aspects of the plasma ions. Using high spatial resolution laser-induced fluorescence (LIF) in three dimensions, Scime et al. [62] observed helically flowing ions downstream from a helicon antenna. An example dataset is given in figure 2.18. In this figure the neutral pressure was 3.8 mTorr, the rf frequency was 9.5 MHz and the magnetic field strength was 652 G. The bottom color plot gives the magnitude of the LIF signal and the top color plot gives the magnitude of the ion flow speed in the z (parallel to magnetic field) direction. Chakraborty Thakur et al. [66] measured sheared azimuthal ion flow profiles that depend on axial magnetic field strength. Their results are presented in figure 2.19 The authors observe azimuthal ion flows that,

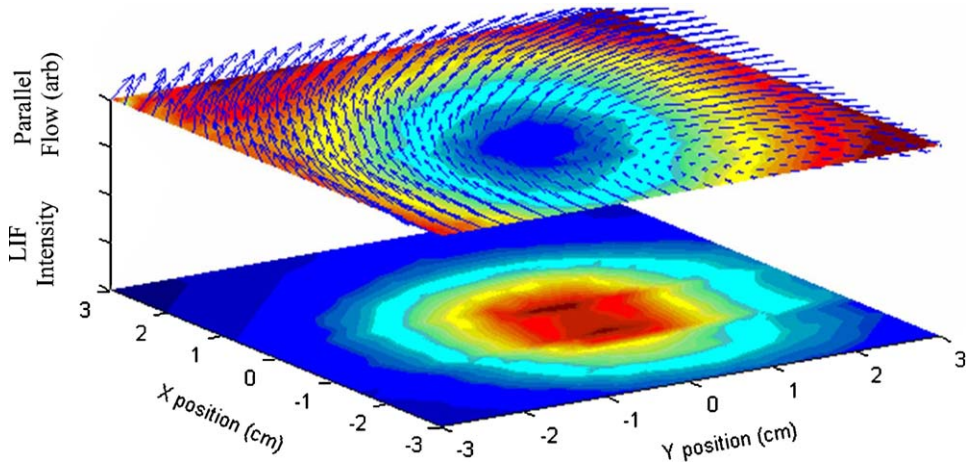

Figure 2.18: Ion flow speed in three dimensions in a helicon discharge [62].

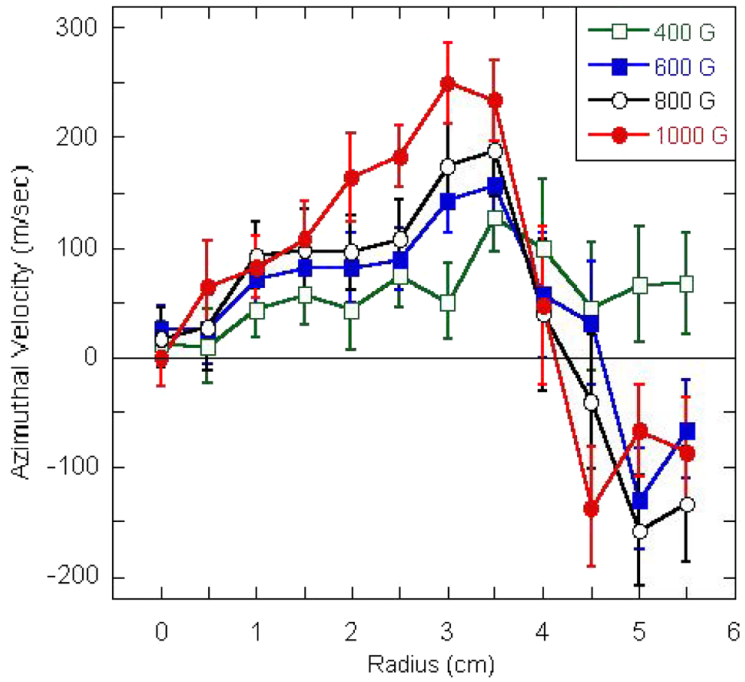

Figure 2.19: Ion flow speed vs. plasma radius for several magnetic field strengths in a helicon discharge [66].

when the axial magnetic field strength is greater than 400 G, changes direction at radii greater than 4 cm. The sheared azimuthal flows are correlated with the onset of drift wave turbulence, a centrally peaked density profile, and a radial ion temperature gradient.

Scime et al. also report on observed ion temperature anisotropy in helicon discharges [63]. The temperature anisotropy depends on magnetic field strength and neutral density. Example data are given in figures 2.20 and 2.21. Mikhailenko et al. [64] suggest that this

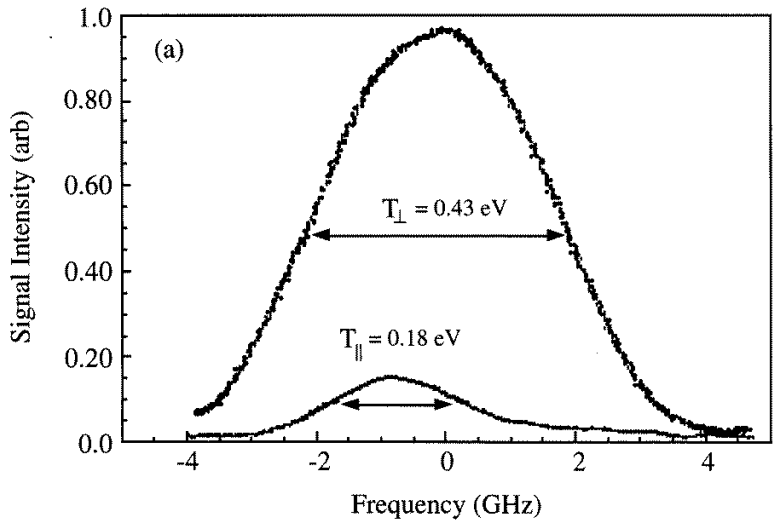

Figure 2.20: LIF signal vs. laser frequency parallel and perpendicular to axial magnetic field from Scime et al. [63].

temperature anisotropy could be due to the same parametric decay of the helicon pump wave into ion sound turbulence. They mathematically show at short wavelengths the ion sound waves are spectrally anisotropic. These short wavelength sound waves then scatter on ions, heating the ions predominantly across the magnetic field. The authors also suggest that the Trivelpiece-Gould waves (the β_2 solution from equations 2.16 and 2.17) can also excite parametric ion sound turbulence perpendicular to the axial magnetic field.

Another possible source of ion temperature anisotropies is the ion Landau damping on the TG waves [61]. Scime et al. [65] also made short wavelength power spectrum

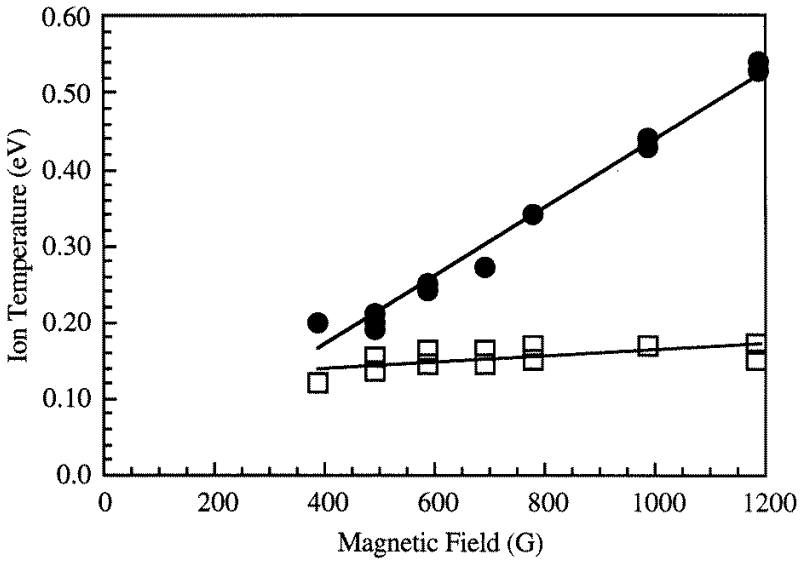

Figure 2.21: Perpendicular (circles) and parallel (squares) ion temperatures from LIF vs. axial magnetic field strength in a helicon discharge from Scime et al. [63].

measurements using a double probe and Thompson scattering apparatus at the edge of a helicon discharge. They observe short wavelength fluctuations at the plasma edge when the pump frequency in close to the lower hybrid frequency. They correlate this with previous observed perpendicular ion heating under the same experimental conditions [61]. Furthermore, using a pulsed helicon source, the authors observe that ion heating in the edge of the discharge occurs concurrently with an increase in electrostatic fluctuation amplitude in the same region. The wave numbers and frequencies of the observed fluctuations suggest that they are observing the parametric decay of the Trivelpiece-Gould mode into ion sound waves [65].

2.4.5 Neutral pumping in helicon discharges

One of the most interesting aspects of helicon discharges is the phenomena of radial neutral pumping. Many helicon plasmas exhibit relatively hollow neutral cores - that is the

neutral density on the axis of the discharge is less than the neutral density at the edge [67, 68]. The magnitude of this effect is very sensitive to the experimental conditions. The presence or absence of neutral pumping is known to affect power deposition from the rf antenna [69]. In the total absence of neutral particles on the axis of a helicon plasma rf input power goes to electron heating instead of further ionization. The effect of neutral pumping is thought to be caused by several factors: high ionization rates on axis, low/high ion/neutral cross field diffusion times, high ion axial diffusion times, and neutral heating in the core [70]. Because neutrals are not bound by the axial magnetic field lines they travel freely to the radial center where they are quickly ionized. Ions, then bound by the field lines, travel much more rapidly along the lines than diffuse across them. As a result they are preferentially lost to the axial boundaries in the system rather than diffusing outward radially or recombining. For relatively hollow, but not empty neutral cores, the remaining neutrals can be heated due to elastic and charge exchange collisions with hotter ions, forming a radial neutral temperature gradient. This effect sets up a radial neutral pressure balance, maintaining a sparse, hot central neutral core with dense colder neutrals outside.

2.5 Previous presheath measurements in rf plasmas

As discussed above, presheaths in quiescent plasmas exist to accelerate ions prior to entering the sheath in order to maintain a monotonic potential profile between the bulk plasma and the boundary surface. In rf discharges the plasma may not be quiet enough for one to assume that the necessity of the presheath still exists. Riemann showed that by looking at the causality of ion acoustic waves in an rf plasma sheath and presheath that the Bohm criterion must hold exactly as stated in equation 2.7 in rf produced plasmas [71].

In rf plasmas, the electric potential typically fluctuates with the plasma potential. The magnitude of the fluctuation depends on the density of the plasma and the rf discharge mode. In capacitively coupled plasmas, the density is usually low enough for the antenna's

electric fields to penetrate deep into the plasma, generating large bulk plasma potential fluctuations. In higher density discharges, the plasma potential fluctuations can be much smaller, sometime less than a few volts.

In the sheath and presheath, the potential fluctuations are amplified by the DC electric fields. In the sheaths this can lead to bimodal and non-Maxwellian IVDFs. In the presheath this effect is generally not observed because the presheath is typically collisional and because the electric fields are much smaller. Ions will also usually only see the time averaged fields as long as $\omega_{pi} \ll \omega_{rf}$, where ω_{pi} is the ion plasma frequency.

Zheng et al. [72] show that in rf plasmas, even when the ions do not react to the fluctuating potentials, that collisions in the presheath can greatly affect the ion angular distribution that hit an electrode surface. Their data are given in figure 2.22. The authors

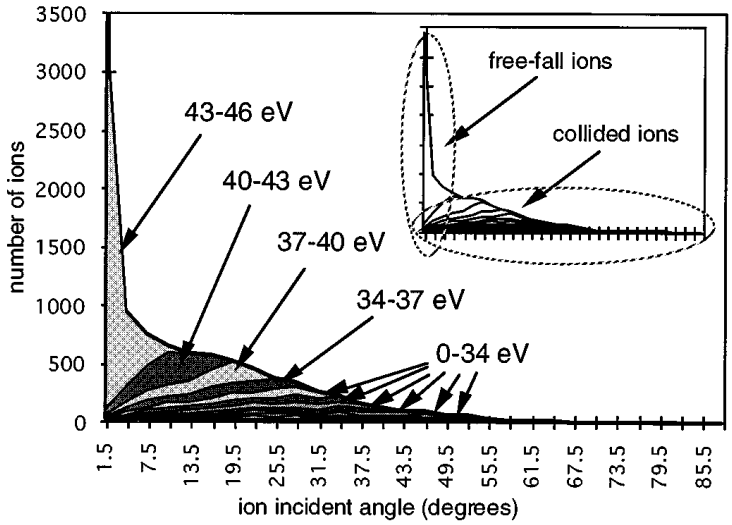

Figure 2.22: Integrated ion angular distribution at an electrode numerically calculated by the IONTRANS code by Zheng et al. [72].

claim that the large angle tail of the ion angular distribution is due to ion collisions in the presheath of the electrode. The ion angular distribution at an electrode surface is generally of significant importance in plasma processing.

There have been several works performed where presheaths in rf plasmas have been measured. Meyer et al. [102] measured the plasma potential with emissive probes in front of a grounded wafer stage in an electron-cyclotron resonance device. By estimating the presheath start and end by changes in slope of the plasma potential versus distance, they found that the presheath lengths were proportional to the ion collision lengths, and used this insight to predict the collision cross sections for the CF_4 ion. Their data are presented in figure 2.23. Using emissive probes the authors only measured the time averaged

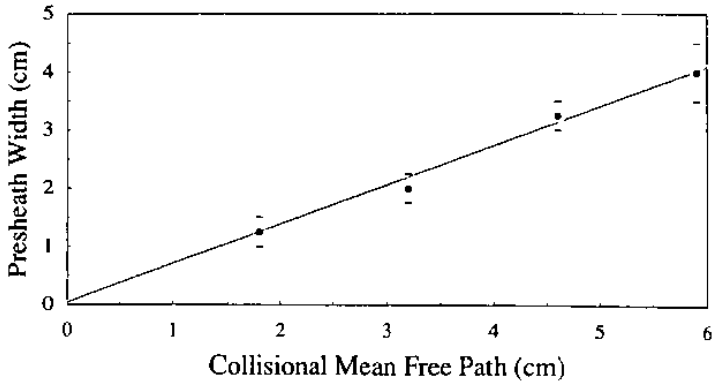

Figure 2.23: Measured presheath thickness vs. mean free path for N_2^+ ions [102].

plasma potentials in the presheath. Ion dynamics were not measured and it is unclear if the sheath-presheath boundary they identified corresponded to where the ions reached the sound speed.

Jacobs et al. [74] used LIF to measure ion velocity distribution functions above a wafer stage in an inductively coupled plasma processing chamber. Line-integrated electron density was measured with a microwave interferometer. The ions were observed to accelerate towards the wafer. Assuming the ions are collisionless near the wafer, the change in plasma potential was inferred from energy conservation of the ions. Their data are presented in figure 2.24. The inner portion of their inferred plasma potential is shown to agree well with Riemann's theory of the presheath in quiescent, weakly collisional plasmas (equation 2.10). This suggests that in this case the ions follow the time averaged plasma potentials,

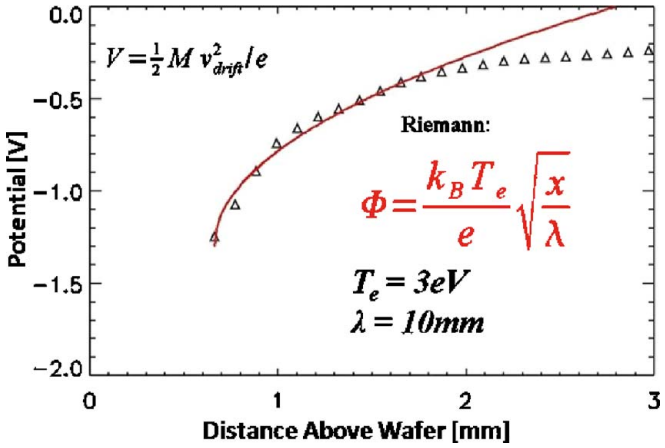

Figure 2.24: Inferred plasma potential from ion energy conservation [74].

which in turn agree well with theory of quiescent plasma presheaths.

Sun et al. [75] observe IVDFs near a grounded plate in a helicon-produced plasma. Their data are given in figure 2.25. The authors note that the ion beam acceleration occurs

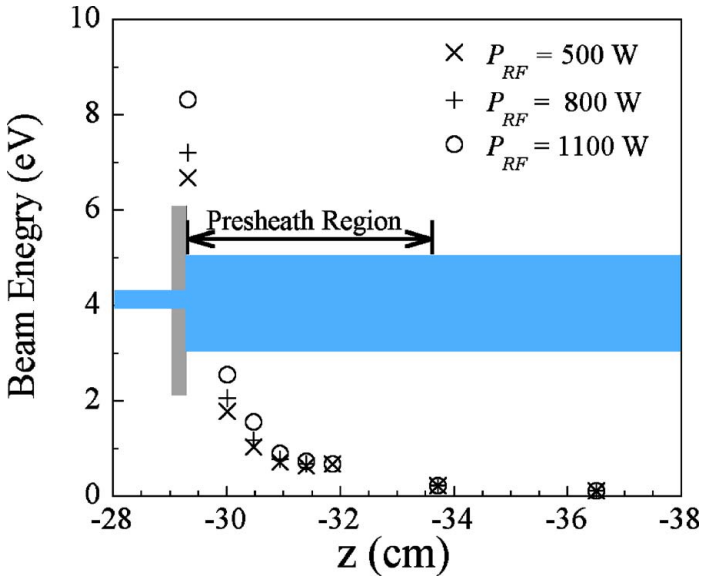

Figure 2.25: Ion energies in front of a grounded plate in a helicon plasma [75].

on a distance length of approximately the ion collision length of 3 cm. Using Langmuir

probes, they measure an electron temperature of 8 eV. Thus the authors observe the ions achieving an energy of T_e in the presheath.

Chapter 3

Experimental setup

To investigate presheaths in plasmas with significant collisions (λ less than the size of the experiment), ionization ($\nu_{iz} \sim \nu_c$), and magnetic field effects ($\rho_{i,e}$ less than the radius of the experiment), a helicon plasma source was constructed with Langmuir and emissive probes, and laser-induced fluorescence (LIF) diagnostics. The helicon source is ideal because of its background axial magnetic field, optical access, strong LIF signal, and appropriate plasma parameter regimes. Background information regarding the diagnostics, and the experimental setup of each set of measurements are described in the next sections.

3.1 Langmuir probes

Langmuir probes are one of the oldest plasma diagnostics. Simply put, a Langmuir probe is a conductor exposed to the plasma, whose total area is much smaller than the other loss areas exposed to the plasma (typically the conducting vacuum chamber walls). "Smaller" means at least as small, compared to the other loss areas in the system, as the square root of the mass ratio between the electrons and the ions [5]. The potential on the probe is swept relative to system ground, and the collected current is measured. The collected current is a function of the plasma potential, the electron and ion energy distribution functions, and the

total probe collecting area. Langmuir probe use has been reviewed by a number of authors [12, 76, 77]. The relevant background material for understanding Langmuir probes in this proposed work is presented here.

3.1.1 Planar Langmuir probes in unmagnetized, quiescent plasmas

For a collecting probe in a cold plasma where $T_e = T_i \approx 0$, the probe will collect current determined by the probe's potential relative to the plasma potential. If the probe is above the plasma potential, then no ions will be collected, and any electron that enters the probe's sheath will inevitably fall towards the probe and be collected. Above this potential no further increase in electron current is expected because the current is a function of random electron flux into the probe sheath, which is not a function of probe bias above the plasma potential. Conversely, if the probe is biased below the plasma potential, then electrons will not be collected, and any ion that enters the probe's sheath will be collected.

In typical experimental plasmas a situation where $T_e \gg T_i \approx 0$ is common. In this case, the electron current collected will depend on the electron velocity distribution function. The electron current collected by a probe in a plasma in general is given by

$$I_e = Ae \int_{v_{min}}^{\infty} dv_z \, v_z \int_{-\infty}^{\infty} \int_{-\infty}^{\infty} dv_x \, dv_y \, f_e(v_x, v_y, v_x) \tag{3.1}$$

where A is the probe's collection area, $v_{min} = \sqrt{2e(\phi - V_B)/m_e}$, ϕ is the plasma potential relative to ground and V_B is the probe bias potential relative to ground. In many low temperature plasma experiments and applications, the electron distribution function is described by a Maxwellian (equation 2.2). Using this form in equation 3.1 the collected current becomes

$$I_e = An_0 e \sqrt{\frac{T_e}{2\pi m_e}} exp\left[\frac{-e(\phi - V_B)}{T_e}\right], \; V_B \leq \phi \tag{3.2}$$

$$I_e = An_0 e \sqrt{\frac{T_e}{2\pi m_e}}, \; V_B > \phi \tag{3.3}$$

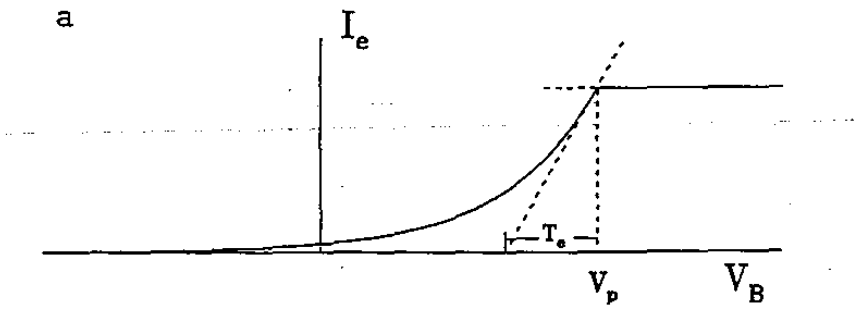

Figure 3.1: Electron current to a planar Langmuir probe with Maxwellian electrons [77]. V_p here is ϕ in the text.

Equations 3.2 and 3.3 and plotted in figure 3.1. As is seen in this figure and in equation 3.2, for $V_B < \phi$ the electron current is an exponential function of the bias voltage. Thus the natural log of this region of the I-V characteristic will yield a straight line that is inversely proportional to the electron temperature (T_e).

Figure 3.1 does not include ion current. The ion current collected will go as [77]

$$I_i = 0.6 n_0 e A v_B, \ V_B \leq \phi \tag{3.4}$$

$$I_i = 0, \ V_B > \phi \tag{3.5}$$

where v_B is the Bohm velocity given in equation 2.7. The factor of 0.6 is due to the decrease in plasma density in front of the probe due to the probe's presheath for collisionless presheaths [1]. For collisional presheaths this factor is smaller than 0.6 [5]. Because ions are much more massive, they are not accelerated to high speeds in the probes sheath compared to electrons. As a result the ion current collected is much smaller than the electron current by a factor of the square root of the mass ratio of the electrons and ions. For argon plasmas, this is approximately a factor of 200. The collected electron/ion current above/below the plasma potential is called the saturation current.

Given this information, for a planar probe in a Maxwellian plasma where $T_e \gg T_i$, the exponential part of the characteristic yields the electron temperature (after the ion current

is subtracted), the "knee" of the trace gives the plasma potential, and the ion current from equation 3.4 yields the bulk plasma density.

In reality the probe's collecting area will be governed by the expanse of the sheath around the probe. The sheath thickness will increase for increasing bias potential above the plasma potential due to its increasing collecting area. For an infinite planar probe the sheath will expand normal to the surface of the probe. Thus the collecting area of the probe relative to the plasma does not increase. For a small planar probe, when the sheath expands it will expand around the edges, eventually turning the collecting area from planar to spherical. This will cause the electron current to increase slowly as the bias voltage increases past the plasma potential, instead of remaining constant. An example trace exhibiting this is given in figure 3.2. The negative current in this figure is due to ion

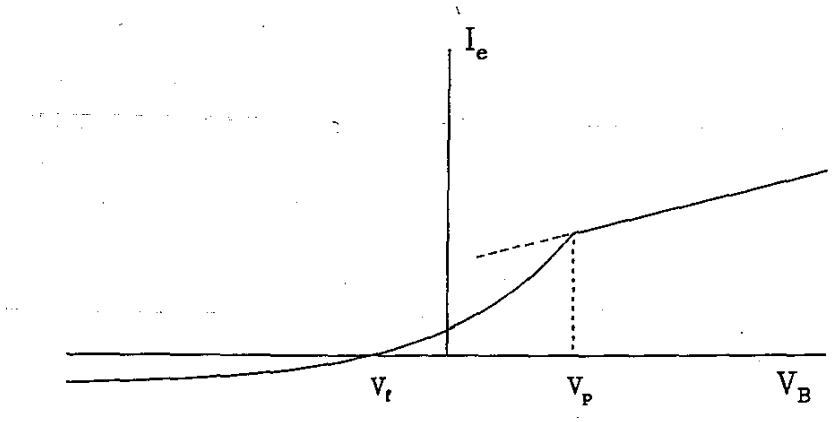

Figure 3.2: Electron current to a planar Langmuir probe with sheath expansion for $V_B > \phi$ [77]. V_p here is ϕ in the text.

current for $V_B < \phi$. Note that figures 3.1 and 3.2 are not to scale. Important features such as ion and electron current magnitudes have been rescaled to make them easier to observe.

3.1.2 Cylindrical Langmuir probes in unmagnetized, quiescent plasmas

It is often advantageous to use Langmuir probes with cylindrical geometry. Cylindrical probes can be made smaller more easily and can be less perturbing to the plasma than a comparable planar probe. It is often easier to obtain more resilient materials for withstanding plasma heat flux and sputtering in cylindrical geometry. This geometry requires more careful analysis of the current characteristic. The cylindrical geometry will create a cylindrical sheath around the probe. Due to their angular momentum, some particles that enter the sheath may then simply be scattered, instead of collected. For a collisionless probe sheath and presheath the theory that predicts collected current is called "orbital motion limited" (OML) theory [78]. Taking into account these orbital effects, this theory predicts that the electron and ion current will be given by

$$I_e \approx en_0A\sqrt{\frac{4T_e}{2\pi^2m_e}}\sqrt{1+\frac{e(V_B-\phi)}{T_e}},\ V_B<\phi \tag{3.6}$$

$$I_i \approx en_0A\sqrt{-\frac{2e(V_B-\phi)}{\pi^2M_i}},\ V_B>\phi. \tag{3.7}$$

An important caveat to this formulation is that OML theory assumes the cylindrical probe is infinitely long. In reality a cylindrical probe has a finite extent and the electron current collected by the probe tip affects the electron saturation current collected. Hoskinson and Hershkowitz [79] show that the electron saturation current for a finite cylindrical probe can be empirically fit to the following equation

$$I_e = en_0A\sqrt{\frac{Te}{2\pi^2m_e}}1.08\left(1+\frac{e(V_B-\phi)}{T_e}\right)^{\gamma},\ V_B\geq\phi \tag{3.8}$$

where γ is a fitting factor accounting for probe end effects. For an infinite probe $\gamma \rightarrow 1/2$. Hoskinson and Hershkowitz experimentally investigated the regions of $0 \leq r_p/\lambda_D \leq 2$ and $L_p/\lambda_D < 300$ and found that probe end effects were apparent for all experiments in these ranges.

When collisions are present in the probe's sheath the assumptions that precede these results are no longer valid. Another theory, called Allen, Boyd, Reynolds theory (named after its creators) describes the process of ion collection by cylindrical probes in this case [80]. This theory describes how particles in the sheath and presheath collide and move radially towards the probe, negating the orbital effects in OML theory.

Because of the different collecting geometry for planar, cylindrical, and spherical (not discussed here) probes , the electron current for $V_B > \phi$ increases at different rates for the different cases. This is shown in figure 3.3. In each case the exponential part of the

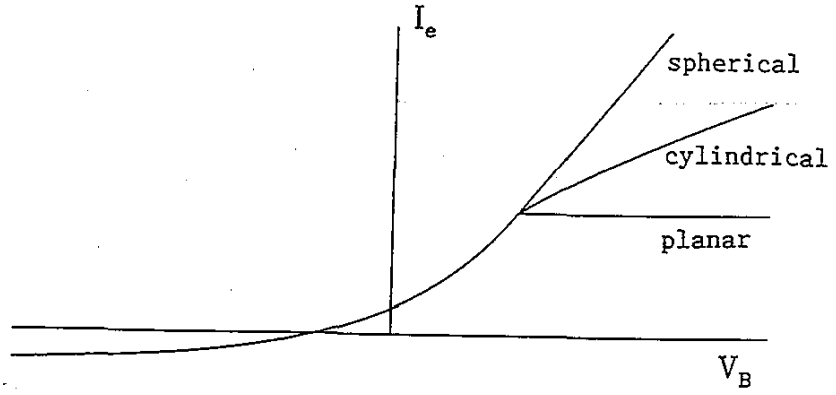

Figure 3.3: I-V characteristics for planar, cylindrical, and spherical Langmuir probes [77].

curve still yields the electron temperature, the ion current yields the plasma density, and the knee gives the plasma potential (not apparent in spherical probe traces). The form of the equation used to obtain these results may be affected by the geometry, as shown in equations 3.6 and 3.7.

3.1.3 Langmuir probes in quiescent, magnetized plasmas

Many plasmas of interested often have background magnetic fields strong enough that the electron and ion gyro radii are smaller than the dimensions of the diagnostic probes. This situation is called a "magnetized" plasma and has been review by several authors

[12, 76, 77]. The main effect of the magnetic field is to constrain electron and ion motion to along the magnetic field lines. The particles within one gyro radius of the field lines that intersect the probe have access to the probe's collecting area, thus limiting the probes total possible collection current compared to unmagnetized systems. The only way for particles outside the field lines to be collected to to collide and "jump" onto a field line intersecting the probe. For low temperature plasmas these collisions are often with neutral particles. Chen [76] calculates that this reduces the electron saturation current, which is then given by

$$I_e = \frac{n_0 \bar{v_e} A \lambda_{en}}{3 r_p} \sqrt{\frac{D_\perp}{D_{||}}},\ V_B > \phi \tag{3.9}$$

where λ_{en} is the electron-neutral collision length, r_p is the probe radius, $D_\perp$ and $D_{||}$ are the diffusion constants perpendicular and parallel to the magnetic field respectively. Because $m_e \ll M_i$, the electron gyro radius is much smaller than the ion gyro radius. Thus it is common for electrons to be magnetized and ions to unmagnetized. In this case only the reduction in electron saturation current needs to be properly accounted for.

3.1.4 Langmuir probes in rf plasmas

The main effect of radio frequency plasma generation on probe characteristics is a fluctuation of the plasma potential (ϕ) during the course of the probe sweep. For a sinusoidal rf fluctuation, the fluctuating potential will spend the most time in the extrema of the voltage cycle. The I-V characteristic will then have two "knees". An example trace is give in figure 3.4. In this figure I_e^* is the electron saturation current and the effect of the rf fluctuation is obvious. In denser plasmas, the plasma will more completely shield out the rf electric fields reducing the peak to peak fluctuations of the plasma potential. The Langmuir probe traces may then deceivingly appear to be normal I-V traces, except with a slightly hotter electron temperature [81]. Traces in dense rf plasmas must be analyzed carefully in order to account for falsely hot electrons.

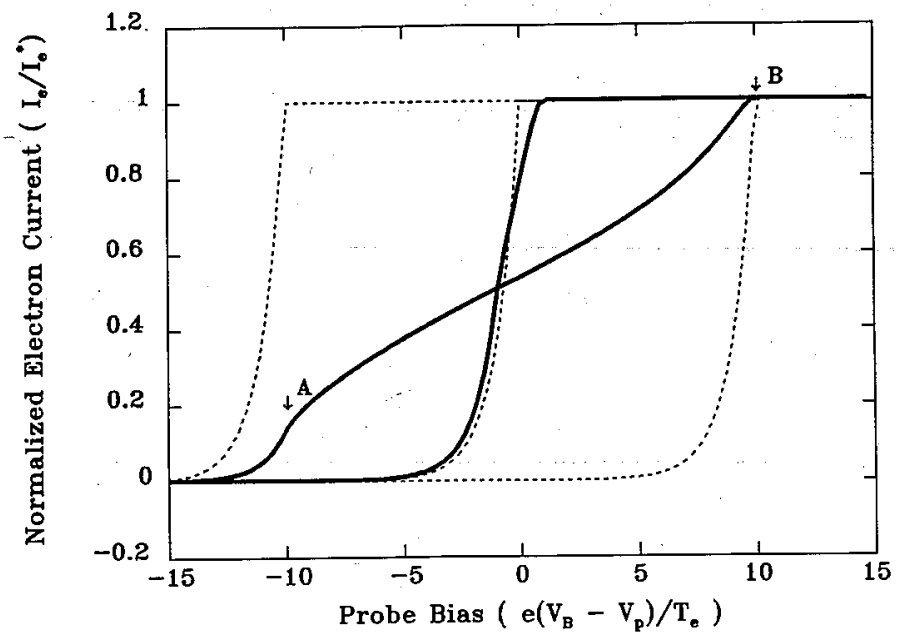

Figure 3.4: I-V characteristic for Langmuir probe in an rf plasma with a sinusoidal plasma potential fluctuation for two different rf fluctuation amplitudes [77]. The dashed lines represent probe traces if the plasma potential were fixed at the extrema or midpoint of the rf cycle. V_p here is ϕ in the text.

Oksuz et al. [82] claim that the electron temperature can be accurately measured by looking at the most negative V_B part of the exponential region of a probe trace. During this part of the trace, only the highest energy electrons will be collected by the probe. For these electrons, the changes in their energy due to the potential fluctuation is relatively small compared to their mean energy. If these electrons are representative of the bulk electron energy distribution, then their temperature will accurately represent the total electron temperature, undistorted by the rf fields.

If the frequency of the rf fluctuation is known, it is possible to mitigate the effects on the probe trace by introducing an rf choke into the probe circuit. A choke is simply a tank circuit in series between the probe and the bias supply that is tuned to have a very large impedance (typically $\sim$ 100 kΩ) at the rf frequency, and its harmonics. If the impedance

of the choke is sufficiently large, the subsequent traces can then be analyzed as if rf fluctuations are not present [81, 86].

3.1.5 Langmuir probe interpretation of bi-Maxwellian EEDFs

In many situations, the electron energy distribution function (EEDF) is made of the sum of two distinct Maxwellian populations with different temperatures and densities. Such phenomena are frequently observed in filament-produced discharges [83] and Hall thruster plume plasmas [84]. In many cases one electron population will be significantly hotter than the other. This lends itself to analyzing the electrons in terms of a hot population with temperature T_h and a cold population with temperature T_c. Because the slope log of the I-V trace, after the ions are subtracted, is inversely proportional to the electron temperature, two distinct straight-line regions are observed in the exponential part of the trace. An example is shown in figure 3.5.

To analyze these traces, the log of the full I_e trace is taken, as shown in figure 3.5. A straight line is fit to the region with lesser slope. This region extends to more negative bias as the hotter electrons continue to get collected by the probe at less biases than the cold electrons. The inverse of the slope of this region (red line in figure 3.5) yield the hot electron temperature, T_h. Taking the exponential of the fit to the hot electrons yields the I-V trace of the hot electron population. Subtracting this from the total electron I-V trace yields the characteristic due solely to the cold population. Taking the log of that trace (shown by the dashed line in figure 3.5), and then measuring the inverse of the slope of the straight line region (the blue line in figure 3.5) yields the cold electron temperature.

The contribution of the hot and cold populations to the total density can also be calculated. From equation 3.3 we have

$$\frac{I_h^*}{I_c^*} = \frac{n_h\sqrt{T_h}}{n_c\sqrt{T_c}} \equiv R \tag{3.10}$$

where $I_{h,c}^*, n_{h,c}$ is the hot/cold electron currentat the plasma potential and hot/cold electron

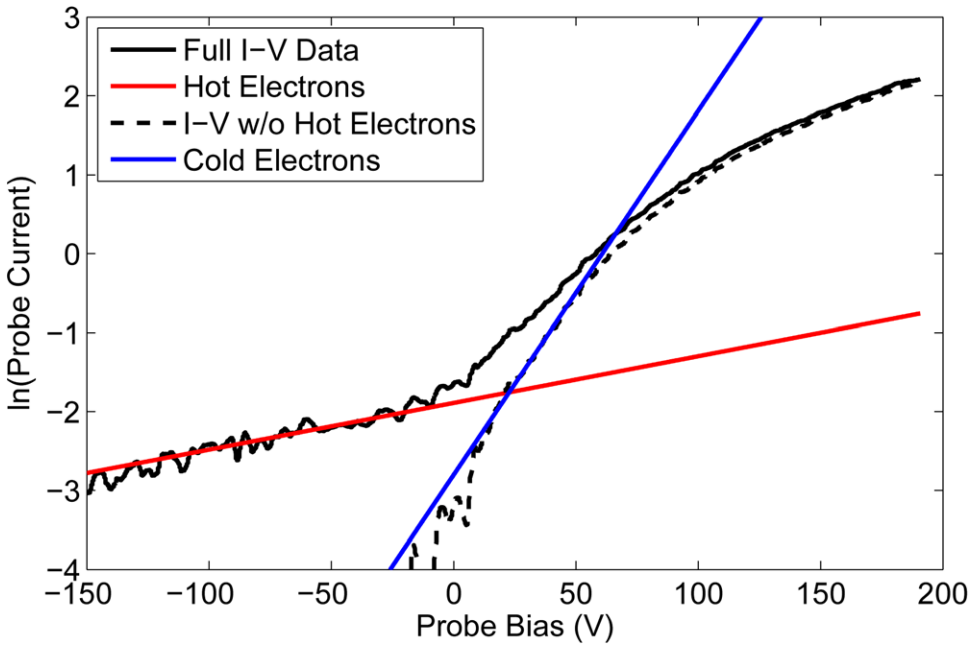

Figure 3.5: I-V characteristic for Langmuir probe in a plasma with bi-Maxwellian electrons [84].

density. Defining this ratio to be R and realizing that $n_c + n_h = n_o$ we have

$$\frac{n_h}{n_o} = \frac{R\sqrt{T_c/T_h}}{1 + R\sqrt{T_c/T_h}} \equiv \alpha. \tag{3.11}$$

The total density can be calculated as usual from the ion saturation. For the purposes of calculating the ion sound speed, c_s, an effective temperature is defined as

$$\frac{1}{T_{eff}} = \frac{1-\alpha}{T_c} + \frac{\alpha}{T_h} \tag{3.12}$$

where T_{eff} is the effective temperature. This definition of effective temperature has been shown to be an accurate for calculating the ion sound speed [85]. It is important to note that the calculation of n_o from the ion saturation current depends on α, which itself is a function of n_o. It is simple to guess correct values of alpha and recursively check its validity using the ratio of hot to total electron saturation currents as an initial guess for α.

3.2 Emissive probes

3.2.1 Emissive probes in unmagnetized, quiescent plasmas

An emissive probe is essentially a Langmuir probe whose surface is heated until it thermionically emits electrons. The probe can be heated Ohmically using an isolated power supply, via a laser beam, or Ohmically through collection of electron current from the plasma. When the probe's bias is below the plasma potential, these emitted electrons will leave the probe and enter the plasma. This will appear as negative current on an I-V trace. When the probe bias is above the plasma potential the emitted electrons will return to the probe, and the probe will act as a normal Langmuir probe. The emitted electrons are generally colder than the plasma electrons, thus the change from negative to positive current in the I-V characteristic is usually very dramatic. Thus the inflection point of an emissive probe trace is a very good estimate of the plasma potential. An example emissive probe trace is given in figure 3.6 where T_W is the wire temperature.

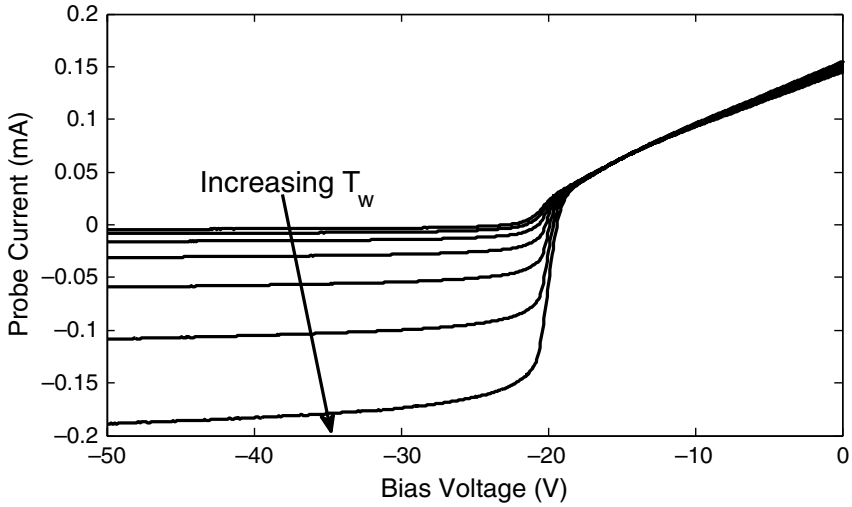

Figure 3.6: An example emissive probe I-V trace for different wire temperatures (T_W) [87].

In this figure, the negative current increases in magnitude with increasing wire temperature because more electrons are thermioncally emitted the hotter the wire is. Emissive probes have been recently reviewed by Sheehan and Hershkowitz [87]. The authors show that the inflection point of the I-V trace at large T_W occurs slightly off from the plasma potential because of space charge effects around the probe from the emitted electrons. Thus the inflection point in the limit of zero emission has been shown to be an accurate and robust method for measuring the plasma potential [87].

The inflection point in the limit of zero emission is not the only way to calculate the plasma potential. In 1966 Kemp and Sellen [88] showed that as the emission of the probe was increased its floating potential approximated the plasma potential. An example dataset is given in figure 3.7. This method, along with others, was later compared with the inflec-

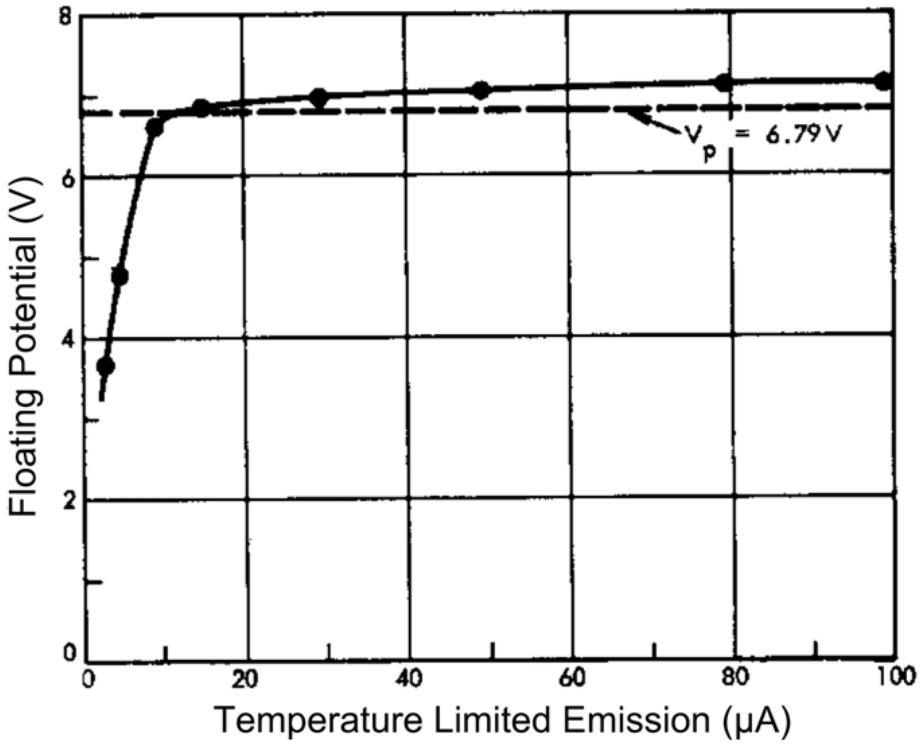

Figure 3.7: Emissive probe floating potential for increasing wire temperature [87].

tion point method by Sheehan et al. [84] and shown to be accurate within $\sim 2T_e/e$.

3.2.2 Emissive probes in magnetized and rf plasmas

The effect of a magnetic field on an emissive probe is to limit its collected electron current. Because the magnitude of the emitted electron current is a function of T_W large emitted current can still be achieved in a magnetized system. Thus the inflection point at the plasma potential is still easily discernible, and the inflection point in the limit of zero emission is still an accurate measure of the plasma potential.

In an rf plasma, just as with a Langmuir probe, the I-V trace will have two knees due to the fluctuating plasma potential. These knees will be more pronounced than with a Langmuir probe due to the emitted electron current. Wang et al. [89] have shown than an emissive probe trace using the inflection point method can be an accurate measure of the time averaged plasma potential and the peak to peak fluctuation of the plasma potential. An example dataset is given in figure 3.8. In this figure $< I >$ is the time averaged value of the electron current collected. The different traces are for different plasma potential fluctuation amplitudes. The spacing between the peaks in the derivatives in the bottom panel gives the peak to peak fluctuations and the mean value of the peaks' potentials gives the time averaged plasma potential.

3.3 Laser-induced fluorescence

Laser-induced fluorescence is an absorption spectroscopy method involving the excitation of plasma ions to a higher energy level using a laser, observing the light from the ion's relaxation, and using the Doppler shift of the absorbed photons to measure ion temperature and flow speed. LIF was first used to diagnose plasma ions by Uzelac and Leis in 1992 [90]. Severn et al. [91] proposed a scheme with diode lasers that is very useful for investigating singly-ionized argon ions in low temperature plasmas. In their scheme the argon ion $3d\,^4F_{7/2}$ metastable state is excited by a photon of wavelength 668.614 nm to

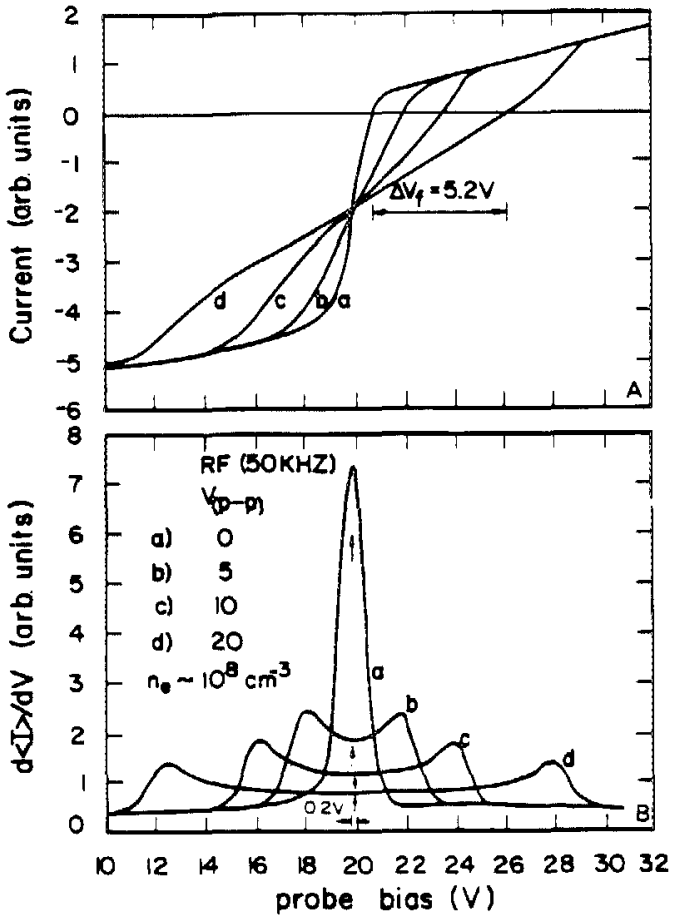

Figure 3.8: Emissive probe I-V trace in an rf plasma for different plasma potential fluctuation amplitudes [89]. The upper panel gives the raw I-V characteristics and the bottom panel shows the derivatives of the I-V traces.

the $4p\,^4D^0_{5/2}$ state, which then preferentially decays to the $4s\,^4P_{3/2}$ state emitting a photon with wavelength 442.72 nm. An energy level diagram describing this transition is given in figure 3.9.

The argon ions move due to thermal energy and due to flows in the plasma. The exciting laser is swept in frequency and the emitted light intensity is measured as a function of sweep frequency. The resulting curve is related to the ion velocity distribution function and can be used to measure the ion temperature and bulk flow speed. It is important to

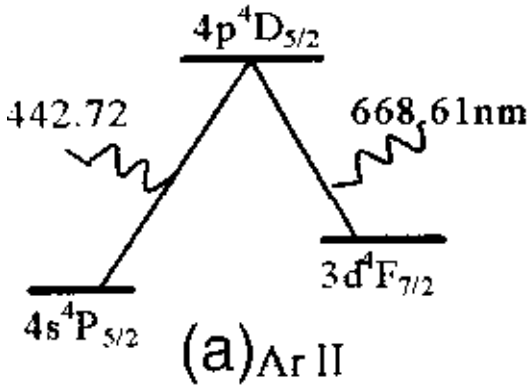

Figure 3.9: Energy level transition diagram for LIF scheme used [92].

note that the laser excites the argon ions from one metastable state to another ($3d\,^4F_{7/2} \rightarrow 4p\,^4D^0_{5/2}$). It is assumed that the IVDF of these states accurately describes the IVDF of the ground state argon ions.

The curve obtained from LIF will be widened due to the laser's natural line width in frequency space, the Doppler broadening of the ion population, and due to quantum uncertainty in the decay time of the argon ion. As long as the ion temperature is much more significant than the laser line width and the quantum uncertainty, the argon emitted light intensity versus laser frequency will be directly proportional to the IVDF. The frequency simply needs to be converted into ion velocity using the usual light Doppler shift equation [26] given in equation 3.13 below

$$\frac{f}{f_0} = \left(1 + \frac{v_i}{c}\right) \rightarrow v_i = c\left(\frac{f}{f_0} - 1\right) \tag{3.13}$$

where c is the speed of light in vacuum, f is the Doppler shifted frequency seen by the moving ion and f_0 is the frequency seen by a stationary ion, in this case 668.6144 nm.

In a magnetized plasma the argon ion energy levels given in figure 3.9 will undergo Zeeman splitting. This increases the possible excitation sequences the ion can undergo. For the relevant metastable states the Zeeman transitions are the $\Delta m = 0$, or the π transition (where m is the magnetic orbital quantum number) and $\Delta m = \pm 1$, or the σ tran-

sitions. The resulting broadening due to the σ transition Zeeman splitting is significant compared to the Doppler broadening and must be taken into consideration [92]. One way to correct for this effect is to utilize the fact that the σ transition light absorbed along the magnetic field must be circularly polarized. By injecting laser light with a fixed circular polarization, selective excitation of one of the σ transitions can be achieved. Thus instead of the resulting emission light being Zeeman broadened, they are simply shifted in energy due to the Zeeman splitting of either $\Delta m = +1$ or $\Delta m = -1$, depending on the polarization of the light injected. The resulting frequency shift of the ions is easily calculated and is provided in a useful formula from Keesee et al. [92] as $\Delta f = \pm$ 1.4 GHz/kG, where Δf is the frequency shift of the IVDF in frequency space, and kG is the magnitude of the background magnetic field in the system in thousands of Gauss. The π transition only absorbs/emits light linearly polarized light perpendicular to the magnetic field line, with the axis of polarization aligned with the magnetic field. Thus for perpendicular IVDF measurements, only appropriately angled linearly polarized light is injected. There is no frequency offset for the π transition as it corresponds to $\Delta m = 0$.

3.4 Description of the experimental apparatus

3.4.1 Vacuum chamber

Figure 3.10 shows an annotated picture of the experimental apparatus used for all the experiments presented here. The vacuum chamber consists of a 10 cm ID 1 m long Pyrex tube attached to a Pyrex cross tee. The tube sits in the center of 6 water cooled electromagnet pancake coils used for generating axial magnetic fields in the system. The coils together can carry up to 700 amps DC current generating an axial magnetic field of up to 1 kG. The coils and cross tee are wrapped in grounded aluminum mesh for rf shielding. In figure 3.10 the cylindrical portion of the vacuum chamber is not visible and the

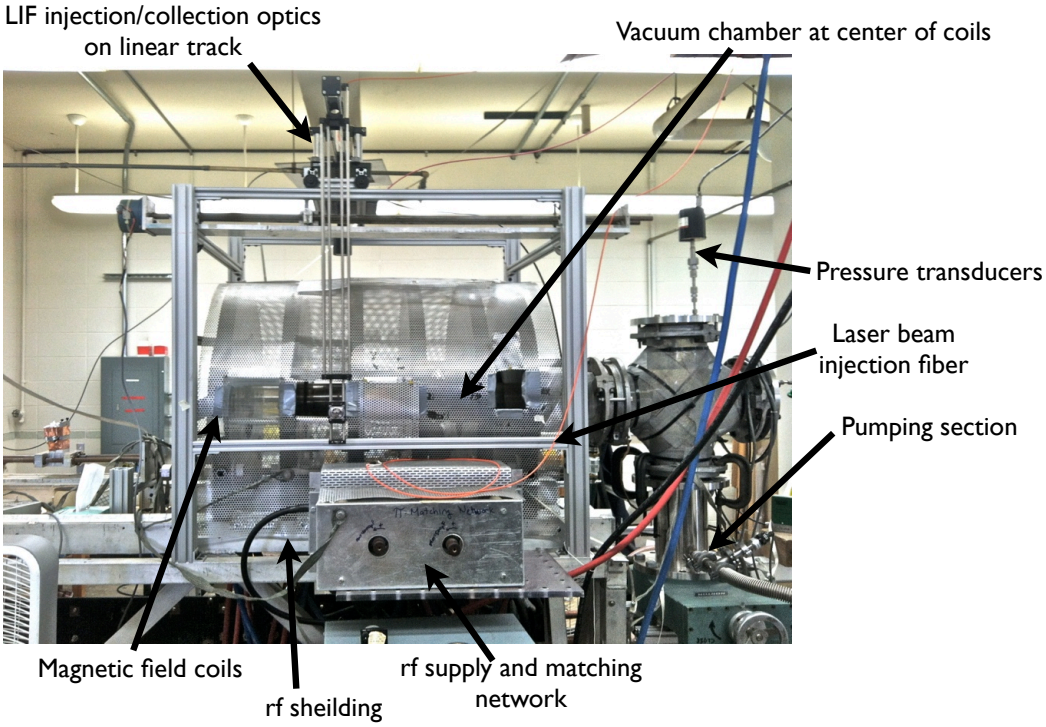

Figure 3.10: Picture of helicon apparatus with major features highlighted.

pancake coils are visible through the rf sheilding. The cross tee is seen on the right side of the image. The cross tee is attached to a turbo molecular pumping system and utilizes hot filament ionization, capacitive manometer, and thermocouple gauges for pressure measurement. The argon gas feed is attached to a flange on this side of the chamber (not visible in figure 3.10). The pumps and vacuum chamber achieve a base pressure of 7×10^{-8} torr.

An rf power supply applies 0 to 750 W of rf power to the helicon antenna via a π matching network. The applied signal is sinusoidal at 13.56 MHz. Typical return powers are less then 2 W. The helicon antenna is a 16 cm long m = -1 configuration (lower left hand corner of figure 2.10) and is hidden in figure 3.10 behind the rf shielding. A close up image of the system with the rf power supply on is shown in figure 3.11. The cylindrical Pyrex chamber is now visible along the horizontal centerline of the image. The vertical horizontal lines are the magnetic field coils. The small straps wrapped around the Pyrex

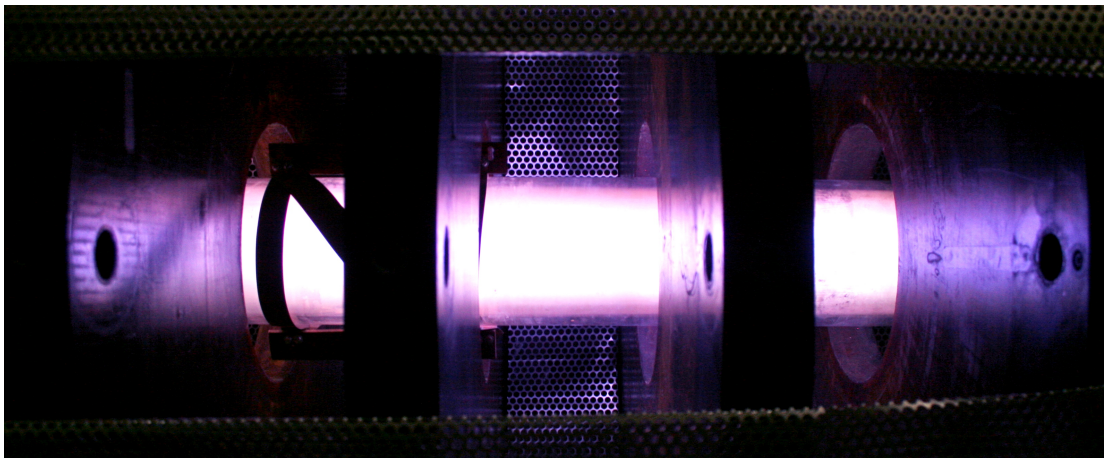

Figure 3.11: Picture of helicon apparatus with the rf supply on at 500 W and a background magnetic field of 1 kG.

chamber in the left of figure 3.11 are part of the rf antenna.

The grounded plate and probe diagnostics are inserted through the flange on the left side of figure 3.10 (the right side of figure 3.11). The probe shafts fit through a slip vacuum seal that allows for linear and rotational shaft motions. The grounded plate is held on a fixed post attached through the flange and connected to system ground. The plate position can be moved by inserting spacers of fixed length, but cannot be moved continuously like the probe shaft can.

3.4.2 Laser & optics

Figure 3.12 shows a diagram of the laser beam path prior to injection into the plasma. The Toptica laser has an output beam exiting the amplifier of 300 mW. This beam passes through two 10% beam splitters sending the beam to a Burleigh wavemeter for coarse tuning the wavelength, and a molecular Iodine (I_2) gas cell. As the laser frequency is scanned it excites the I_2 gas which has a known relaxation spectrum. This spectrum is used for absolute wavelength reference. An example I_2 spectrum is given in figure 3.13. The remaining beam power (230 mW) is sent through a Stanford Research Systems optical

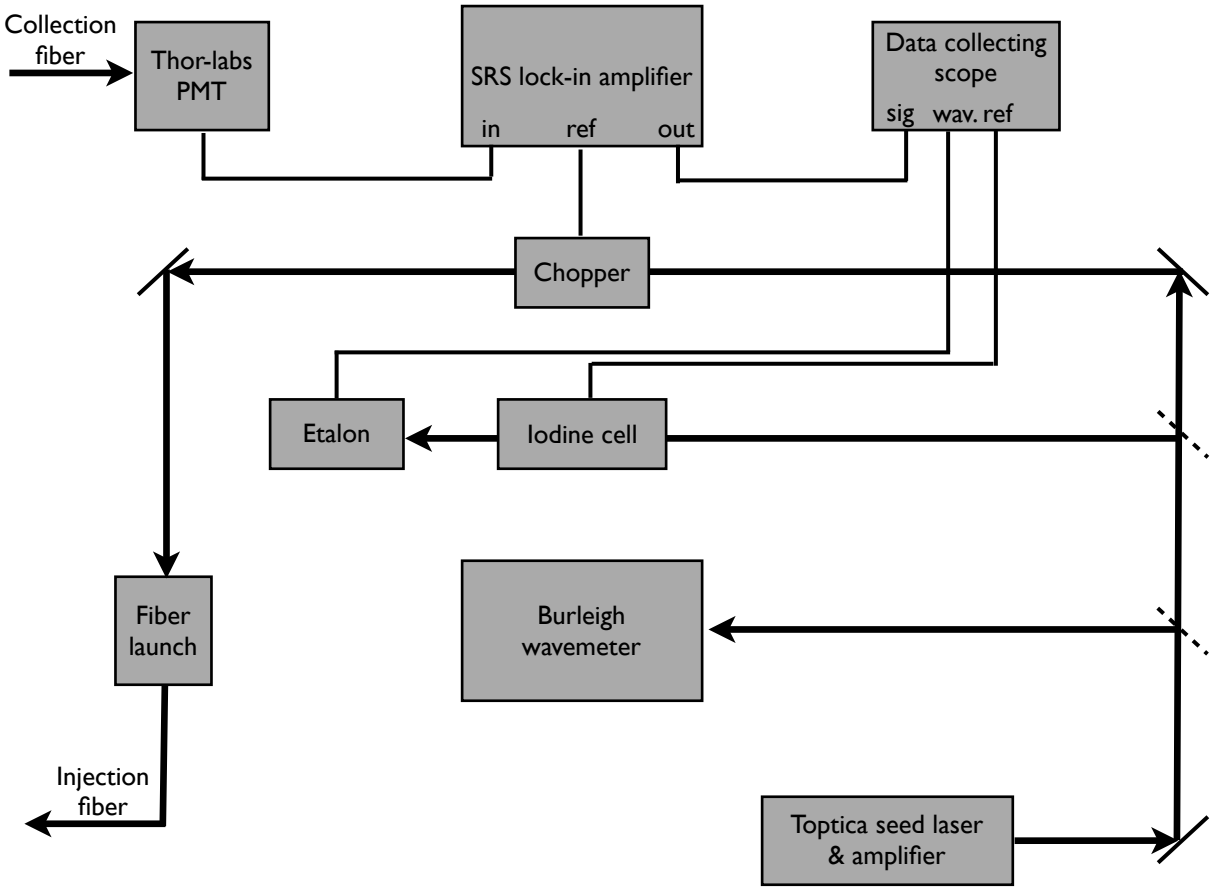

Figure 3.12: Diagram of LIF optics setup.

chopper to modulate in the input laser. The modulated signal is sent as a reference to a Stanford Research Systems lock-in amplifier, which is used to discern the fluoresced signal from the noisy plasma environment. The rest of the laser beam is then sent to a fiber launch unit that couples the laser light to the 50 μm injection fiber.

The axial pump laser beam for LIF is injected from the flange on the right side of the system as viewed in figure 3.10, via a 50 μm multimode fiber optic cable, a collimator, linear polarizer and quarter wave plate. The fast axes of the linear polarizer and quarter wave plate can be turned to create right hand circular, left hand circular, and elliptically polarized light. The laser beam can also be injected perpendicularly to the magnetic field. The perpendicular injection optic (visible in figure 3.14) consists of a fiber collimator

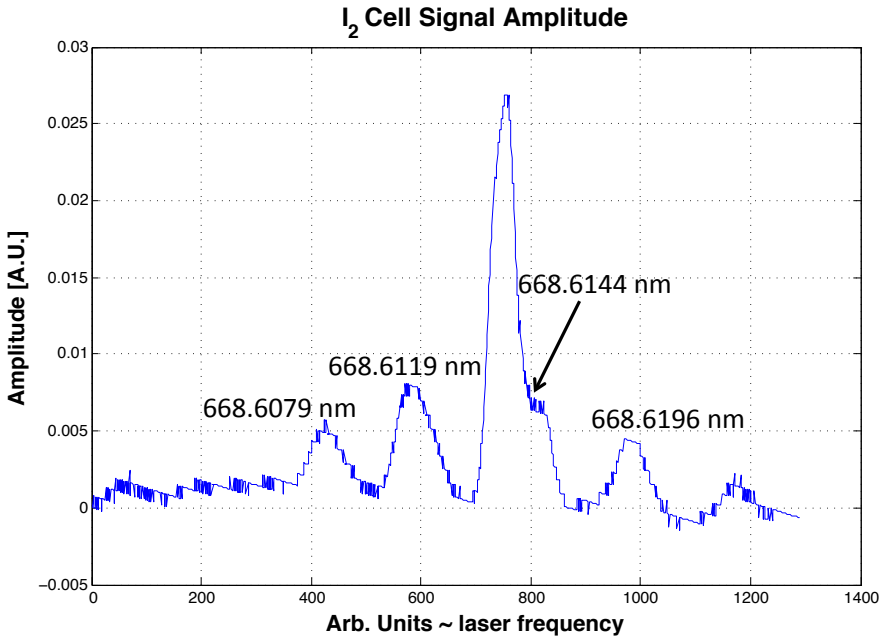

Figure 3.13: Molecular Iodine spectrum around 668.6144 nm.

and linear polarizer. The axis of the polarizer can be turned so as to align it with the background magnetic field for pumping of the π transition. The perpendicular injection optic is aligned and moves with the collection telescope (also visible in figure 3.14). The telescope consists of a 2 inch converging lens that focuses the emission light into the 100 μm return fiber.

The collected emission light is brought back to the optics bench. It is passed through a 1 nm bandwidth notch filter centered on 442 nm, and then shone on the PMT, whose output is coupled to the lock-in amplifier. The amplifier then gives the amplitude of the output signal being modulated at the chopping frequency (2 kHz). Comparing this amplitude simultaneously with the Iodine cell wavelength reference and the laser's relative wavelength reference gives the IVDF in laser frequency space. The IVDF is then corrected for the Zeeman splitting offset and displayed in velocity space.

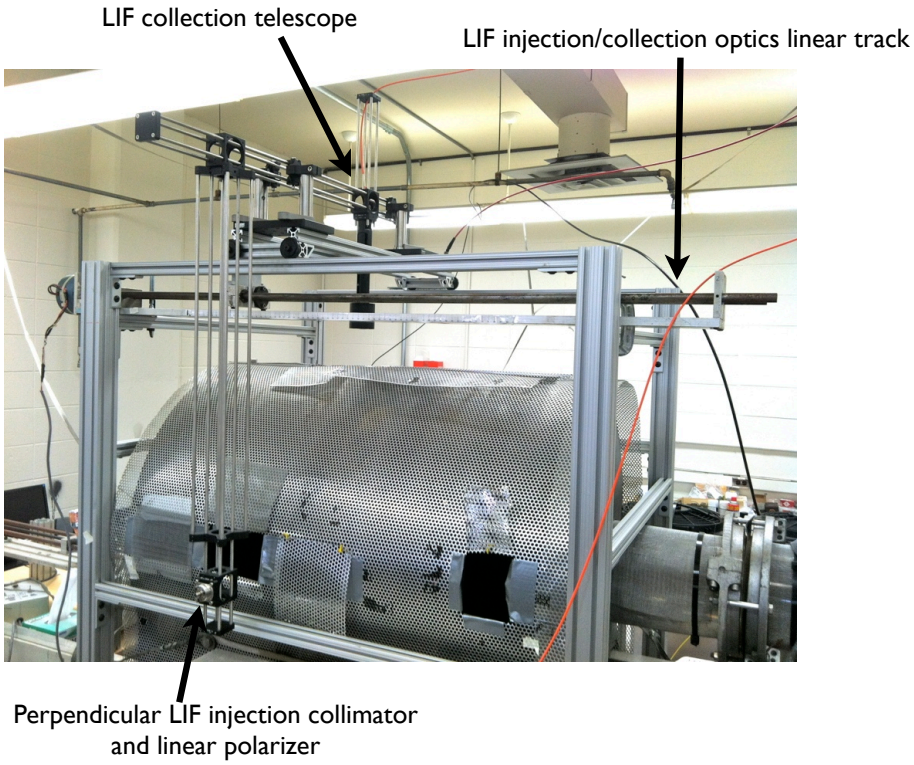

Figure 3.14: Picture of the perpendicular injection optics and the collection telescope.

3.4.3 Langmuir & emissive probes

Figure 3.15 shows a diagram of the sweeping circuit used for both the Langmuir and emissive probes. The bias voltage is provided by a 1 kHz triangle wave function generator in series with a Kepco BOP 200-1 power amplifier providing up to $\pm$ 200 V. The output of the Kepco is applied to the probe tip via a 10 Ω current sensing resistor. The current across the resistor is measured with an AD629 difference amplifier. For Langmuir probe use an rf choke [81] is held in series with the probe tip. The bias of the probe tip is measured with a 10-to-1 voltage divider and an IN114 instrumentation amplifier. The outputs of both operational amplifiers are measured by an oscilloscope. 64 traces are averaged and then recorded by the oscilloscope. The entire probe circuit, except for the probe tip, is encased in a grounded aluminum case so as to shield it from rf noise.

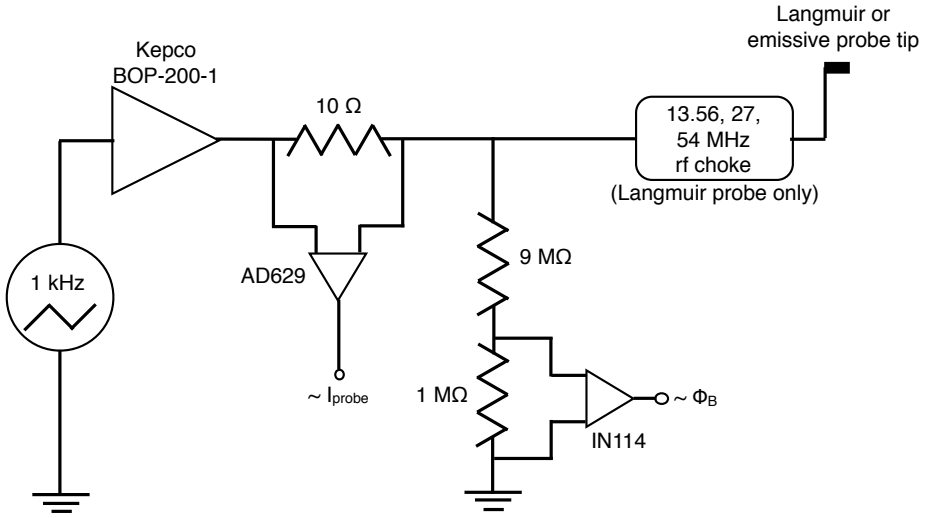

Figure 3.15: A diagram of the emissive and Langmuir probe electronics.

For Langmuir probe measurements the probe tip consists of a 0.6 mm diameter tungsten wire 0.5 cm long. For emissive probe measurements the probe tip is a 0.1 mm diameter thoriated tungsten wire. The thoriated tungsten has a lower work function than pure tungsten, increasing its electron emissivity for a given wire temperature. The emissive probe wire is heated to emission via Joule heating from collection of electron current from the plasma. The probe sweep range is set such that the probe collects enough electron current to heat the probe to emission. As the probe cooling time is much longer than the sweep period, the probe temperature remains constant across the range of the sweep and the probe emits a constant value of emission current below the plasma potential [93].

Both probes are constructed by spot welding the respective tip to a gold-plated nickel wire, which itself is soldered to the wire fed to the BNC output of the probe shaft. The probe tip is held by an alumina collar, which also acts to shield the gold-plated nickel wire from the plasma. The alumina collar is held by a 0.6 cm diameter stainless steel tube, which has a 90^o bend at the end. The tube is fed through the vacuum slip joint, to allow for linear and rotational translation. Because the shaft has a 90^o bend at the end, rotation allows for diagnosis of different radial positions. The part of the shaft exposed to

the plasma is covered by a 0.6 cm ID quartz tube, shielding the plasma from the grounded loss area of the shaft wall.

3.4.4 Experimental setup for $\psi = 0^o$ experiment

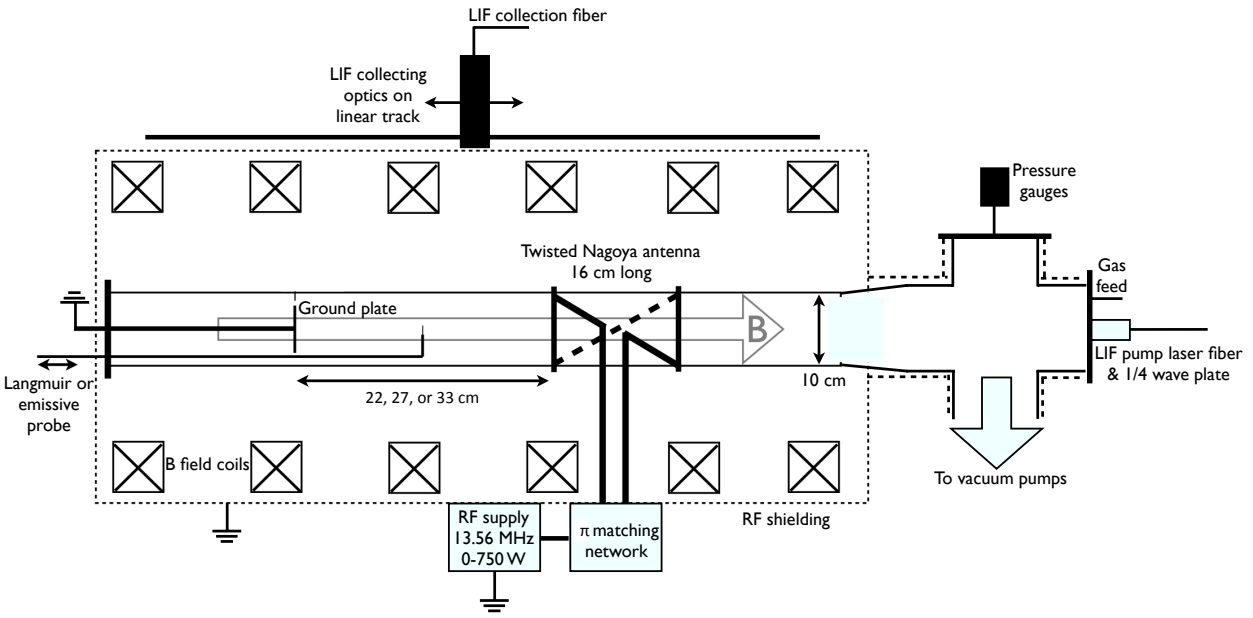

Figure 3.16: Diagram of the experimental apparatus for the $\psi = 0^o$ experiment.

A diagram of the experimental setup for the $\psi = 0^o$ experiment is given in figure 3.16. For this experiment an axial magnetic field of 900 $\pm$ 25 G is applied. the helicon antenna is wrapped around the Pyrex tube whose right edge is one antenna length away from the flange joining the tube and the cross-tee. The antenna position is not adjustable. For this experiment 500 W of rf power is coupled to the plasma at 13.56 MHz via a π matching network. 3 to 4 mTorr of argon gas is injected on the right side of the system. On the left side of the system a 6.3 cm diameter grounded stainless steel plate is placed either 22, 27, or 33 cm downstream from the helicon antenna.

The rf compensated Langmuir probe or uncompensated emissive probe is inserted through the left side of the system in order to measure electron temperature and ion density,

or local plasma potential respectively. The ion density is calculated from the ion saturation current from the Langmuir probe. The emissive probe is swept over $\approx$ 200 V, and changes in the upper bound of the sweep voltage by 5 to 10 V yielded strong changes in probe temperature and thus electron emission level. The "limit of zero emission" method [84] is used to measure plasma potential, as only this method is reliable in the presence of strong electron beams, which can exist in helicon plasmas and near double layers. The diode laser beam is injection from the flange on the right side of figure 3.16 via a fiber coupler, linear polarizer and quarter wave plate.

3.4.5 Experimental setup for $\psi = 16^o \rightarrow 60^o$ experiment

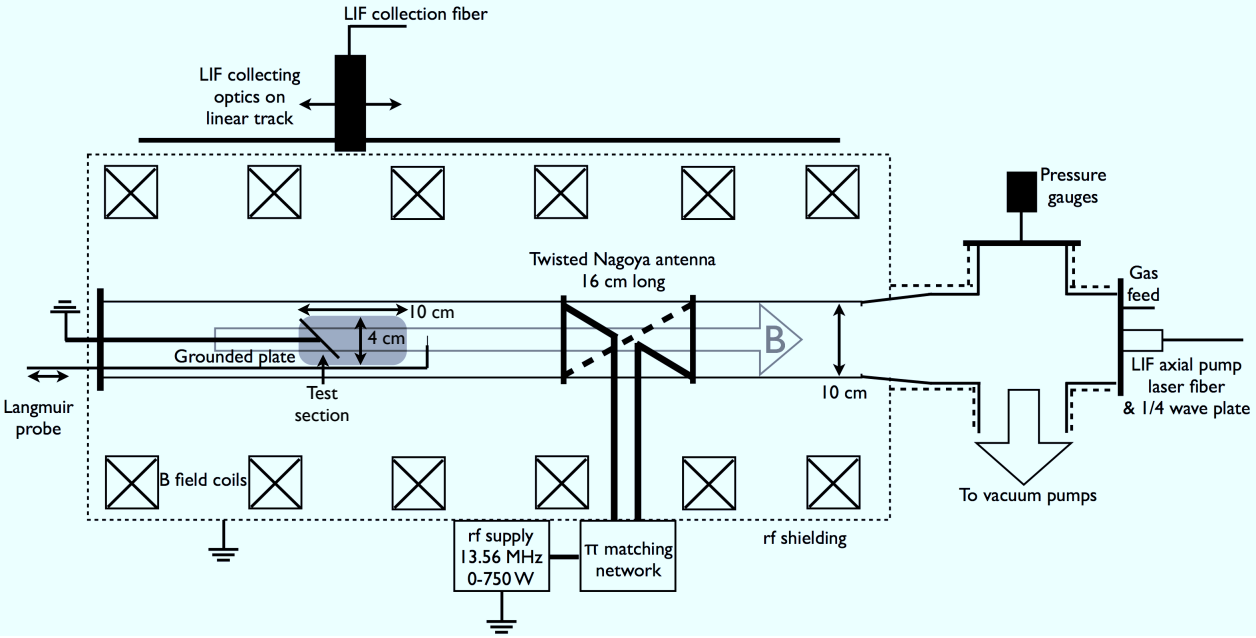

Figure 3.17: Diagram of the experimental apparatus for the $\psi = 16^o \rightarrow 60^o$ experiment. The shaded region shows approximately where measurements were made for this experiment. The angle of the grounded plate is shown in the wrong plane and is simply for demonstration purposes. The perpendicular pump laser beam goes into the page in this projection.

The experimental setup for the $\psi = 16^o \rightarrow 60^o$ is the same as the previous setup except for a few notable features. Figure 3.17 shows a diagram of the experimental setup. The grounded plate is fixed at 27 cm from the edge of the antenna and held at $16^o, 30^o, 45^o$, or 60^o to the background magnetic field. The magnetic field is set at 1 ± 0.03 kG. rf power is varied between 450 and 750 W to achieve similar ($T_e = 2.5 \rightarrow 5$ eV, $n_i \approx 1 \times 10^{12} cm^{-3}$) plasma parameters and strong LIF signal for each run. Measurements are performed at 1, 3 and 6.5 mTorr and are taken in the shaded region seen in figure 3.17. The probe is inserted and the measurements taken in this experiment in the same manner as the $\psi = 0^o$ experiment. The axial pump LIF laser beam is injected from the same location as the previous experiment. The $\psi = 16^o \rightarrow 60^o$ experiment also has perpendicular pump laser beam injection, not shown in figure 3.17, but seen in figure 3.14. A diagram of the parallel and perpendicular LIF scheme is shown in figure 3.18. The collection optic is mounted transverse to both the parallel and perpendicular pump lasers (laser beams visible in figure 3.18 but not figure 3.17) and can be moved both axially and radially. The collection optic's focal spot has a diameter of 0.4 cm, setting the lower limit for the LIF spatial resolution. At any given time, only the axial or perpendicular pump laser is injected so as to separately diagnose ion flow parallel and perpendicular to the magnetic field.

3.5 System parameterization

The sum of all parts just described is referred to as "MARIA", which stands for the **M**agnetized **A**nisot**R**opic **I**on-distribution **A**pparatus. MARIA is capable of generating plasmas in the capacitive, inductive and helicon modes. The mode changes are visually correlated with jumps in discharge brightness. A representative plasma density scan as a function of rf power at 500 G and axial magnetic field strength at 350 W is given in figure 3.19.

Plasma density jumps are apparent at 100 W and 250 W, suggesting the boundaries be-

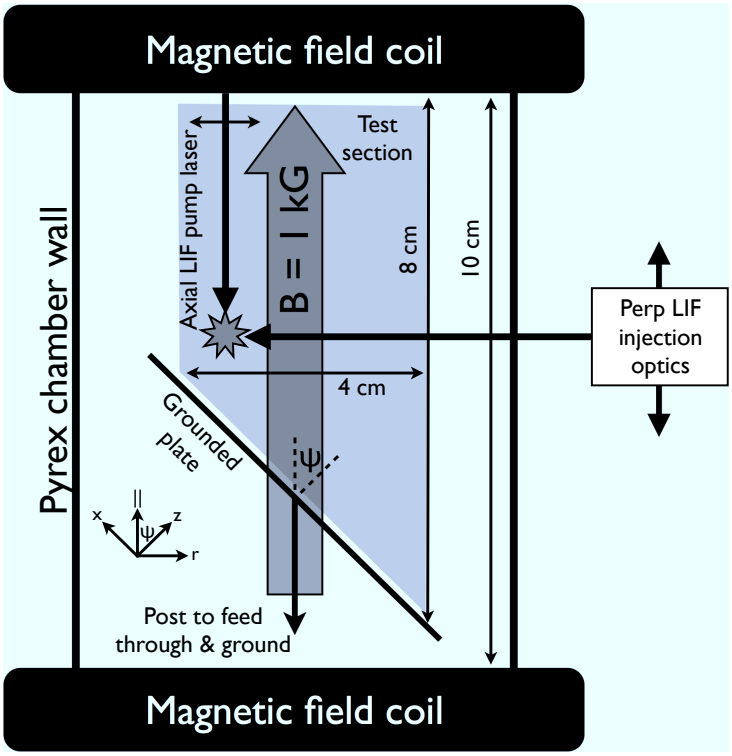

Figure 3.18: Cross section of the experimental test section for $\psi = 16^o \rightarrow 60^o$ experiment with parallel and perpendicular pump lasers shown. The shaded region shows the location where LIF measurements are made. The collection optics are oriented perpendicular to the page in this projection ('y' axis, not shown).

tween the different discharge regimes. The bottom panel of figure 3.19 shows that at 300 W, the plasma density increases linearly with increasing magnetic field strength, suggesting that this final discharge regime is a helicon mode. Given the range of neutral pressure, magnetic field strength, and rf power, a wide range of characteristic plasma lengths and frequencies can be obtained. These ranges are summarized in table 3.1. Figure 3.20 shows two representative IVDF measurements and their fits to Gaussian functions, which are used to calculate the ion temperatures and drift velocities.

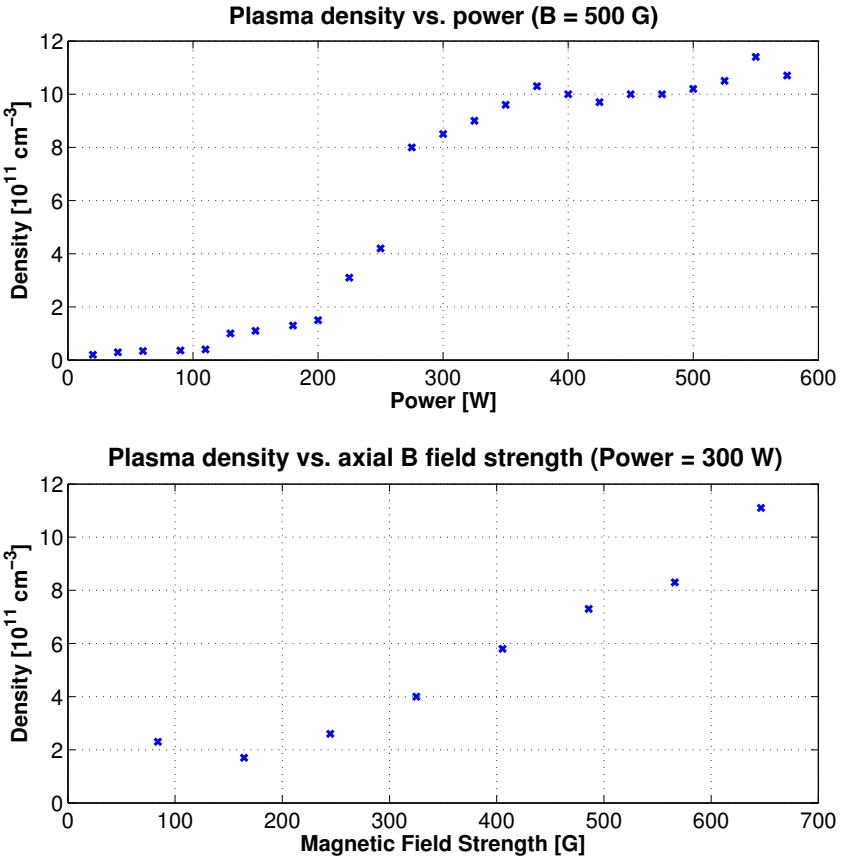

Figure 3.19: Plasma density on axis as a function (a) rf power and (b) magnetic field strength.

Parameter	**Range**
p_n	$0.5 \rightarrow 10$ mTorr
λ	$0.2 \rightarrow 4$ cm
n_o	$5 \times 10^8 \rightarrow 5 \times 10^{12}\, cm^{-3}$
T_e	$2 \rightarrow 7$ eV
T_i	$0.1 \rightarrow 0.6$ eV
λ_D	$0.001 \rightarrow 0.06$ cm
ρ_i	$0.5 \rightarrow 1$ cm
ρ_e	$5 \times 10^{-4} \rightarrow 1 \times 10^{-3}$ cm
f_{pi}	~ 10 MHz
f_{pe}	~ 3 GHz
f_{ci}	$20 \rightarrow 40$ kHz
f_{ce}	$1.4 \rightarrow 2.8$ GHz

Table 3.1: Plasma parameters capable of being produced by MARIA

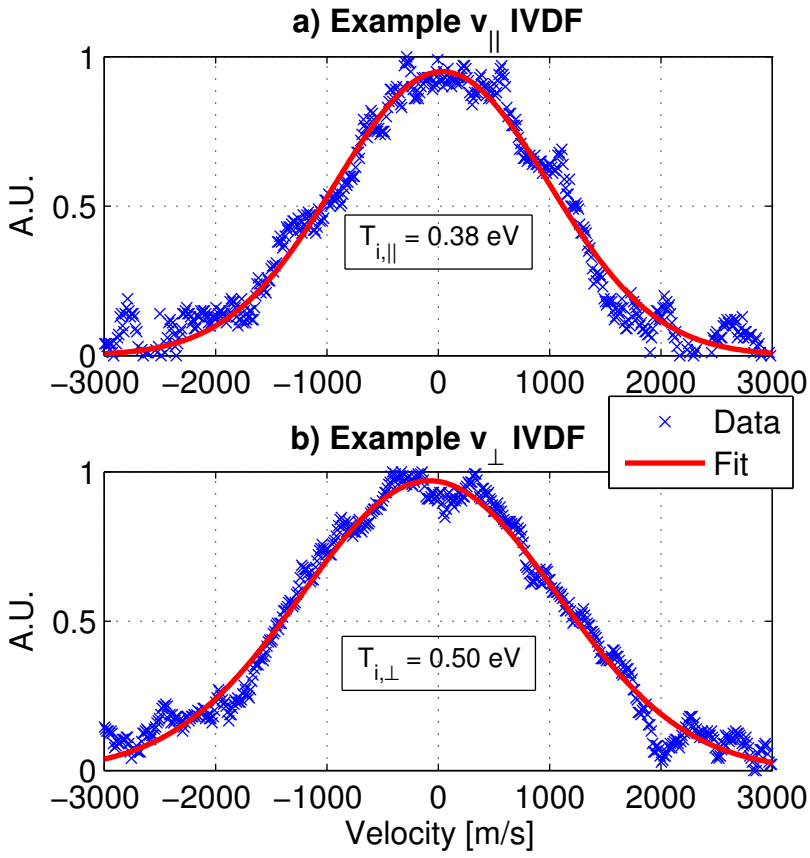

Figure 3.20: Representative measured (a) parallel and (b) perpendicular ion velocity distribution functions (IVDFs) for a 3 mTorr plasma with $\psi = 16^o$. Measurements are taken on axis 10 cm from the grounded plate. $v_{||}$ is the ion drift velocity parallel to the magnetic field, and $v_{\perp}$ is the velocity perpendicular to the field (in the 'r' direction shown in figure 3.18).

Chapter 4

$\psi = 0^o$ Experiment

4.1 Probe & LIF measurements - The observation of double layer-like structures

For the first presheath measurements, a 6 cm diameter grounded plate was held on axis 27 cm from the edge of the rf antenna. Langmuir and emissive probe traces were taken between 0 and 4 cm from the axis radially and at many locations axially between the plate and the helicon antenna for a neutral pressure of 3 mTorr, magnetic field strength of 900 $\pm$ 25 G, and 500 W rf power. Langmuir probe traces taken between 0 and 2.5 cm radially and 15 to 20 cm from the grounded plate exhibited characteristics of both a hot and cold electron population. Two example traces are given in figure 4.1. In this figure, the natural log of the trace taken 9 cm from the grounded plate (the trace on the left) has a single region of constant slope over approximately three decades, indicating a single Maxwellian electron population (panel d). The trace taken 17 cm from the grounded plate (the right trace) consists of two regions of linear slope over at least a decade in electron current each. The hot electron temperature varies between 7 and 12 eV, whereas the cold electrons has a temperature of 2 to 3 eV. The traces in figure 4.1 have been artificially offset in voltage

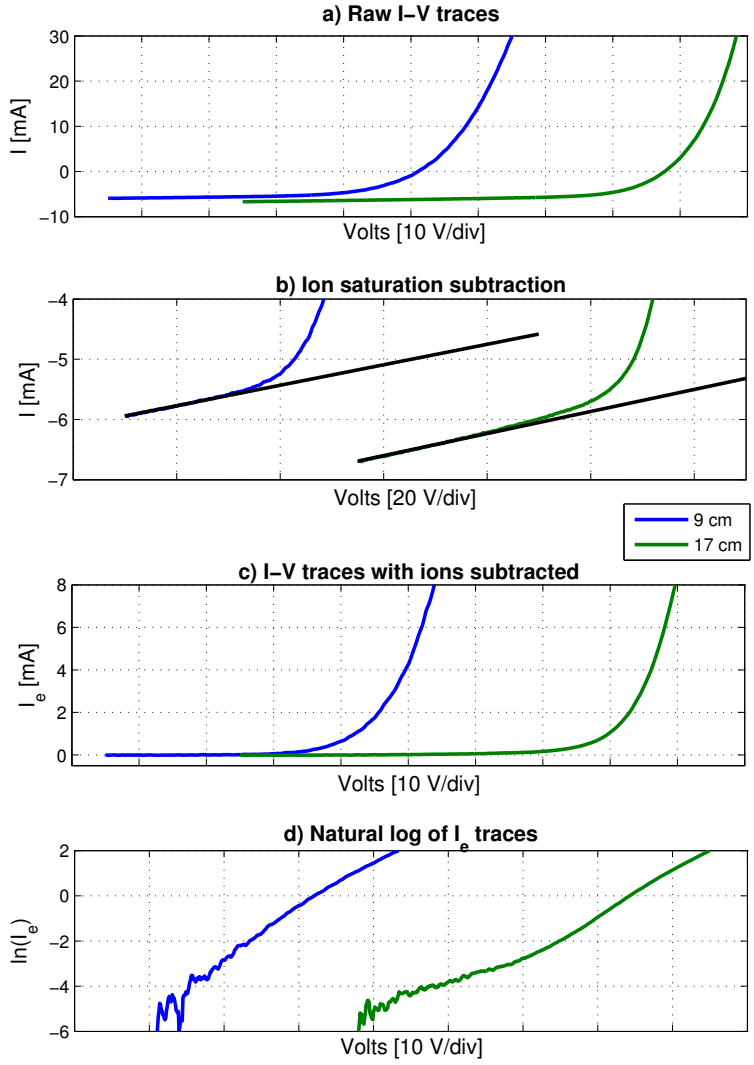

Figure 4.1: Example I-V traces taken on axis at two different locations relative to the location of the grounded plate. The traces are artificially offset in voltage for comparison purposes. (a) Raw traces. (b) Magnified view of ion saturation regions. Black lines are subtracted ion current assuming planar geometry. (c) Resulting electron current traces. (d) Natural log of electron current traces showing Maxwellian (9 cm) and bi-Maxwellian electron energy distributions (17 cm).

for comparison purposes.

The location and values of the hot electron temperatures is plotted in a contour map, alongside the plasma potential from the emissive probe traces, the ion density from the Langmuir probe traces, and the ion axial drift velocities from the LIF measurements in figure 4.2. In panel (a) of this figure a region of strong axial electric field is seen at

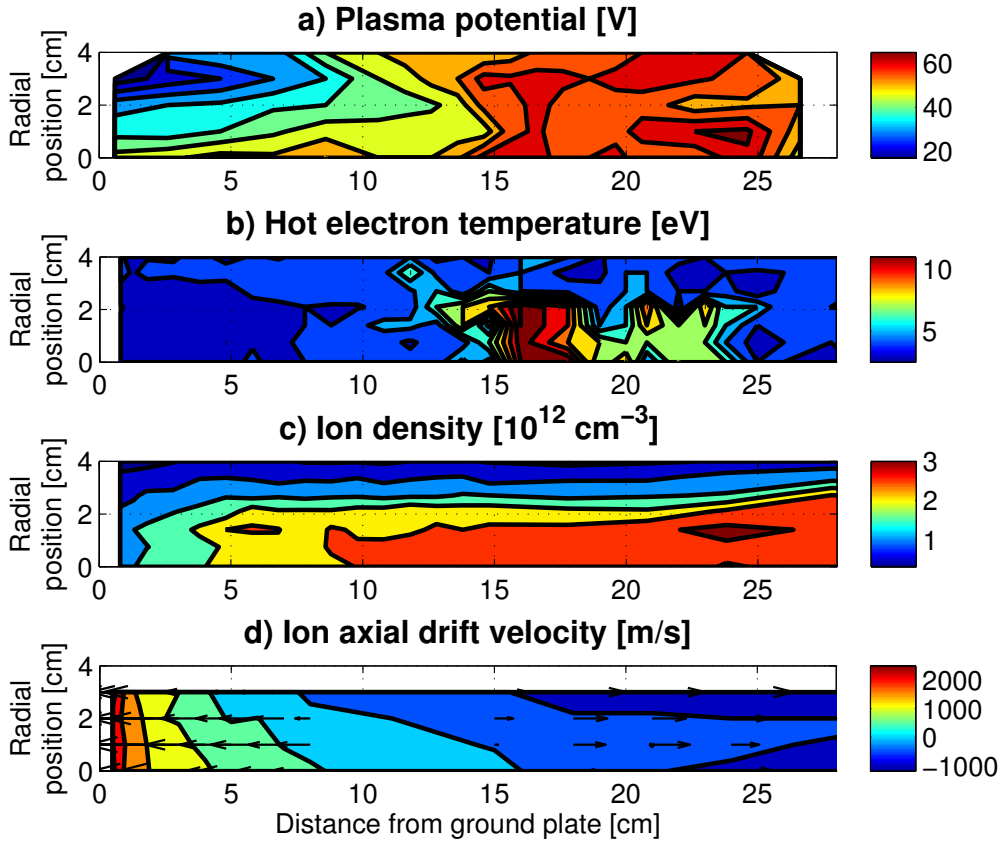

Figure 4.2: The plasma potential (a), hot electron temperature (b), ion density (c), and ion axial drift velocity (d) at different axial and radial positions in the plasma for a neutral pressure of 3 mTorr, magnetic field strength of 900 $\pm$ 25 G, and 500 W rf power. The grounded plate is located at 0 cm and the edge of the rf antenna is located at 27 cm (see figure 3.16).

approximately 15 cm from the grounded plate and exists radially between 0 and 2.5 cm. This potential step is dubbed the "double layer-like structure" as it exhibits a localized potential step of approximately 10 V, but it occurs over a few λ, rather than λ_D. In panel (b) it is observed that on the high potential side of the electric field a region of hot electrons exists. Everywhere else the electrons have a temperature of 3 to 4 eV. In panel (c) the ion density is plotted. Panel (d) of figure 4.2 shows the ion axial drift velocity at different radial and axial positions. The superimposed arrows show the direction and magnitude of the flow velocity. The ions change flow direction approximately 15 cm from the grounded plate, indicating the presence of a potential peak in that region. An appropriately located potential well could also draw ions towards the antenna, but without a peak somewhere upstream of the grounded plate an ion flow stagnation point would not exist. The absence of data indicated by the lack of arrows between 8 and 15 cm from the grounded plate is due the the presence of a pancake coil, which prevented optical access to the system at these locations. The data here are interpolated between the data points at 8 and 15 cm, and as such, inaccuracies may be significant in this region.

The strong axial electric field is positioned adjacent to the region of hot electrons both radially and axially. The hot electrons are all within one antenna length (16 cm) from the edge of the antenna (z = 27 cm). Electron temperature peaks in the near field of the rf antenna in helicon sources are well documented [55, 56, 94] and the observation of similar phenomena here suggests that the double layer-like structure's location may be determined by localized electron heating. However, another spatial scale exists in our system - the presheath of the grounded plate. As discussed in chapter 2, presheaths are known to scale with the ion-neutral collision length in low temperature systems.

To investigate the effects of the presheath axial scans of potential (figure 4.3), electron temperature (figure 4.4), and ion density (figure 4.5) were performed normal to the grounded plate for a variety of neutral pressures. All neutral pressures exhibit similar

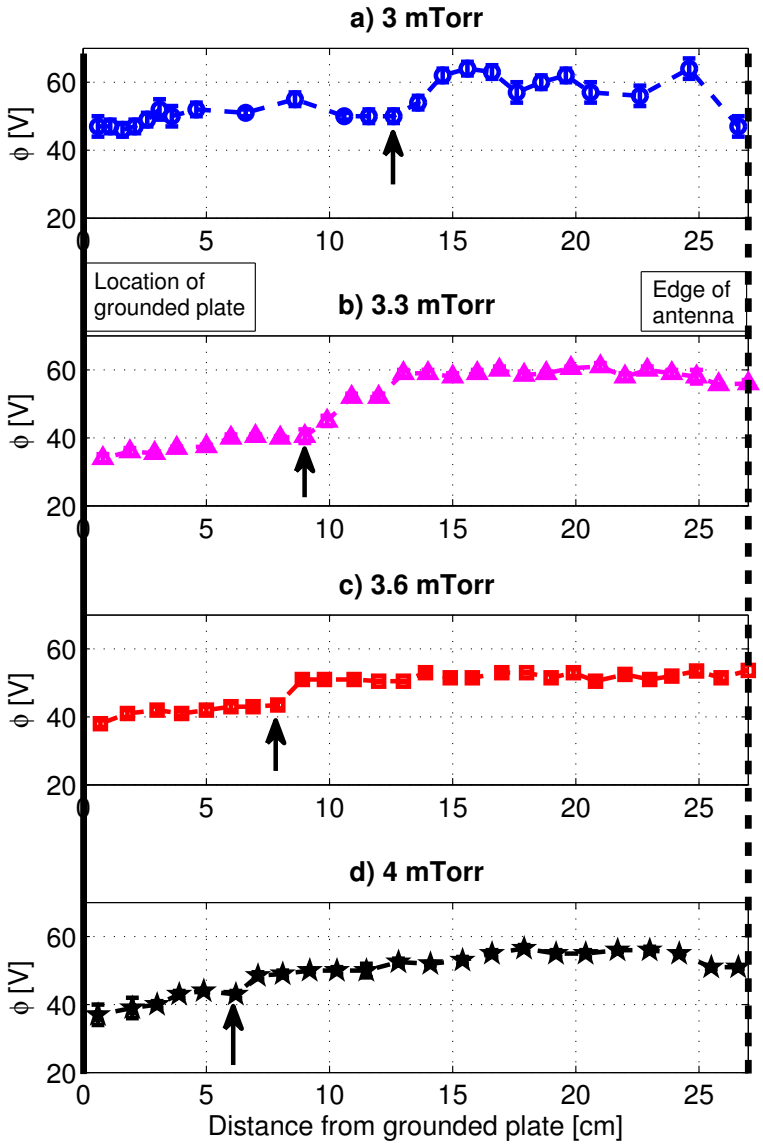

Figure 4.3: Scans of potential (ϕ) normal to the grounded plate on the system axis for neutral pressures of (a) 3, (b) 3.3, (c) 3.6, and (d) 4 mTorr of argon. Upward arrows indicate location of the edge of the double layer-like structure. The vertical solid black line at 0 cm indicates the location of the grounded plate, and the vertical dashed line at 26 cm shows the location of the leading edge of the rf antenna.

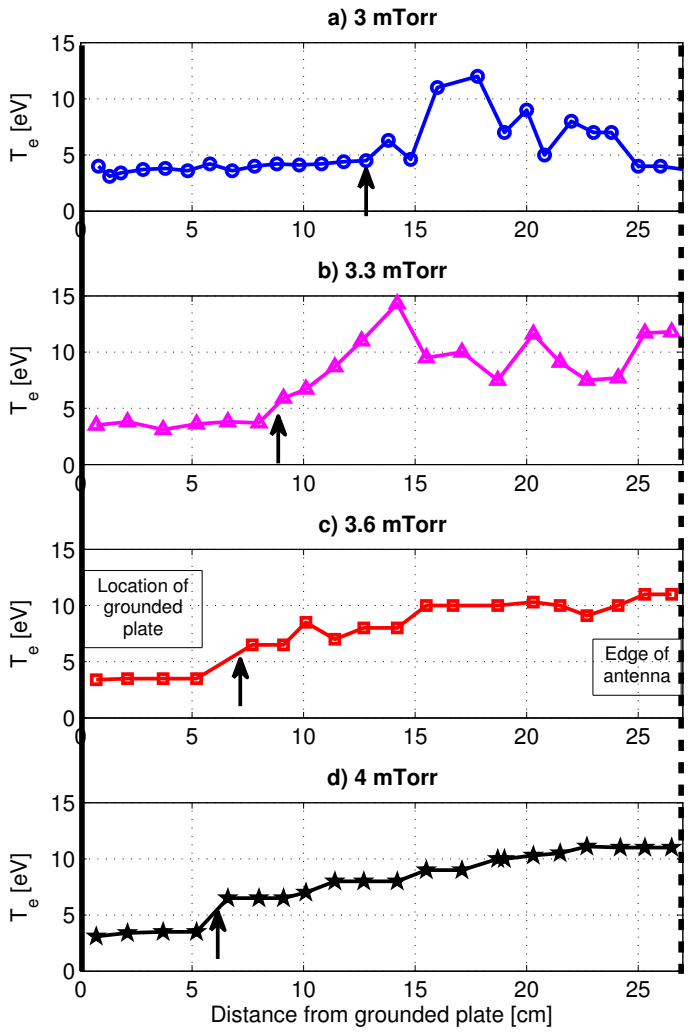

Figure 4.4: Scans of electron temperature (T_e) normal to the grounded plate on the system axis for neutral pressures of (a) 3, (b) 3.3, (c) 3.6, and (d) 4 mTorr of argon. Upward arrows indicate location of the edge of the double layer-like structure from figure 4.3. The vertical solid black line at 0 cm indicates the location of the grounded plate, and the vertical dashed line at 26 cm shows the location of the leading edge of the rf antenna. The uncertainties in the data are equal to the sizes of the individual data markers.

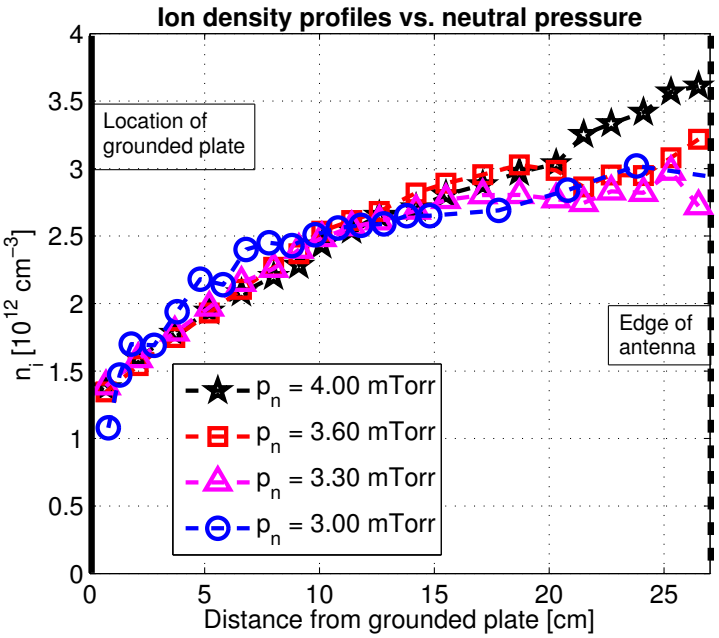

Figure 4.5: Scans of ion density (n_i) normal to the grounded plate on the system axis for neutral pressures of 3 (blue circles), 3.3 (pink triangles), 3.6 (red squares), and 4 (black stars) mTorr of argon. The vertical solid black line at 0 cm indicates the location of the grounded plate, and the vertical dashed line shows at 26 cm the location of the leading edge of the rf antenna. The uncertainties in the data are smaller than the sizes of the individual data markers.

phenomena - a potential step of a few volts adjacent to a step in electron temperature of a few eV. In figure 4.4, to the right of the upward arrows, the temperature of the hotter of the two populations is plotted. The cold population in those regions have the same temperature as the single population observed to the left of the upward arrows (from 3 - 4 eV for all neutral pressures). Figure 4.5 shows the ion densities measured from the Langmuir probe for these experiments. For all neutral pressures in this discharge regime, the ion densities exhibit a monotonic decay from the antenna to the grounded plate. No major localized peaks in density are measured anywhere.

The measured height of the potential step across the double layer-like structure ($\Delta\phi_{meas}$) is sufficient to equalize thermal electron fluxes everywhere in the system, such that no net charge builds up in time at any given location. The fluxes of particles through the plane perpendicular to the magnetic field at a given axial position is given by the sum of particle fluxes going from right to left minus the sum of particle fluxes going from left to right at that location. For electrons we have

$$\Gamma_e^+(z) - \Gamma_e^-(z) = 0 \tag{4.1}$$

where $\Gamma_e^{\pm}(z)$ is the electron flux in the axial (z) direction to the right (+) and left (-) directions. For a Maxwellian population of particles the random thermal fluxes of particles in a given direction is $\Gamma \sim n\bar{v}$ where n is the particle density and $\bar{v}$ is the average particle speed. In order to predict the value of $\Delta\phi$ needed to equalize thermal particle fluxes, we can evaluate equation 4.1 assuming electron flux conservation across the double layer-like structure ($\Gamma_e^-(z) \approx \Gamma_e^-(z_h)$, where z_h is the z position of the high potential side of the double layer-like structure). This is justified as $\tau_{DL}\nu_{iz} \ll 1$, where τ_{DL} is an electron transit time across the double layer, and ν_{iz} is the ionization frequency. Evaluating equation 4.1 on the low potential side of the double layer-like structures in figure 4.3 (indicated by the upward arrows) we have

$$n_e(z)\overline{v(z)} = n_c(z)\overline{v_c} + n_h(z)\overline{v_h} \tag{4.2}$$

where $n_e(z)$ is the electron density on the low potential side of the double layer-like structure, $n_c(z)$ is the cold electron density from the high potential side of the structure, $n_h(z)$ is the hot electron density at that location, $\overline{v_c}$ is the average cold electron speed, and $\overline{v_h}$ is the average hot electron speed. The hot and cold electron densities are given by the Boltzmann relation for electrons along the magnetic field such that

$$n_{c,h}(z) = n_{c,h}(z_h)exp[e\Delta\phi/T_{c,h}] \tag{4.3}$$

where $\Delta\phi$ is the potential drop across the double layer-like structure (negative going from right to left) and $T_{c,h}$ is the cold and hot electron temperature respectively. Plugging this into equation 4.2 and using the definition of average particle velocity in a Maxwellian distribution for $\bar{v}$ we have

$$n_e(z)\sqrt{T_e} = n_c(z_h)exp[e\Delta\phi/T_c]\sqrt{T_c} + n_n(z_h)exp[e\Delta\phi/T_h]\sqrt{T_h}. \tag{4.4}$$

To predict the value of the potential drop across the double layer-like structure ($\Delta\phi_{pred}$) measured values for n and T are plugged into equation 4.4, and $\Delta\phi$ is solved for. Data for temperature are given in figure 4.4. For n_e, quasineutralty is assumed on the low potential side of the double layer-like structure and hence n_e is taken from data in figure 4.5. On the high potential side of the structure, quasineutrality is still assumed, however because two electron populations exist the relation $n_i(z_h) \approx n_c(z_h) + n_h(z_h)$ (where n_i is the ion density given in figure 4.5) must hold. Estimating the contribution of n_c and n_h to the total electron density in a plasma with two Maxwellian electron populations is performed by analysis of the Langmuir probe traces as described in chapter 3. Using these data, it follows that in equation 4.4 the cold electron fluxes from the high potential side are much less than the hot electron fluxes such that

$$n_e(z)\sqrt{T_e} \approx n_h(z_h)exp[e\Delta\phi/T_h]\sqrt{T_h}. \tag{4.5}$$

From this equation the predicted values of the double layer potential drops are

$$\Delta\phi_{pred} = \frac{T_h}{e} ln\left[\frac{n_e(z)}{n_h(z_h)}\sqrt{\frac{T_c}{T_h}}\right]. \tag{4.6}$$

The predicted value is compared to the measured value of $\Delta\phi$ in figure 4.6. The uncertainty in $\Delta\phi_{pred}$ shown in the figure is largely due to uncertainty in the measured values of $n_h(z_h)$. $n_e(z)/n_h(z_h)$ is given in table 4.1. Within this uncertainty, the measured value of the double layer potential drop follows the prediction using the measured values of n and T for all the neutral pressures investigated. This supports the idea that the double layer-like structure exists to maintain charge balance everywhere in the system.

p_n [mTorr]	T_c [eV]	T_h [eV]	$n_h(z_h)/n_e(z)$
3	4.1 ± 0.02	12 ± 0.05	0.25 ± 0.05
3.3	4.2 ± 0.02	14 ± 0.05	0.13 ± 0.07
3.6	3.7 ± 0.02	7 ± 0.05	0.2 ± 0.05
4	3.3 ± 0.02	7 ± 0.05	0.15 ± 0.07

Table 4.1: Table of hot and cold electron temperatures, and ratios of hot to bulk plasma densities for data in figure 4.6.

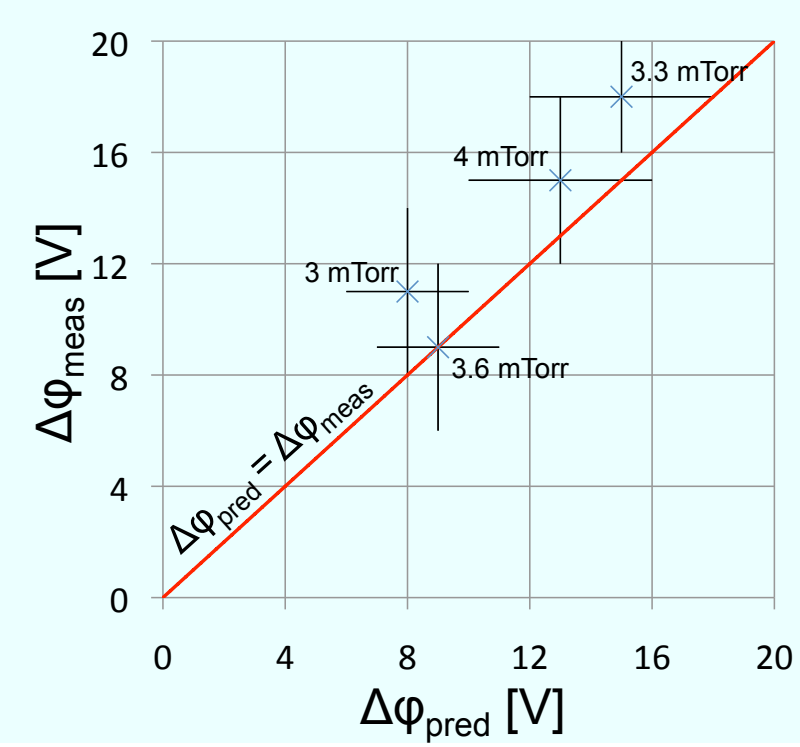

Figure 4.6: Comparison of $\Delta\phi_{pred}$ vs $\Delta\phi_{meas}$ from data provided in figures 4.3-4.5.

As observed in figure 4.3, the double layer-like structure's position, as indicated by the black arrows in figure 4.3, depends on the neutral pressure. The neutral pressure was only varied between 3 and 4 mTorr as above and below these pressures, for fixed forward rf

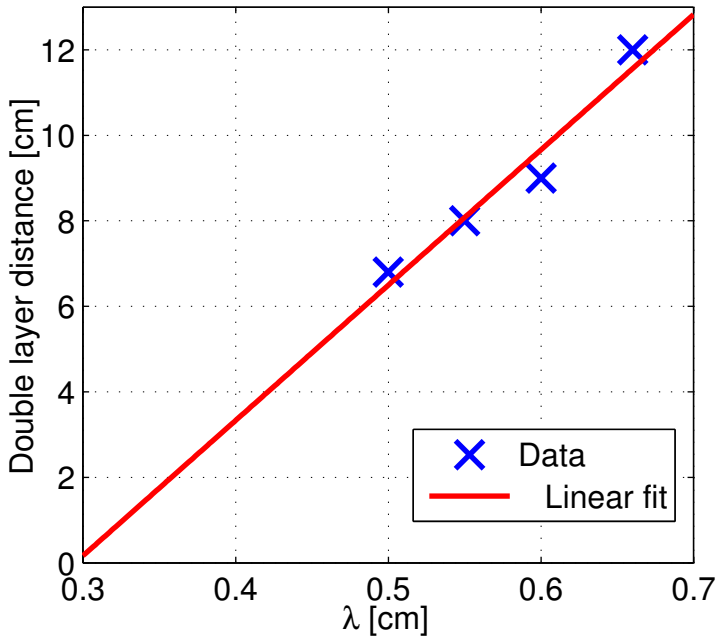

Figure 4.7: Double layer-like structure's distance from grounded plate versus λ. Grounded plate located 27 cm from leading edge of rf antenna. The uncertainties in the data are equal to the sizes of the individual data markers.

power and magnetic field strength, the discharge changed modes (indicated by a change in brightness and density and electron temperature profiles). Changing the neutral density changes the ion-neutral collision length, λ. This length is known to be the scale length relevant to presheath formation [3, 4]. Figure 4.7 shows the double layer-like structure's distance from the grounded plate versus λ. Just like the length of a presheath, the measured distance increases linearly with λ.

Figure 4.8 shows the ion drift velocities from the edge of the double layer-like structure to the grounded plate for all neutral pressures. Upstream from the double layer-like structures the ions had, within their respective uncertainties, zero drift velocity. The 3 and 3.3 mTorr data are taken up to the magnetic field coil, as measurements underneath were not possible due to lack of optical access. The double layer like structures occurred un-

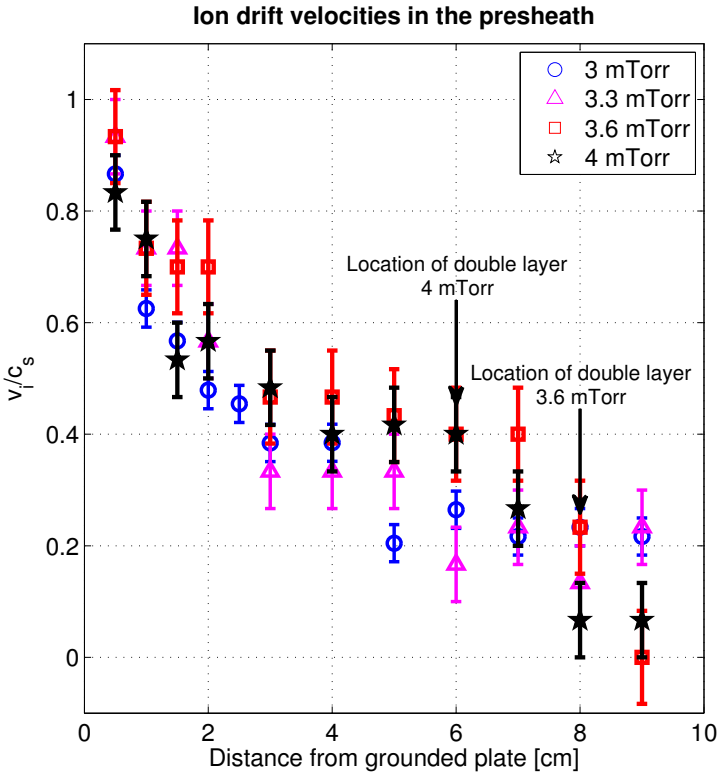

Figure 4.8: Ion drift velocities (v_i) normalized to the sound speed ($c_s = \sqrt{(T_e + T_i)/M_i}$) in the presheath of the grounded plate for different neutral pressures. The black arrows correspond to the locations of the edges of the double layer-like structures for 3.6 and 4 mTorr, as seen in figure 4.3 panels (c) and (d).

derneath the coil for these pressures. The 3.6 and 4 mTorr data gain 0.4 times the sound speed across the double layer-like structure. To check the consistency of these data with Langmuir and emissive probe measurements the ion fluid equation

$$v_i \frac{\partial v_i}{\partial z} = \frac{e}{M_i}\overline{E_z} - \frac{T_i}{n_i M_i}\frac{\partial n_i}{\partial z} - \nu_c v_i \tag{4.7}$$

was solved numerically, where v_i is the ion drift velocity, $\overline{E_z}$ is the average electric field across the double layer-like structure, T_i is the ion temperature, and $\nu_c = n_n \sigma v$ is the collision frequency. n_n is the neutral gas density, v is the total three dimensional ion velocity,

and σ is the momentum transfer collision cross section from Phelps [96]. Using data for density and drift velocities, $\overline{E_z}$ is found to be $\approx$ 200 V/m, comparable to the 500 V/m measured by the emissive probe. Discrepancies between the estimated $\overline{E_z}$ and the measured values could be due to the fact that the probe's ceramic collar is comparable in size to the width of the double layer structure, potentially perturbing it during measurement. Also, given the spatial resolution of the probe, determined by the size of the ceramic collar, the spatial extent of the double layer-like structure may be smaller than what is observed in the data for 3.6 and 4 mTorr in figure 4.3.

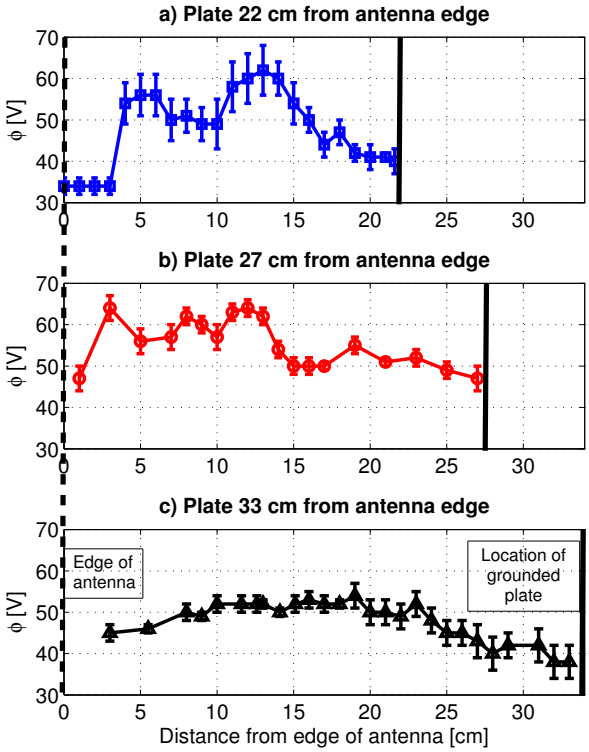

Figure 4.9: Axial potential scans for grounded plate positions of (a) 22, (b) 27, and (c) 33 cm from the rf antenna. The vertical solid black lines to the right indicate the location of the grounded plate, and the vertical dashed line shows the location of the leading edge of the rf antenna.

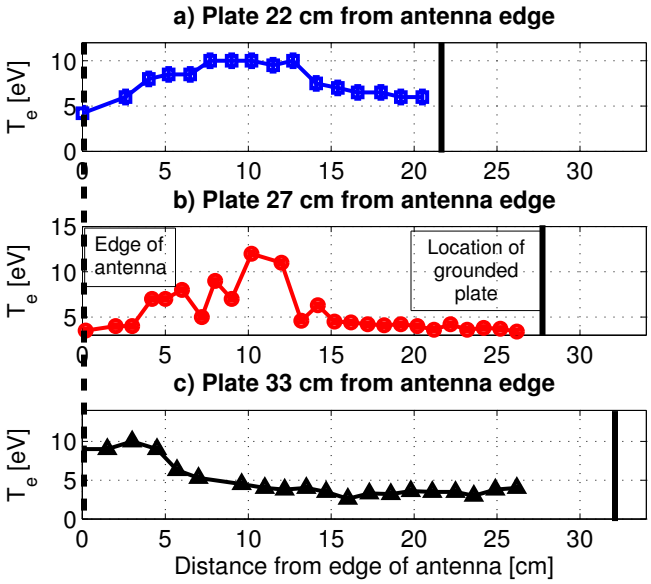

Figure 4.10: Axial electron temperature scans for grounded plate positions of (a) 22, (b) 27, and (c) 33 cm from the rf antenna. The vertical solid black lines to the right indicate the location of the grounded plate, and the vertical dashed line shows the location of the leading edge of the rf antenna.

After the neutral pressure scan, the grounded plate's position was moved relative to the rf antenna at a fixed neutral pressure of 3 mTorr, a magnetic field strength of 900 G and 500 W forward rf power. The plate is held at 22, 27, and 33 cm from the edge of the rf antenna. The 27 cm dataset is the same position the plate was in for the neutral pressure scan data presented in figures 4.3-4.5. Figures 4.9 and 4.10 show axial potential and electron temperature scans for these plate positions. Unlike figure 4.3, position is now measured relative to the rf antenna, not to the grounded plate. When the grounded plate is moved towards the antenna (panel (a) of figure 4.9), the double layer-like structure is still observed. A localized peak in electron temperature similar to those seen in figure 4.4 is also observed. When the grounded plate is moved away from the antenna relative to its original position (panel (c) of figure 4.9) no double layer-like structure is apparent.

Rather, the potential changes gradually along the axis of the system, with no localized

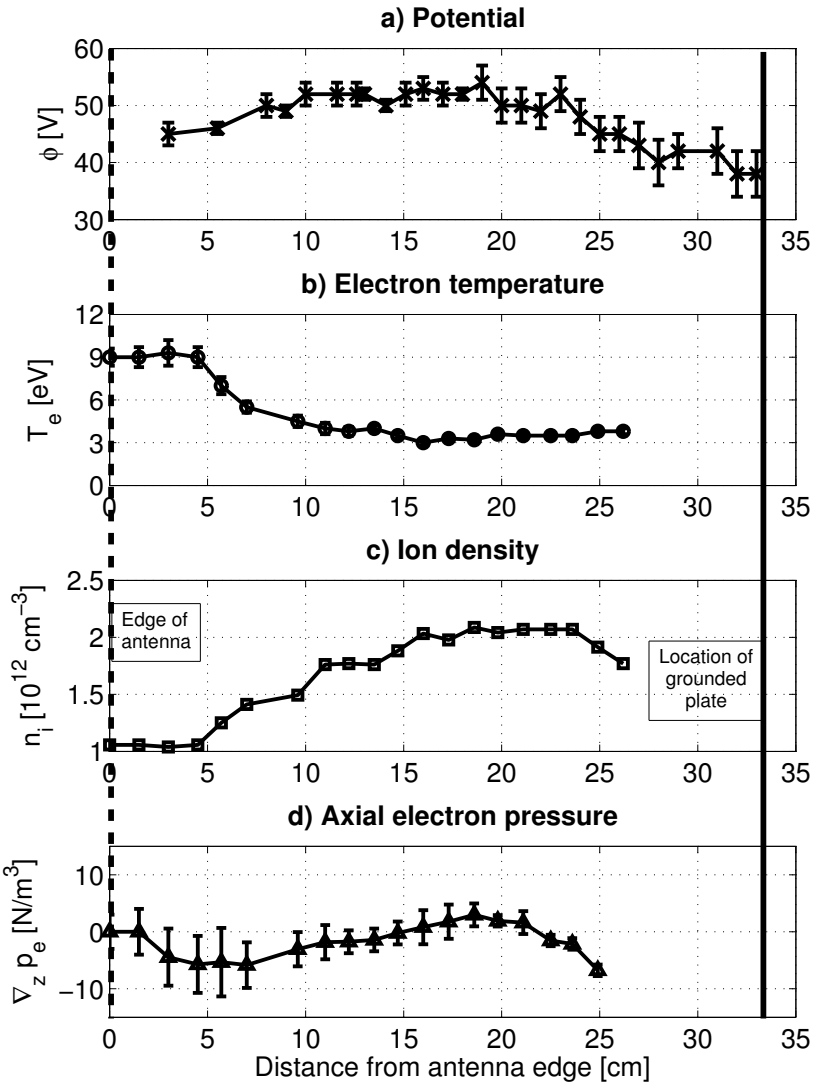

Figure 4.11: (a) Potential, (b) electron temperature, (c) ion density, and (d) calculated electron fluid pressure gradient for plate position 33 cm away from rf antenna. The vertical solid black lines to the right indicate the location of the grounded plate, and the vertical dashed line at 0 cm shows the location of the leading edge of the rf antenna.

regions of significant electric field. Figure 4.11 shows the electron temperature (panel (b)) and ion density profiles (panel (c)) for this plate position. These profiles exhibit different behavior than those where the double layer-like structure existed. Figure 4.11b shows a localized region of relatively hot electrons. For these data only one electron population is observed. No confining potential structures are observed. As the electron temperature decays moving away from the antenna, the ion density increases in the same distance. Figure 4.11d shows the thermal axial electron pressure gradient using the data in panels (a)-(c). The thermal pressure gradient is given by $\nabla_z p_e = \frac{\partial}{\partial z}(n_e T_e)$. Figure 4.11d shows that within the uncertainty, the gradient of the axial electron pressure is zero everywhere measured in the system. As such, no electric fields are necessary to maintain this as the increase in density in concert with the decrease in electron temperature keeps the gradient of the thermal axial electron pressure zero everywhere. This is the same discharge regime reported by Chen et al. [55, 56, 94].

4.2 Ion fluid model for $\psi = 0^o$ measurements

To further investigate this phenomenon, and to validate measurements taken in the presheath, the potential and ion drift velocity data in this region were fit to a one-dimensional ion fluid model, which takes into account ion pressure, collisional friction with neutrals, and ionization. The model is used to predict the ion velocities and plasma potential in the presheath as a function of the measured electron temperature, neutral and ion densities.

In deriving a one dimensional fluid model for ion flow in the presheath of the grounded plate, several considerations are necessary that are often overlooked elsewhere. First, ionization is significant in the system as the ionization frequency is comparable to the ion-neutral charge exchange collision frequency ($\nu_{iz} \sim \nu_c$). Ion pressure is also included in the fluid model. While the ion temperature is still much less than the electron temperature ($T_i \approx 0.1$ eV, $T_e \approx 3$ - 4 eV), the ion thermal speed ($v_{Ti} = \sqrt{T_i/M_i}$) is a significant frac-

tion of the Bohm speed, u_B ($\sqrt{T_i/T_e} \approx 0.2$). Finally ion pressure is assumed to follow the ideal gas law ($p_i = n_i T_i$), as LIF measurements in the presheath show a Maxwellian IVDF. Given these consideration, as with Riemann [3] and Helander et al. [95] the following equations are considered:

$$\frac{\partial}{\partial z}(n_i v_i) = n_e \nu_{iz} \tag{4.8}$$

$$n_e = n_0 exp[e(\phi - \phi_0)/T_e] \tag{4.9}$$

$$M_i n_i v_i \frac{\partial v_i}{\partial z} = -e n_i \frac{\partial \phi}{\partial z} - \frac{\partial p_i}{\partial z} - M_i v_i n_i \nu_c \tag{4.10}$$

where $\nu_{iz} = n_n K$. v_i is the ion drift velocity, and $\nu_c = n_n \sigma v$. n_n is the background neutral density and as direct neutral density measurements are not possible in this experiment it is a fitting parameter. K is the ionization rate constant. For electron temperatures up to 7 eV, it has been fit by Gudmundsson (as referenced by Lieberman [30]) to be

$$K[m^3/s] = 2.34 \times 10^{-14} T_e[eV]^{0.59} exp(-17.44/T_e[eV]). \tag{4.11}$$

σ is the momentum transfer collision cross section. v is the total ion velocity including gyro motions. As discussed previously, values for σ are taken from Phelps [96]. ϕ_0 is the measured reference potential taken at the same location the bulk plasma density in the presheath (n_0) is measured. Finally, quasineutrality ($n_i \approx n_e$) is assumed throughout the presheath. Using this, the ideal gas law and equations 5.1 - 5.2 the following coupled differential equations are obtained:

$$\frac{\partial \eta}{\partial z} = \frac{\nu_{iz} + \nu_c}{v_i - v_{Ti}^2/v_i - u_B^2/v_i} \tag{4.12}$$

$$\frac{\partial v_i}{\partial z} = \frac{\nu_{iz}(u_B^2/v_i^2 + v_{Ti}^2/v_i^2) + \nu_c}{u_B^2/v_i^2 + v_{Ti}^2/v_i^2 - 1} \tag{4.13}$$

where $\eta = e\phi/T_e$ and $u_B = \sqrt{T_e/M_i}$. From the denominators of equations 4.12 and 4.13, the fluid model approaches a singularity as $v_i \rightarrow c_s = \sqrt{u_B^2 + v_{Ti}^2}$. This has been used by Riemann [3, 29] to determine the location of the sheath-presheath transition. The

singularity occurs as the quasineutrality condition breaks down. As such equations 4.12 and 4.13 are integrated numerically from the measured location where $v_i = u_B$, outward. Starting from experimental values where the presheath begins and the double layer ends and integrating inwards yields the same results, except the integration must be aborted as the singularity is approached. The results are integrated using experimental values of n_i, T_i, T_e and then fitted to experimental data for potential and ion drift velocity in the presheath from figures 4.3 and 4.8, with the neutral density being the fitting parameter.

Figures 4.12 and 4.13 show the ion drift velocity and plasma potential data and fits for all neutral pressures. In order to achieve this fit an axial neutral density between $2.8 \rightarrow 4 \times 10^{13} cm^{-3}$ is necessary corresponding to a pressure of $\approx$ 1 mTorr. This indicates that there is significant neutral pumping on the axis of the system so that there is an axial neutral gradient between the measurement region in the experiment and the location of the pressure transducer [69, 70]. In either case, comparison of the data to the model shows that the double layer-like structure ends and the presheath begins where the ion velocity exiting the double layer matches the ion velocity necessary in the presheath at the given distance away from the grounded plate. For example, for the 3.6 mTorr dataset, the ion double layer exit velocity is 1300 $\pm$ 200 m/s. A free standing presheath for the plasma parameters in this system would accelerate ions to this velocity 6 cm from the grounded boundary, as predicted by the fluid model in figure 4.12c. As such, the double layer-like structure exists 6 cm away from the grounded plate. The double layer ion exit velocities for all neutral pressures are comparable (800 $\pm$ 100 m/s for 3 and 3.3 mTorr, and 1300 $\pm$ 200 m/s for 3.6 and 4 mTorr). Thus the double layer's distance from the grounded plate scales with the length of the presheath, which itself scales with λ, explaining the results in figure 4.7.

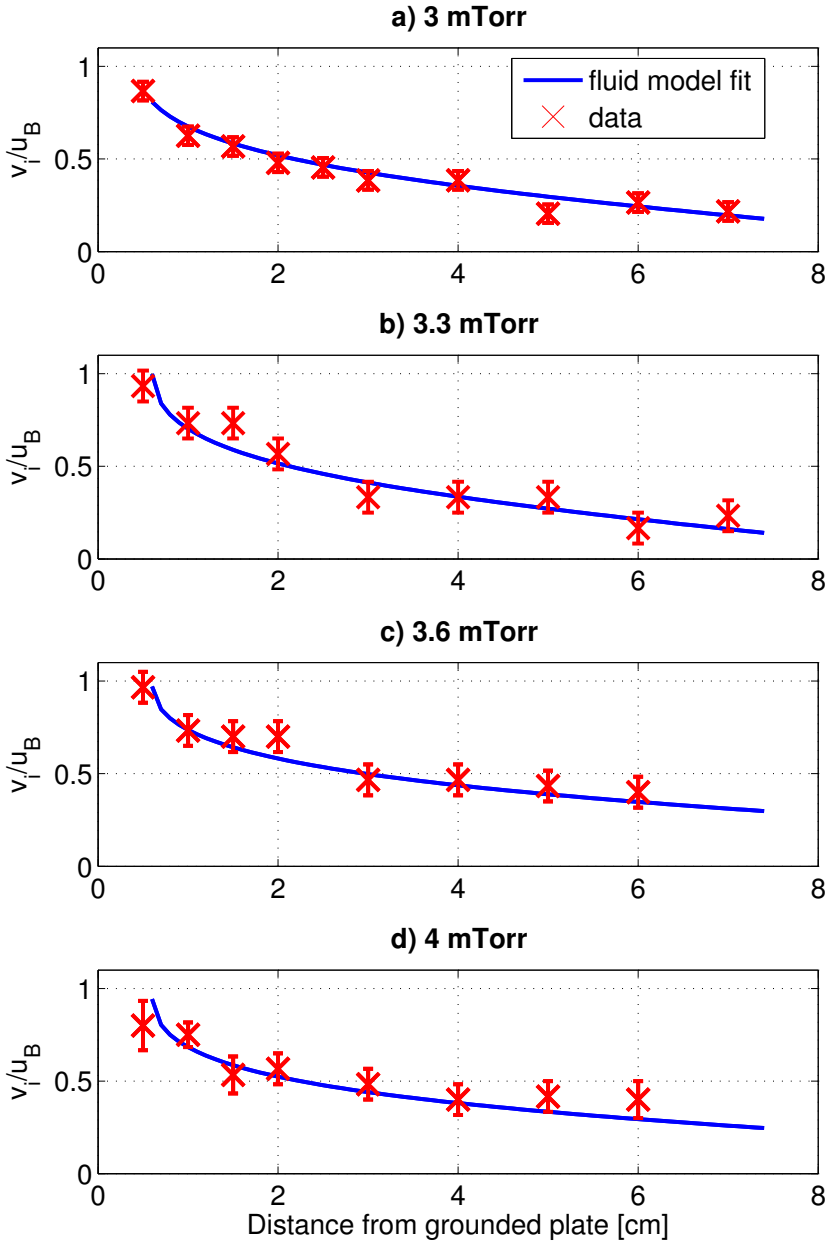

Figure 4.12: Fit of fluid model to ion drift velocity normalized to the Bohm speed ($u_B = \sqrt{T_e/M_i}$) for (a) 3 mTorr, (b) 3.3 mTorr, (c) 3.6 mTorr, and (d) 4 mTorr.

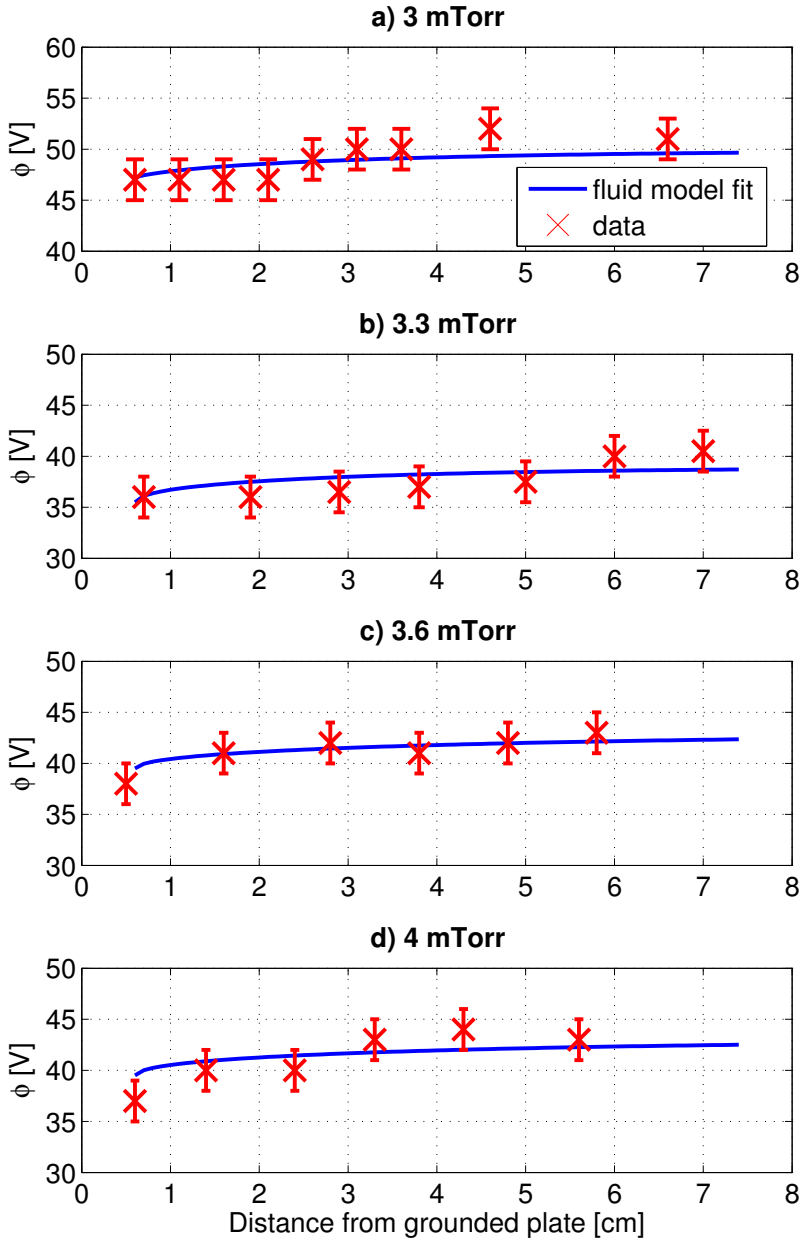

Figure 4.13: Fit of fluid model to plasma potential for (a) 3 mTorr, (b) 3.3 mTorr, (c) 3.6 mTorr, and (d) 4 mTorr.

4.3 Discussion - Presheath & boundary effects on helicon discharge equilibria

The data presented exhibit two distinct discharge equilibria. Both regimes exhibit a localized region of relatively hot electrons. In the absence of density gradients or electric fields, the region of hot electrons would have larger thermal fluxes of particles out of it than replenishing fluxes of colder electrons into it. This leads to a net change in electron density in that region in time until a steady state is achieved, or until the discharge is extinguished. In the first discharge regime represented in figures 4.3-4.5, an electric field develops adjacent to the region of hot electrons. The electric field retards the fluxes of hot electrons away from the hot region, such that the fluxes of cold electrons into the region equals the fluxes of hot electrons out. This mechanism maintains the steady state charge balance in the system.

When the grounded plate is moved away from the antenna, we observe a different discharge equilibria. In this regime, the electron temperature decays away from the localized hot region, over a longer length than the double layer-like structure previously observed. As the temperature decays, the ion density increases over the same length. The density increase maintains $\nabla_z p_e \approx 0$ everywhere in the system. Thus no electric fields are necessary to maintain constant global change balance, which is the same discharge equilibria observed by Chen et al. [55, 56, 94] in previous helicon experiments.

From these experiments it is clear that for a fixed neutral pressure, magnetic field strength, and forward rf power, the location of the downstream boundary plays a crucial role in the overall discharge equilibria. One significant factor in understanding this behavior is recognizing that the dominant electron heating mechanism may change for the dataset where the grounded plate is moved far away from the rf antenna. Two of the prominent theories for electron heating in helicon plasmas include heating due to paramet-

ric instabilities [60] and heating due to wave-trapped electrons [58, 98, 99]. The growth rate of parametric instabilities in helicon plasmas is related to the local electron and ion temperatures and wave electric fields [60]. While wave field measurements were not available in this experiment, it has been shown by Akhiezer et al. [60] and measured by Kline et al. [61, 97] that parametric instabilities are significant sinks of helicon wave energy in helicon plasmas similar to the experiment presented here ($P_{rf} \sim$ 700 W, B $\sim$ 1000 G, $p_n \sim$ 5 - 10 mTorr, $T_e \sim$ 5 - 10 eV, $n_e \sim 10^{12} - 10^{13} cm^{-3}$). Akhiezer et al. [60] show that the calculated helicon wave energy decay length for these parameters is on the order of 10 cm. Thus they claim that electron temperature peaks this distance from the rf antenna may be caused by helicon wave absorption and subsequent electron heating due to parametric instabilities. In our experiment, when the plate was held at 22 or 27 cm from the rf antenna, the hot electrons were observed 10 - 20 cm away from the rf antenna. This suggests that in these regimes, parametric instabilities may be the driver of electron heating.

In the other regime, electron temperature data given in figure 4.11 when the grounded plate was held 33 cm from the rf antenna, show that the hot electrons exist within a few centimeters of the antenna. At this position, wave-trapping of electrons may be significant. Landau damping of helicon waves on electrons has been reported by several authors [57, 98, 99]. Chen and Blackwell [58] showed that Landau damping is an insufficient mechanism to explain the high ionization efficiency of helicons, however wave-trapping may still be an effective mechanism for localized electron heating. Underneath the rf antenna, the plasma density can be low enough to allow for standing wave electric fields to exist. In this experiment, Langmuir probe measurements were not possible underneath the antenna, however data in figure 4.11c show plasma density decaying steadily nearing the antenna. Wave-trapped electrons underneath the antenna can gain significant beam energies. As they flow downstream, collisions with neutrals and beam plasma instabilities can quickly thermalize the population [58], resulting in a relatively hot electron energy

distribution very near the antenna, which is what is observed in figure 4.11.

It is important to note that the heating mechanism alone does not determine whether or not a double layer-like structure will form. Indeed Akhiezer et al. [60] showed that parametric instabilities may explain the discharge equilibria first presented by Chen et al. [55, 56, 94], which did not exhibit any double layer structures. It is the dominant electron heating mode together with the location of the downstream boundary that determines the overall discharge equilibria and the presence or absence of the double layer-like structure. In the absence of a double layer-like structure, the hot electron population cools off in space due to electron heat conduction. As is observed in figure 4.11 and calculated by Chen et al. [55], this cooling process takes at least a few tens of centimeters for the given helicon parameters. In order to maintain $\nabla_z p_e \approx 0$ everywhere, the plasma density has to increase on this same length scale. Within a few ion-neutral collision lengths from the grounded plate, the presheath exists to accelerate ions towards the boundary. In this region, the plasma density must decrease monotonically to maintain sufficient electric field for this process. If the presheath region overlaps with the region where the density must increase to maintain charge balance, both conditions cannot be met, and a new discharge equilibria must be found. In this case, a double layer-like structure can fulfill both requirements (maintain charge balance and a monotonic decrease in density near the grounded plate).

One additional interesting point is the fundamental role of the presheath in the overall discharge equilibria. Presheaths have been studied for many years in a variety of different situations and experiments [3, 4, 32, 74, 75, 100, 101, 102]. The potential drop across the presheath and its extent are typicaly determined by plasma parameters like electron temperature, neutral density, collision and ionization lengths. In that sense the presheath is a reactive phenomenon - it needs to exist (under the appropriate conditions [29]) but its magnitude and extent are determined externally by the plasma. For the data presented here, the required ion flow in the presheath dictates the location of the double layer-like

structure and thus the location of the abrupt termination of the hot electrons.

Chapter 5

$\psi = 16^o \rightarrow 60^o$ Experiment

5.1 Probe and LIF measurements of magnetic presheaths

		$\psi = 16^o$			$\psi = 30^o$			$\psi = 45^o$			$\psi = 60^o$		
$p_n[mTorr]$	λ/ρ_i	$P_{rf}[W]$	$n_i[10^{12}cm^{-3}]$	$T_e[eV]$	$P_{rf}[W]$	$n_i[10^{12}cm^{-3}]$	$T_e[eV]$	$P_{rf}[W]$	$n_i[10^{12}cm^{-3}]$	$T_e[eV]$	$P_{rf}[W]$	$n_i[10^{12}cm^{-3}]$	$T_e[eV]$
1	≈ 4	500	1.3	3.5	500	1.1	3.5	450	1	4.5	550	1.2	4
3	≈ 1	500	2.3	5.1	500	2	3.5	650	2.2	3.8	750	1.7	2.5
6.5	≈ 0.5	600	2.5	4	600	2.8	4	500	2.3	4	750	2.1	3.5

Table 5.1: Table of the upstream plasma parameters for all datasets where p_n is the neutral fill pressure, P_{rf} is the forward rf power, n_i is the ion density, T_e is the electron temperature, λ/ρ_i is the ion-neutral collision length ratio to ion gyro radius, and ψ is the angle between the magnetic field and the plate normal. "Upstream" measurements are taken on axis underneath the upstream magnetic field coil, visible in figure 3.18.

For this experiment LIF and Langmuir probe measurements were performed at 5 radial locations and many axial locations upstream of a grounded plate. The plate is held at either 16^o, 30^o, 45^o, or 60^o relative to the background axial magnetic field. Measurements were performed at 1, 3, and 6.5 mTorr fill pressure of argon. Table 5.1 shows the upstream plasma parameters measured using the Langmuir probe for all datasets. The forward rf power is varied between 450 and 750 W in order to achieve similar plasma densities ($\approx$

$1 \rightarrow 3 \times 10^{12} cm^{-3}$), temperatures (2.5 $\rightarrow$ 5 eV), and strong LIF signal for each set. The data in table 5.1 were taken on the system axis, underneath the upstream magnetic field coil, as seen in figure 3.18.

Figure 5.1 shows representative n_i and T_e axial profiles at different radii for the 3 mTorr, $\psi = 16^o$ dataset. The radial density profiles vary within approximately 25% at any given axial location. Profiles for other datasets exhibited the same axial and radial properties. The density for this dataset is peaked one cm off axis. Offsets in density and temperature peaks are sometimes observed in helicon discharges [70] but the physics of such phenomena are not the focus of this work.

Figure 5.2 shows a representative velocity field for a 3 mTorr plasma with the plate held at $\psi = 45^o$. The measurements are taken at the locations of the arrow tails. The size and direction of the arrows indicate the speed and direction of ion flow. Some arrows cross the black line because of their large speeds, however the positions of the measurements (as indicated by the location of the arrow tails) are no closer than 0.4 cm axially from the grounded plate at all radii. The blue arrow in the lower right hand corner indicates the size of the arrow that corresponds to an ion speed of c_s. The perpendicular scatter of some of the arrows near the center of figure 5.2 is due to noise in the IVDF data at that location. Uncertainty for drift velocity measurements vary from $\pm$ 50 m/s to $\pm$ 250 m/s depending on the local signal level. For reference, the parallel ion thermal velocities vary from 500 to 800 m/s. Integration times were limited due to sputtering of the plate on the Pyrex chamber walls, which increases opacity over time.

Figure 5.3 shows all the velocity fields for every dataset. Panel G of this figure shows the same data as figure 5.2. The arrows are rescaled to a larger size in order to make their positions and directions more evident in the smaller panels. The shaded areas indicate the regions where a 1D ion fluid model is used to analyze the data. The model is presented in the next section. The thin red lines in figure 5.3 indicate the locations where $v_{||} = c_s$. The

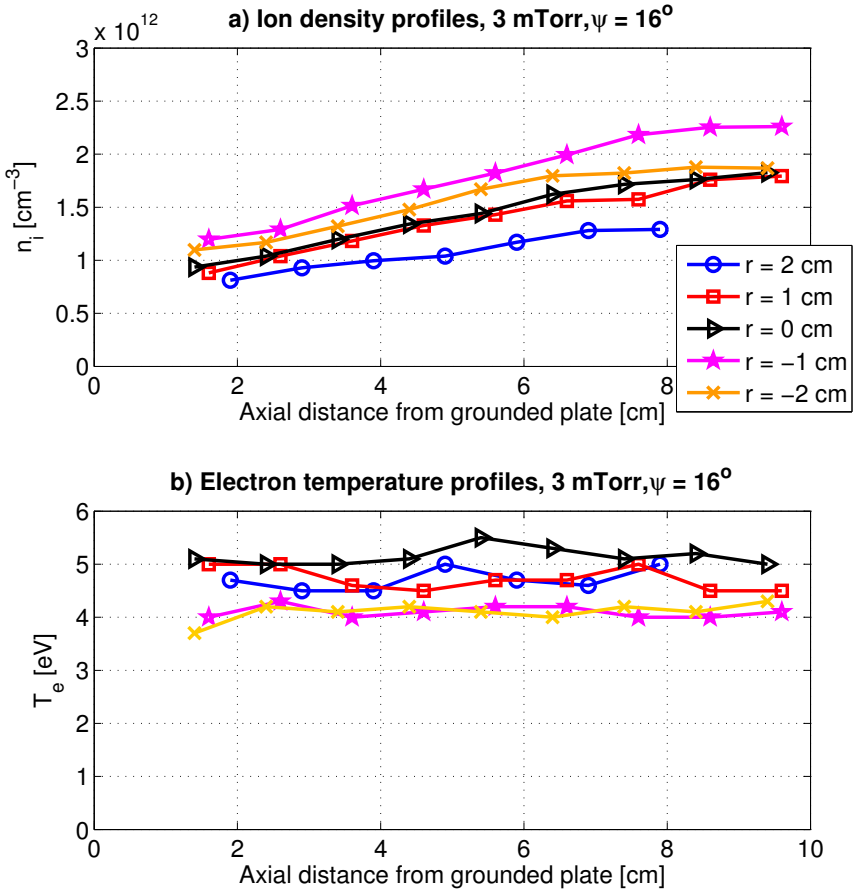

Figure 5.1: Example (a) ion density and (b) electron temperature profiles upstream from the grounded plate at different radial positions held at $\psi = 16^o$ relative to the background magnetic field, at 3 mTorr. Radial positions are in cm relative to the system axis.

thick black lines show the locations of the grounded plate. For the 3 mTorr datasets (panels E - H) these equivelocity lines do not run parallel to the grounded plate. The location where $v_{||} = c_s$ moves farther way from the plate axially at inner radii. This suggests the presence of neutral pumping, an effect often observed in helicon discharges [70, 69], which could increase the ion-neutral collision length at inner radii. As the collisional presheaths and collisional-magnetic presheath lengths scale with the ion-neutral collision length [29, 35], decreased neutral pressure on axis could increase the distance from the

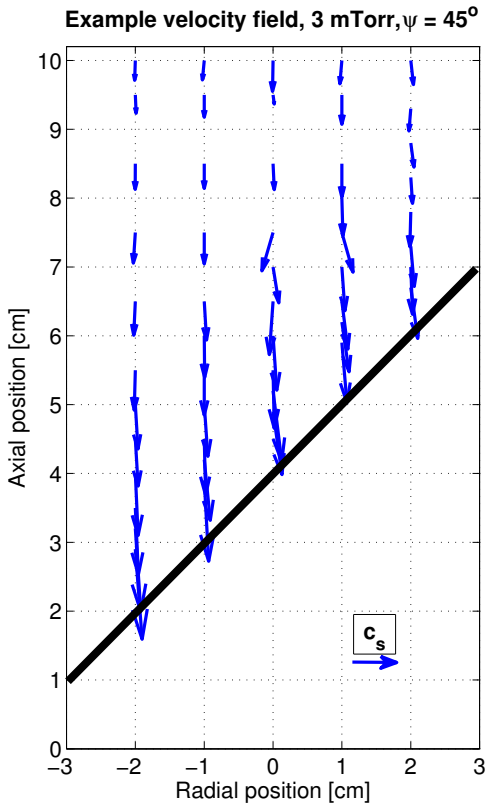

Figure 5.2: Representative velocity field from LIF measurements for a 3 mTorr plasma with $\psi = 45^o$. The solid black line indicates the location of the grounded plate.

plate where $v_{||} = c_s$. No radial variation in the sonic point is observed for the 1 mTorr dataset (panels A - D) suggesting no radial neutral pumping for these data. Red lines are not drawn for the 6.5 mTorr dataset (panels I - L) as the sonic point is not reached at the closest LIF measurement location of 0.4 cm axially from the grounded plate. Dashed lines for these data show representative equal $v_{||}$ lines, which also do not run parallel to the grounded plates, indicating the presence of neutral pumping. For several of the 1 and 6.5 mTorr datasets clear LIF signals were not obtained at all positions. Blue arrows are not shown for these locations. The data in all panels of figure 5.3 show that ion flow does not begin to bend noticeably towards the grounded plate until $\psi = 60^o$ (panels D, H, and L).

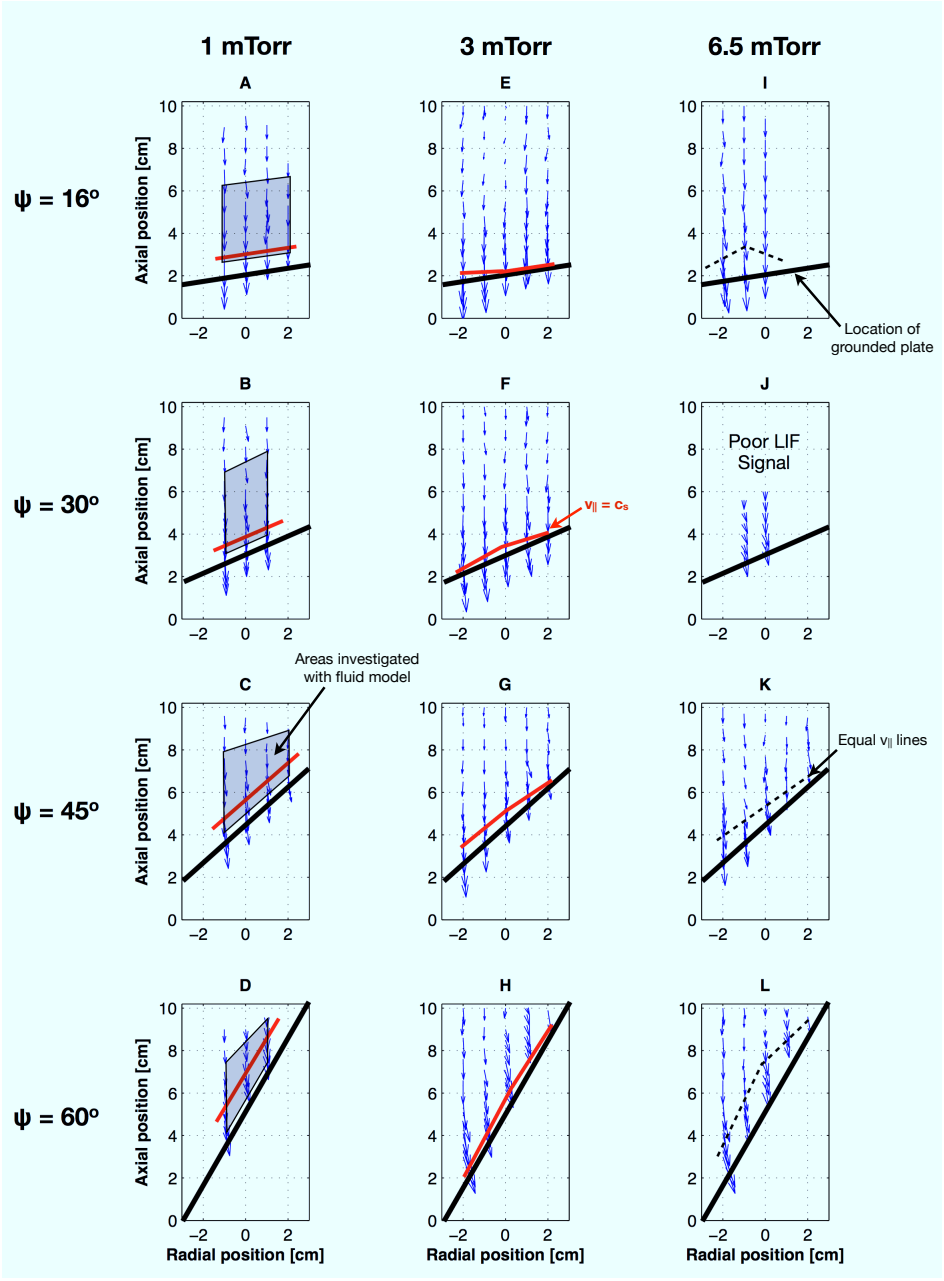

Figure 5.3: Velocity fields for all neutral pressure and plate angle datasets. The thick black lines indicate the location of the grounded plate, and the thin red lines indicate the location where $v_{||} = c_s$. Dashed lines are representative equal $v_{||}$ contours. The shaded regions highlight data used in the ion fluid model in section 5.2.

For all angles and neutral pressures $v_\perp/v_{||} \leq 25\%$.

The $v_{||} = c_s$ lines generally move closer to the plate as the neutral pressure increases (see panels A, E, and I for example). This is consistent with the results presented by Riemann [34], who shows that the parallel sonic point approaches the sheath edge as the ion-neutral collision frequency increases. For sufficiently high levels of collisionality, depending on ψ, Riemann shows that the parallel ion speed may never become supersonic prior to reaching the sheath edge for increasing collisionality due to increased cross field transport. This phenomena is observed here in panels I through L.

5.2 Ion fluid model of the magnetic presheath with collisions and ionization

As for the $\psi = 0^o$ experiment a one dimensional fluid model was developed that takes into account ion pressure, ion-neutral collisions, and ionization, all of which are important to consider at the neutral pressures and electron and ion temperatures in this experiment ($\sqrt{T_i/T_e} \approx 0.2$, and $\nu_{iz} \sim \nu_c$). The fluid model is fit to data from the 1 mTorr dataset because of the apparent absence of radial neutral density gradients (unlike the 3 and 6.5 mTorr datasets). To begin, the following equations were considered:

$$\nabla \cdot (n_i \vec{v}) = n_e n_n K \tag{5.1}$$

$$M_i n_i (\vec{v} \cdot \nabla)\vec{v} = -e n_i \nabla\phi + e n_i \vec{v} \times \vec{B} - \nabla p_i - M_i n_i \nu_c \vec{v} \tag{5.2}$$

$$n_e = n_0 exp[e(\phi - \phi_0)/T_e] \tag{5.3}$$

where $\vec{B}$ is the background magnetic field. As before, for $7 \geq T_e \geq 1$ eV, K has been fit by Gudmundsson (as referenced by Lieberman [30]) to be

$$K[m^3/s] = 2.34 \times 10^{-14} T_e[eV]^{0.59} exp(-17.44/T_e[eV]). \tag{5.4}$$

$\nu_c = n_n \sigma v$ where σ is the ion-neutral momentum transfer collision cross section. Cross section values are taken from Phelps [96]. Ion pressure is calculated from the ideal gas law such that $p_{i,||} = n_i T_{i,||}$ and $p_{i,\perp} = n_i T_{i,\perp}$. The Boltzmann relation for electron density (equation **??**) is generally valid along magnetic field lines, but across it only when the upstream reference values for density (n_0) and potential (ϕ_0) are constant across different magnetic field lines. Quasineutrality was assumed in the presheath ($n_i \approx n_e$).

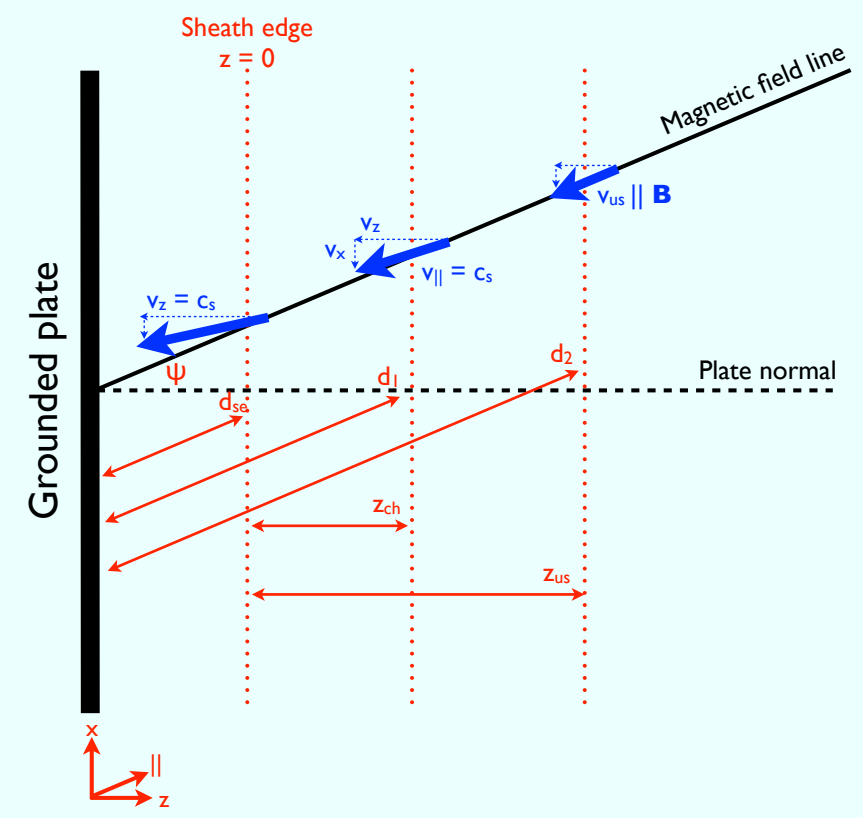

Figure 5.4: Diagram of the simulation space for the ion fluid model. $d_{se,1,2}$ are axial distances from the grounded plate. z is distance normal to the plate with $z = 0$ being the point where $v_z = c_s$. z_{ch} is Chodura's definition of the magnetic presheath thickness [24]. z_{us}, d_2 is the position of the upstream starting values used in the model where $\vec{v}$ is along $\vec{B}$. The thick blue arrows represent velocity vectors and red arrows and dotted lines represent spatial positions and axes.

The equations were evaluated in the rotated frame of reference shown in figure 5.4. In order to analyze equations 5.1 - **??** in one dimension rather than three, they were evaluated in x, y, and z under the assumption that $\frac{\partial}{\partial x}, \frac{\partial}{\partial y} \rightarrow 0$. Starting positions of $d_2 \leq 4$ cm were used, which ensured that cross field variations in T_e, n_i, and v were less than 25%. The validity of this simplification is justified afterward by the results. As ψ increases the $\frac{\partial}{\partial x}, \frac{\partial}{\partial y} \rightarrow 0$ assumption becomes less valid as motion along x translates to larger motion along d, which exhibited variations in n_i. The consequences of this are discussed in the next paragraphs. The model was evaluated from $d_2 \rightarrow d_{se}$ in figure 5.4, as for positions closer to the plate quasineutrality is no longer maintained. Given these assumptions equations 5.1 - 5.4 result in:

$$v_z \frac{\partial v_x}{\partial z} = \omega_z v_y - \nu_c v_x \tag{5.5}$$

$$v_z \frac{\partial v_y}{\partial z} = \omega_x v_z - \omega_z v_x - \nu_c v_y \tag{5.6}$$

$$v_z \frac{\partial v_z}{\partial z} = -(u_B^2 + v_{Ti}^2)\frac{1}{n_i}\frac{\partial n_i}{\partial z} - \omega_x v_y - \nu_c v_z \tag{5.7}$$

$$v_z \frac{\partial n_i}{\partial z} + n_i \frac{\partial v_z}{\partial z} = n_n n_i K \tag{5.8}$$

where $v_{x,y,z}$ is the ion drift velocity in the respective dimension, $\omega_x = eBsin(\psi)/M_i$, and $\omega_z = eBcos(\psi)/M_i$. Rearranging and combining equations 5.7 and 5.8 one obtains

$$\frac{\partial v_z}{\partial z} = \frac{(u_B^2 + v_{Ti}^2)n_n K + \omega_x v_y v_z + \nu_c v_z^2}{v_z^2 - (u_B^2 + v_{Ti}^2)}. \tag{5.9}$$

From equation 5.9, $\frac{\partial v_z}{\partial z} \rightarrow \infty$ as $v_z^2 \rightarrow c_s^2 = (u_B^2 + v_{Ti}^2)$. This occurs as quasineutrality breaks down and the Boltzmann relation no longer correctly estimates ion density. Presheath fluid models by Riemann [29, 34] approach the same singularity when $v_z^2 \rightarrow u_B^2$, as he does not include ion pressure effects. The equations here were integrated numerically from $z_{us} \rightarrow z = 0$, using data for n_i, T_e, and $\vec{v}$ as values for the upstream boundary conditions, and the results were then fit to data. The upstream neutral density and v_y were used as fitting parameters as these were not directly measured.

Because of the inclusion of the magnetic field, the velocities in all three dimensions must be resolved, unlike the fluid model for the $\psi = 0^o$ experiment. Aside from this, the other difference is the choice to solve the coupled equations in terms of drift velocities and ion density, rather than plasma potential, which are coupled through the Boltzmann relation. This choice was due to the reliance on Langmuir probe data for this experiment, rather than emissive probe data for the previous experiment.

Figure 5.5 shows fits from the numerical calculation of the fluid model to data for $v_{||}$ as a function of d/ρ_i, the axial distance from the grounded plate normalized to the ion gyro radius. The integration is terminated when $v_z = u_B = \sqrt{T_e/M_i}$ to avoid reaching the singularity at $v_z = c_s$, and as such the model does not extend to the data for $z < 0$ ($\approx d/\rho_i < 2$ in figure 5.5 panels a - c). As seen in figure 5.4, d is related to z by the transformation $d = (z/cos\psi) + d_{se}$. The resulting $v_{x,y,z}$ profiles from this calculation are shown in figure 5.6. Good fits to data are obtained using the neutral density measured by the pressure transducer ($n_n = 3 \times 10^{13} cm^{-3}$).

The $\psi = 60^o$ dataset does not extend as far as the other angles in both z and d as less area upstream from the grounded plate is available for data collection, as seen in figure 5.3D. This dataset also exhibits the worst fit to the model. As previously mentioned the assumption that $\frac{\partial}{\partial x}, \frac{\partial}{\partial y}$ is not significant is only marginally fulfilled for the $\psi = 60^o$ data.

Calculated $v_{x,y,z}$ profiles shown in figure 5.6 compare favorably to the fluid model results presented by Riemann [34] and Ahedo [35]. Consistency between the data and our fluid model calculation requires significant ion drifts in the $\vec{E} \times \vec{B}$ $(-y)$ direction. As ψ increases, a more negative v_y upstream starting value is required. This is due to greater $\vec{E} \times \vec{B}$ drift velocities due to a larger component of $\vec{B}$ normal to the presheath electric field in the z direction, as well as a greater presheath electric field to turn ions towards the plate to fulfill $v_z = c_s$ at the sheath edge.

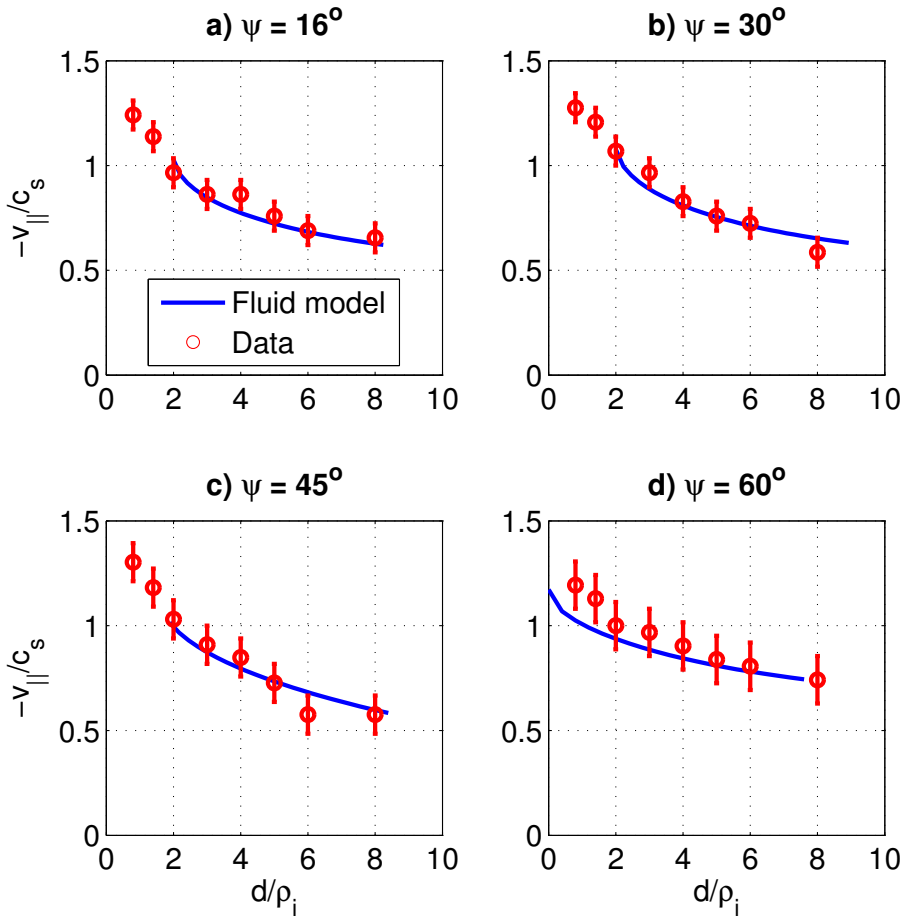

Figure 5.5: Fits of fluid models (blue lines) to 1 mTorr data (red circles) for $-v_{||}$ normalized to the sound speed ($c_s = \sqrt{(T_e + T_i)/M_i}$) for (a) $\psi = 16^o$, (b) $\psi = 30^o$, (c) $\psi = 45^o$, and (d) $\psi = 30^o$ versus axial distance from the grounded plate normalized to the ion gyro radius. The minus velocity is given due to the coordinate convention adopted (see figure 5.4).

5.3 Discussion - On ion dynamics in the magnetized plasma boundary

For the 1 mTorr dataset $\lambda/\rho_i \approx 4$, and thus the prediction by Chodura [24] for the magnetic presheath length should apply. Table 5.2 shows calculated lengths of the magnetic

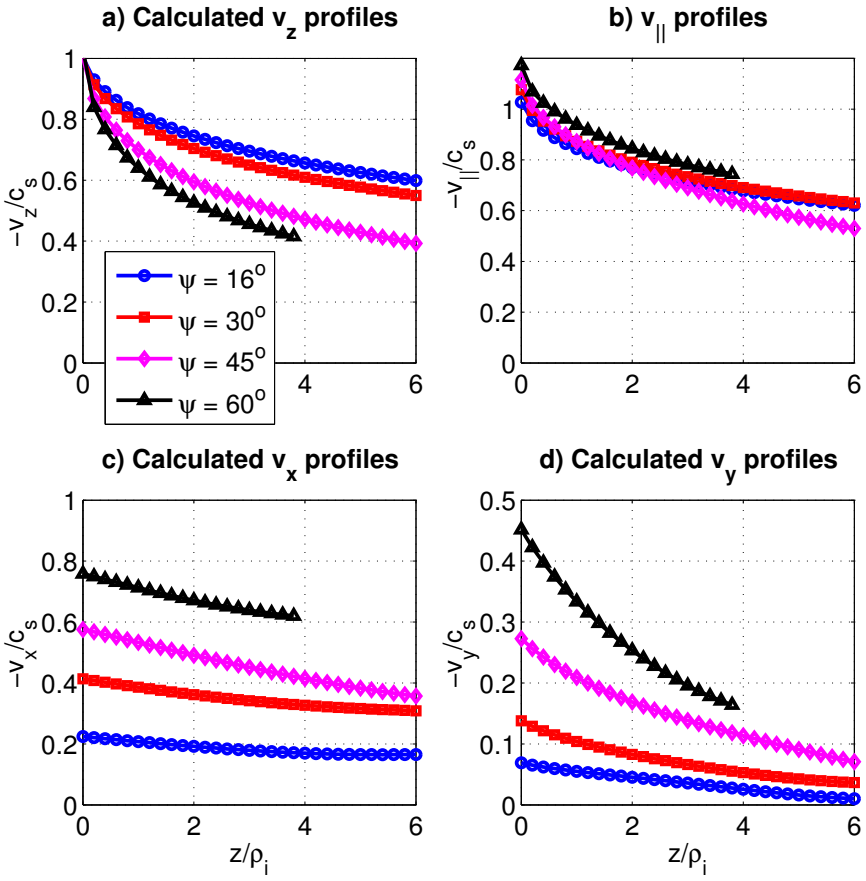

Figure 5.6: Results of the numerical fluid model calculation for 1 mTorr datasets for (a) v_z, (b) $v_{||}$, (c) v_x, and (d) v_y versus distance normal to the plate. All distances are normalized to the ion gyro radius and all velocities are normalized to the sound speed, c_s. Negative signs for velocities are due to the axes definitions shown in figure 5.4.

presheath as defined by Chodura (see figure 5.4), from the results shown in figure 5.6. This length (z_{ch}) is compared to the ion gyro radius, ion-neutral collision length, and Chodura's prediction for the magnetic presheath length, z_{ch}^{pred} ($\sqrt{6}(c_s/\omega_{ci})sin\psi$), and does not scale with any.

The results for all neutral pressures show that when collisions, ionization, temperature, and/or density gradients are present, Chodura's [24] simple prediction for the length and

ψ	λ [cm]	ρ_i [cm]	z_{ch}/ρ_i	z_{ch}^{pred}/ρ_i	z_{hm}/ρ_i
16^o	1.9	0.45 ± 0.02	0.12	1.8	0.15
30^o	1.9	0.49 ± 0.02	0.18	3.1	0.18
45^o	1.9	0.45 ± 0.03	0.25	4.4	0.21
60^o	1.9	0.4 ± 0.04	0.6	6.3	0.21

Table 5.2: Table of calculated (z_{ch}, from the fluid model) and predicted (z_{ch}^{pred}, from Chodura's [24] scaling) magnetic presheath lengths for 1 mTorr dataset. z_{hm} is the half maximum distance for the data presented in figure 5.7.

structure of the magnetized plasma boundary does not hold. The measured layer where $v_{||} = c_s \rightarrow v_z = c_s$ increases by a factor of 5 as $\psi = 16^o \rightarrow 60^o$, whereas Chodura's prediction increases by approximately a factor of 3.5. Thus in the regime where $\lambda/\rho_i \approx 4$ and $\nu_{iz} \sim \nu_c$, Chodura's prediction is not even a good "rule of thumb". The presheath structure can only be rigorously predicted using models that take into account all of the important physical processes. This begs the question: what exactly is meant by the term "magnetic presheath", and what does it have to do with the sonic point $v_{||} = c_s$? In figure 5.3 panels H and L, it is observed that ions begin to deflect from the magnetic field prior to this parallel sonic point. Conversely, in the remaining panels it is seen that the ion velocities are not deflected noticeably until $\psi = 60^o$. As Ahedo [35] has shown, when $\lambda/\rho_i \sim \mathcal{O}(1)$ the collisional and magnetic presheaths become indistinct, meaning the region where the ions achieve drift velocities perpendicular to the magnetic field lines is not correlated with the ion drift velocity sonic point parallel to the magnetic field line. This result is confirmed experimentally here. Riemann [34] argues that the parallel sonic point is the location that is "characterized by a change in dynamic process, which is responsible for the presheath mechanism", from collisional friction along the magnetic field lines to forces pushing ions

across field lines. Thus at this point the ion flow deviates "significantly" from the magnetic lines of force.

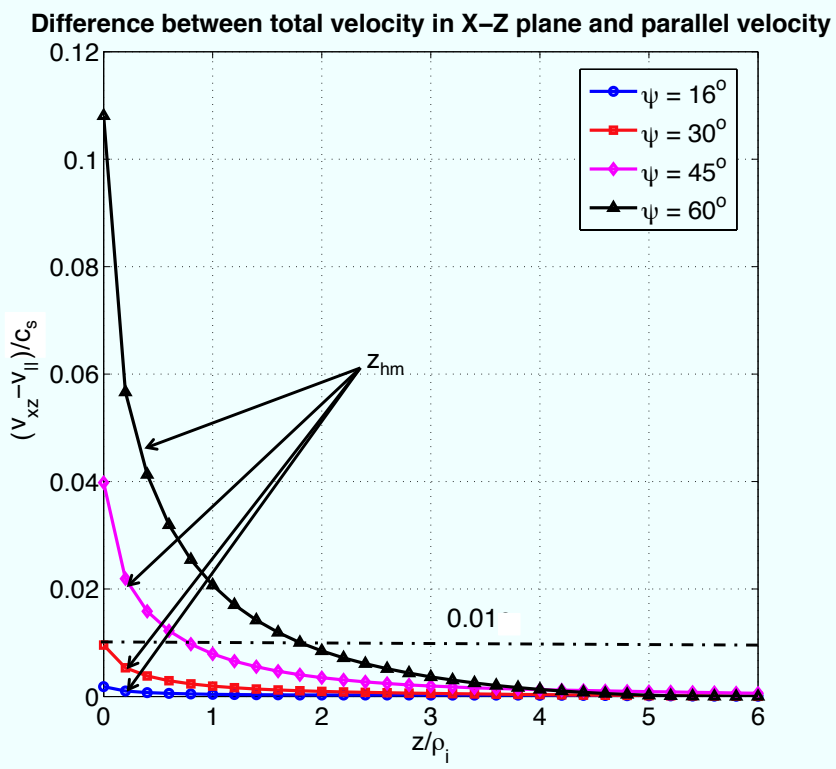

Figure 5.7: Total ion drift velocity in the $x-z$ plane ($\sqrt{v_x^2+v_z^2}$) minus $v_{||}$ versus normal distance from the grounded plate for 1 mTorr dataset-benchmarked fluid model. All velocities are normalized to the sound speed, c_s, and all distances normalized to the ion gyro radius. The dashed-dotted line indicates the ordinate position where $v_{xz}-v_{||}$ = 1% of c_s. The black arrows point to the locations of z_{hm} for each ψ.

To help clarify this ambiguity the total ion drift velocity in the $x-z$ plane (v_{xz}) minus the ion drift velocity along the magnetic field is graphed in figure 5.7. As the ions curve away from the field lines $v_{xz}-v_{||}>0$. Table 5.2 compares the parallel sonic point (z_{ch}) and the half maximum point (z_{hm}) for the curves in figure 5.7. The table shows that for $\psi = 16^o \rightarrow 45^o$ $z_{ch} \approx z_{hm}$. For $\psi = 60^o$, effects of radial gradients may reduce the validity of the model used to calculate z_{ch} and z_{hm}. In light of this, the location of the

sonic point parallel to the magnetic field can be said to indicate the position where ion flow has "significantly" deviated from the magnetic field lines, and Riemann's [34] definition of magnetic presheaths is substantiated.

Another point of view recognizes that in general, from figure 5.7 for increasing ψ the region where $\vec{v}$ is no longer parallel to $\vec{B}$ by some amount ($v_{xz} - v_{||}$ = 0.01c_s for example) moves farther away from the sheath edge. Thus another definition for the term "magnetic presheath" is the layer near the boundary where $\vec{v}$ is no longer parallel to $\vec{B}$, but v_z has not yet achieved the sound speed, and can be referred to by the fractional deviation from flow along the field lines. For example the layer where $v_{xz} - v_{||} \geq 0.01c_s$ to $v_z = c_s$ can be referred to as the "1%" magnetic presheath. From figures 5.3 and 5.7 it is clear that this point need not correlate with the parallel sonic point. In fact, the 6.5 mTorr data, and previous analysis by Riemann [34], show that given a sufficiently high collision frequency ("sufficiently" depends on the other system parameters, as shown by Riemann), $v_{||}$ may never reach the sound speed, as transport to the boundary increases perpendicular to the field lines due to collisions with neutrals.

It is important to recognize the total ion drift velocity deviation from along the magnetic field lines. As seen in figure 5.3, the ion flow deviation in the $x - z$ plane from along the magnetic field lines only becomes apparent when $\psi = 60^o$. Analysis of the fluid model reveals that deviation occurs for all angles, but it is only a few percent of the total ion drift velocity in the $x - z$ plane. An incorrect conclusion for these angles of attack and collisionality regimes is that ions impact the wall close to the angle of incidence of the magnetic field. This is false because the $\vec{E} \times \vec{B}$ velocity has not yet been considered. Figure 5.6d shows that the $\vec{E} \times \vec{B}$ drift velocity is 10% $\rightarrow$ 40% of the sound speed at the sheath edge in our experiment. Thus to account for the angular impact of ions on the magnetized boundary, it is imperative to resolve the entire 3-dimensional flow. The effect of $\vec{E} \times \vec{B}$ drifts with regard to turbulence and heat fluxes are considered for fusion exper-

iments [10, 103, 104, 105] but may not be considered for sputtering and erosion effects. It is well known that sputtering yields from materials depend strongly on the angular incidence of the incoming ions [10, 30]. For proper modeling of divertor wall erosion in fusion experiments, the details of the magnetized plasma boundary within a few ion gyro radii from the wall, and especially the $\vec{E} \times \vec{B}$ velocity in this region, must be resolved. Futhermore, data in figure 5.3 and the model results presented in figures 5.6 and 5.7, show that the ion flow deviation from along the magnetic field lines occurs, in these experiments, within a few λ of the sheath edge. As such, charge exchange collisions in these regions will generate populations of fast neutrals that impact the wall at various angles of attack, possible significantly contributing to wall erosion and sputtering rates.

In Hall thrusters, ions are often treated as unmagnetized [106]. However recent Hall thruster designs have significant components of $\vec{B}$ parallel to the wall and as such near the sheath-presheath transition, significant $\vec{E} \times \vec{B}$ flows can be present [107, 108]. These flows can alter the ion impact angle significantly, potentially exacerbating wall erosion. This may be a source of discrepancy between wall erosion models and experiments. For example, wall erosion of the SPT-100 [109, 110] Hall thruster is modeled by Gamero-Castaño and Katz [111]. The model used is called HPHall, and is a commonly used hybrid PIC-fluid code used for simulating Hall thruster wall erosion [112]. Ion flow in the azimuthal ($\vec{E} \times \vec{B}$ direction) is not considered in this model as ions are assumed to be unmagnetized [113]. However, close inspection of the results by Gamero-Castaño and Katz shows that discrepancies between wall erosion models and experiments are most severe in regions in the Hall thruster where the ions are still magnetized (prior to significant axial acceleration). In these regions the ion $\vec{E} \times \vec{B}$ flow would change the angle of incidence to the wall, changing the erosion rate. As such, full three-dimensional magnetic flow effects need to be properly realized in order to appropriately model the plasma boundary in Hall thrusters.

Chapter 6

Conclusions

While presheaths have been investigated for many years, the studies have largely been concerned with regimes where ionization and collisions were not important, and the plasma was quiescent. Many theories and experiments often make simplifying assumptions about plasma boundaries such as presheath lengths and magnitudes, and the presence of "magnetic" presheath boundary layers, using results from previous experiments in simple plasmas ($\lambda_D/\lambda \rightarrow 0$, $\rho_i/\lambda \rightarrow 0$ or $\rho_{i,e} \rightarrow \infty$). The experiments presented here show that in many regimes of interest, such as the edges of fusion experiments and Hall thrusters, these assumptions are not only incorrect, they are very misleading. The experiments here investigate presheath formation in plasmas where the ion-neutral collision length is much smaller than the scale sizes of the system, yet much larger than the Debye length, $\psi \neq 0^o$, and $\lambda \sim \rho_i$. Furthermore the ionization frequency is comparable to the ion-neutral collision frequency. Other complications include the presence of neutral pumping and localized electron heating. As such, all of these phenomena were included and were found to play major roles in the formation and analysis of the presheath structures.

In the first experiment, a grounded plate was held normal to the axial magnetic field. In this experiment two separate helicon discharge equilibria are observed. In the first regime the grounded plate is held 22 or 27 cm from the rf antenna. Hot electrons ($T_e \approx 10$ eV) are

observed 10 - 20 cm away from the antenna. The hot electrons, being approximately 10 cm from the grounded plate, do not have enough space to cool off from heat conduction, as this would require an increase in downstream density in the same location that it must decrease monotonically in the presheath. Instead a double layer-like structure forms adjacent to the hot electrons. This structure is much more compact (a few λ long) and as such can maintain steady state charge balance everywhere in the system while maintaining the monotonic decrease in density required by the presheath of the grounded plate. The location of the double layer-like structure is determined by matching the ion exit velocity from the double layer and the necessary ion velocity in the presheath.

The second discharge equilibria in this experiment occurs when the grounded plate is moved to 33 cm from the rf antenna, with all other parameters (neutral pressure, magnetic field, and forward rf power) held constant. In this case (figure 4.11) hot electrons are observed within 5 cm of the edge of the antenna. The electrons cool over approximately 15 cm, and the plasma density increases over this same scale length. The temperature decay and density increase are sufficient to maintain $\nabla_z p_e \approx 0$. No significant electric fields are measured. No double layer-like structure is necessary as the hot electrons, located near the antenna, and the grounded plate, pulled away from the antenna, are far enough away to allow for the electrons to cool from heat conduction, the density to increase to maintain pressure balance, and to still allow enough room for a presheath to form in front of the grounded plate.

For the second experiment the grounded plate was held at various angles of attack relative to the axial magnetic field. The results of the 1 mTorr datasets were used to benchmark a fluid model for the ion flows that takes into account ion-neutral collisions, ionization, and thermal effects. Using the 1 mTorr data and the fluid model, the length of the magnetic presheath is shown to not follow Chodura's [24] model that neglects ionization and collisions. Instead the measurements confirm predictions made by Riemann [34] and Ahedo

[35] regarding ion flow to the magnetized plasma boundary. In the presence of collisions and ionization the collisional and magnetic presheaths become indistinct, and an accurate model of the boundary must take into account all the relevant phenomena. It is argued that the definition of the magnetic presheath is not fully resolved. The data at 1 mTorr support Riemann's [34] argument that the point where $v_{||} = c_s$ identifies the location where the dominant force on the ion flow changes. In addition we provide another definition for the magnetic presheath, which calls it the region where ion flow breaks away from the magnetic field line by a given amount (1%, for example) that need not correlate with the parallel sonic point when collisions and ionization are important. Finally the results of all the datasets and the fluid model show that the ion flow in the plane normal to the boundary largely follows the magnetic field lines for the experimental parameters investigated. However, ion flows parallel to the plate and normal to this plane can be a few tens of percent of the sound speed at the sheath edge, even for low angles of incidence of the magnetic fields. These flows must be accounted for to fully understand transport to, and sputtering from the boundaries of fusion experiments and Hall thrusters.

When treating the plasma boundary for one of the many applications of plasma physics, simple models are often assumed for ion flows and scale lengths of potential structures to obtain estimates for performance for various experimental and industrial applications. As seen in this work however, frequently these estimates are wrong. The presheath for the $\psi = 0^o$ experiment was seen to play a fundamental role in establishing a novel discharge mode of a helicon plasma, rather than being a purely reactive phenomena. Furthermore, ionizations and collisions in magnetic presheaths were shown to break down assumptions that underly preexisting models. The system is so sensitive to these assumptions that the presence of significant collisions and ionization cause the original simplified models not only to be inaccurate, but also misleading. In all, the plasma boundary is a complicated non-linear system that is highly affected by the values of all the plasma parameters, and

more care needs to be taken when modeling and understanding this region.

Bibliography

[1] F. F. Chen, *Introduction to Plasma Physics and Controlled Fusion*, Plenum Press, New York (1984).

[2] S. Robertson, Plasma Physics and Controlled Fusion **55**, 093001 (2013).

[3] K.-U. Riemann, Physics of Plasmas **4**, 4158 (1997).

[4] L. Oksuz and N. Hershkowitz, Physical Review Letters **89**, 145001 (2002).

[5] N. Hershkowitz, Physics of Plasmas **12**, 055502 (2005).

[6] S. D. Baalrud and C. C. Hegna, Plasma Sources Science and Technology **20**, 025013 (2011).

[7] J. E. Allen, Plasma Sources Science and Technology **18**, 014004 (2009).

[8] R. N. Franklin, Journal of Physics D: Applied Physics **36**, R309 (2003).

[9] R. P. Brinkmann, Journal of Physics D: Applied Physics **44**, 042002 (2011).

[10] P. C. Stangeby, The Plasma Boundary of Magnetic Fusion Devices, Taylor & Francis (2000).

[11] E. Sommier, M. K. Allis, N. Gascon, and M. A. Capelli, in *Proceedings of the 42nd Joint Propulsion Conference, Sacramento, California* (American Institute of Aeronautics and Astronautics, Reston, VA, 2006), AIAA 2006-4656.

[12] I. H. Hutchinson, *Principles of Plasma Diagnostics* (Cambridge University Press, New York, 2002).

[13] A. Wingen, O. Schmitz, T. E. Evans, and K. H. Spatschek, Physics of Plasmas **21**, 012509 (2014).

[14] H. Frerichs, O. Schmitz, D. Reiter, T. E. Evans, and Y. Feng, Physics of Plasmas **21**, 020702 (2014).

[15] J. Loizu, P. Ricci, F. D. Halpern, and S. Jolliet, Physics of Plasmas **19**, 122307 (2012).

[16] H. R. Strauss, Physics of Plasmas **21**, 032506 (2014).

[17] E. Sommier, M. K. Scharfe, N. Gascon, M. A. Capelli, and E. Fernandez, IEEE Transactions on Plasma Science **35**, 1379 (2007).

[18] S. Y. Cheng and M. Martinez-Sanchez, Journal of Propulsion and Power **24**, 987 (2008).

[19] M. Keidar and I. I. Beilis, Applied Physics Letters **94**, 191501 (2009).

[20] J. G. Laframboise, Journal of Geophysical Research **102**, 2417 (1997).

[21] I. H. Hutchinson, Physical Review Letters **101**, 035004 (2008).

[22] R. W. Boswell, Plasma Physics and Controlled Fusion **26**, 10 (1984).

[23] G. D. Porter, S. L. Allen, M. Brown, M. E. Fenstermacher, D. N. Hill, R. A. Jong, A. W. Leonard, D. Nilson, M. E. Rensink, T. D. Rognlien, G. R. Smith, and the DIII-D Team, Physics of Plasmas **3**, 1967 (1996).

[24] R. Chodura, Physics of Fluids **25**, 1628 (1982).

[25] I. Langmuir, General Electric Review **26**, 731 (1923).

[26] D. J. Griffiths, *Introduction to Electrodynamics*, Prentice Hall, New Jersey (1999).

[27] I. Langmuir, Physics Review **33**, 954 (1929).

[28] D. Bohm, *The Characteristics of Electrical Discharges in Magnetic Field*, ed. A Guthrie & R. K. Wakerling, McGraw Hill, New York (1949).

[29] K.-U. Riemann, Journal of Physics D: Applied Physics **24**, 493 (1991).

[30] M. A. Lieberman and A. J. Lichtenberg, *Principles of Plasma Discharges and Materials Processing*, Wiley, New Jersey (2005).

[31] D. J. Koch and W. N. G. Hitchon, Physics of Fluids B: Plasma Physics **1**, 2239 (1989).

[32] L. Oksuz, M. Atta Khedr, and N. Hershkowitz, Physics of Plasmas **8**, 1729 (2001).

[33] N. Hershkowitz, E. Ko, X. Wang, and A. M. A. Hala, IEEE Transactions of Plasma Science **33**, 631 (2005).

[34] K.-U. Riemann, Physics of Plasmas **1**, 552 (1994).

[35] E. Ahedo, Physics of Plasmas **4**, 4419 (1997).

[36] P. C. Stangeby, Physics of Plasmas **2**, 702 (1995).

[37] G.-H. Kim, N. Hershkowitz, D. A. Diebold, and M.-H. Cho, Physics of Plasmas **2**, 3222 (1995).

[38] B. Singha, A. Sarma, and J. Chutia, Physics of Plasmas **9**, 683 (2002).

[39] H. Schmitz, K.-U. Riemann, and Th. Daube, Physics of Plasmas **3**, 2486 (1996).

[40] I. I. Beilis, M. Keidar, and S. Goldsmith, Physics of Plasmas **4**, 3461 (1997).

[41] D. D. Tskhakaya, P. K. Shukla, B. Eliasson, and S Kuhn, Physics of Plasmas **12**, 103503 (2005).

[42] N. Hershkowitz, Space Science Reviews **41**, 351 (1985).

[43] C. Charles, Plasma Sources Science and Technology **16**, R1 (2007).

[44] P. Coakley and N. Hershkowitz, Physics of Fluids **22**, 6 (1979).

[45] C. Charles and R. Boswell, Applied Physics Letters **82**, 9 (2003).

[46] I. A. Biloiu and E. E. Scime, Applied Physics Letters **95**, 051504 (2009).

[47] M. Merino and E. Ahedo, Plasma Sources Science and Technology **23**, 032001 (2014).

[48] G. Hairapetian and R. L. Stenzel, Physical Review Letters **65**, 2 (1990).

[49] K. Sato and F. Miyawaki, Physics of Fluids B: Plasma Physics **5**, 5 (1992).

[50] C.-G. Fälthammar, Reviews of Geophysics and Space Physics **15**, 4 (1977).

[51] C. Chan, N. Hershkowitz, and K. E. Lonngren, Physics of Fluids **26**, 6 (1983).

[52] B. W. Longmier, Ph.D. thesis, University of Wisconsin - Madison (2007).

[53] F. F. Chen, Plasma Physics and Controlled Fusion **33**, 339-364 (1991).

[54] I. D. Sudit and F. F. Chen, Plasma Sources Science and Technology **5**, 43 (1996).

[55] F. F. Chen, I. D. Sudit, and M. Light, Plasma Sources Science and Technology **5**, 173 (1996).

[56] F. F. Chen, Physics of Plasmas **3**, 5 (1996).

[57] R. T. S. Chen and N. Hershkowitz, Physical Review Letters **80**, 4677 (1998).

[58] F. F. Chen and D. D. Blackwell, Physical Review Letters **82**, 2677 (1999).

[59] D. A. Arnush and F. F. Chen, Physics of Plasmas **5**, 1239 (1998).

[60] A. I. Akhiezer, V. S. Mikhailenko, and K. N. Stepanov, Physics Letters A **245**, 117 (1998).

[61] J. L. Kline et al., Physical Review Letters **88**, 195002 (2002).

[62] E. E. Scime, R. Hardin, C. Biloiu, A. M. Keesee, and X. Sun, Physics of Plasmas **14**, 043505 (2007).

[63] E. E. Scime et al., Plasma Sources Science and Technology **7**, 186 (1998).

[64] V. S. Mikhailenko, K. N. Stepanov, and E. E. Scime, Physics of Plamsas **10**, 2247 (2003).

[65] E. E. Scime, J. Carr Jr., M. Galante, R. M. Magee, and R. Hardin, Physics of Plasmas **20**, 032103 (2013).

[66] S. Chakraborty Thakur et al., Physics of Plasmas, **19** 082101 (2012).

[67] A. M. Keesee and E. E. Scime, Plasma Sources Science and Technology **16**, 742 (2007).

[68] S. Houshmandyar and E. E. Scime, Plasma Sources Science and Technology **21**, 035008 (2012).

[69] C. M. Denning, M. Wiebold, and J. E. Scharer, Physics of Plasmas **15**, 072115 (2008).

[70] J. Gilland, R. Breun, and N. Hershkowitz, Plasma Sources Science and Technology **7**, 416 (1998).

[71] K.-U. Riemann, Physics of Fluids B: Plasma Physics **4**, 2693 (1992).

[72] J. Zheng, R. P. Brinkmann, and J. P. McVittie, Journal of Vacuum Science and Technology A **13**, 859 (1995).

[73] J. A. Meyer, G.-H. Kim, M. J. Goeckner, and N. Hershkowitz, Plasma Sources Science and Technology **1**, 147 (1992).

[74] B. Jacobs, W. Gekelman, P. Pribyl, M. Barnes, and M. Kilgore, Applied Physics Letters **91**, 161505 (2007).

[75] X. Sun, S. A. Cohen, E. E. Scime, and M. Miah, Physics of Plasmas **12**, 103509 (2005).

[76] F. F. Chen, *Plasma Diagnostic Techniques*, ed. R. H. Huddlestone and S. L. Leonard, Ch. 4, Academic Press Inc., New York (1965).

[77] N. Hershkowitz, *Plasma Diagnostics*, ed. O. Auciello and D. L. Flamm, Ch. 3, Academic Press Inc., New York (1989).

[78] J. E. Allen, Physica Scripta **45**, 497 (1992).

[79] A. R. Hoskinson and N. Hershkowitz, Plasma Sources Science and Technology **15**, 85 (2006).

[80] J. E. Allen, R. L. F. Boyd, and P. Reynolds, Proceedings of the Physical Society Section B **70**, 297 (1957).

[81] I. D. Sudit and F. F. Chen, Plasma Sources Science and Technology **3**, 162 (1994).

[82] L. Oksuz, F. Soberón, and A. R. Ellingboe, Journal of Applied Physics **99**, 013304 (2006).

[83] C.-S. Yip, J. P. Sheehan, N. Hershkowitz, and G. Severn, Plasma Sources Science and Technology **22**, 065002 (2013).

[84] J. P. Sheehan, Y. Raitses, N. Hershkowitz, I. Kaganovich, and N. J. Fisch, Physics of Plasmas **18**, 073501 (2011).

[85] J. Y. Kim, H.-C. Lee, D.-H. Kim, Y.-S. Kim, Y.-C. Kim, and C.-W. Chung, Physics of Plasmas **21**, 023511 (2014).

[86] A. E. Wendt, Review of Scientific Instruments **72**, 2926 (2001).

[87] J. P. Sheehan and N. Hershkowitz, Plasma Sources Science and Technology **20**, 063001 (2011).

[88] R. F. Kemp and J. M. Sellen, Review of Scientific Instruments **37**, 455 (1966).

[89] E. Y. Wang, N. Hershkowitz, T. Intrator, and C. Forest, Review of Scientific Instruments **10**, 2425 (1986).

[90] N. Uzelac and F. Leis, Spectrochimica Acta **47**, 877 (1992).

[91] G. D. Severn, D. A. Edrich, and R. McWilliams, Review of Scientific Instruments **1**, 10 (1997).

[92] A. M. Keesee, E. E. Scime, and R. F. Boivin, Review of Scientific Instruments **10**, 4091 (2004).

[93] N. Hershkowitz, B. Nelson, J. Pew, and D. Gates, Review of Scientific Instruments **54**, 29 (1983).

[94] I. D. Sudit and F. F. Chen, Plasma Sources Science and Technology **5**, 43 (1996).

[95] P. Helander, S. I. Krasheninnikov, and P. J. Catto, Physics of Plasmas **1**, 3174 (1994).

[96] A. V. Phelps, Journal of Physical and Chemical Reference Data **20**, 557 (1991).

[97] J. L. Kline and E. E. Scime, Physics of Plasmas **10**, 135 (2003).

[98] A. R. Ellingboe, R. W. Boswell, J. P. Booth, and N. Sadeghi, Physics of Plasmas **2**, 1807 (1995).

[99] A. W. Molvik, A. R. Ellingboe, and T. D. Rognlien, Physical Review Letters **79**, 233 (1997).

[100] G. A. Emmert, R. M. Wieland, A. T. Mense, and J. N. Davidson, Physics of Fluids **23**, 803 (1980).

[101] M. A. Hussein and G. A. Emmert, Physics of Fluids B: Plasma Physics **2**, 218 (1990).

[102] J. A. Meyer, G.-H. Kim, M. J. Goeckner, and N. Hershkowitz, Plasma Sources Science and Technology **1**, 147 (1992).

[103] P. C. Stangeby and A. V. Chankin, Nuclear Fusion **36**, 839 (1996).

[104] A. V. Chankin, Journal of Nuclear Materials **241**, 199 (1997).

[105] J. Loizu, P. Ricci, F. D. Halpern, S. Jolliet, and A. Mosetto, Physics of Plasmas **21**, 062309 (2014).

[106] M. Keidar, I. D. Boyd, and I. I. Beilis, Physics of Plasmas **8**, 5315 (2001).

[107] Y. Raitses and N. J. Fisch, Physics of Plasmas **8**, 2579 (2001).

[108] M. Keidar and I. D. Boyd, Applied Physics Letters **87**, 121501 (2005).

[109] L. Garrigues, G. J. M. Hagelaar, J. Bareilles, C. Boniface, and J. P. Boeuf, Physics of Plasmas **10**, 4886 (2003).

[110] N. Gascon, M. Dudeck, and S. Barral, Physics of Plasmas **10**, 4123 (2003).

[111] M. Gamero-Castaño and I. Katz, in *29th International Electric Propulsion Conference, Princeton, NJ* (Electric Rocket Propulsion Society, Cleveland, Ohio, 2005), IEPC 05-303.

[112] F. I. Parra, E. Ahedo, J. M. Fife, and M. Martínez-Sánchez, Journal of Applied Physics **100**, 023304 (2006).

[113] M. Martínez-Sánchez, Personal communication (2014).